

COMBINED DILATOMETRY AND MASS SPECTROMETRY OF SINTERING AND
EVOLVED GASES OF BARIUM TITANATE AND ZIRCONIUM DIBORIDE WITH
SINTERING ADDITIVES

A Thesis presented to the Faculty of the Graduate School
University of Missouri

In Partial Fulfillment
Of the Requirements for the Degree
Master of Science

by

MURRAY MOSS

Dr. Stephen J. Lombardo, Thesis Supervisor

DECEMBER 2012

The undersigned, Appointed by the Dean of the Graduate School, have examined the
thesis entitled

**COMBINED DILATOMETRY AND MASS SPECTROMETRY OF SINTERING
AND EVOLVED GASES OF BARIUM TITANATE AND ZIRCONIUM
DIBORIDE WITH SINTERING ADDITIVES**

Presented by

Murray Moss

A candidate for the degree of

Master of Science

And hereby certify that in their opinion it is worth of acceptance.

Dr. Stephen J. Lombardo _____

Dr. David Retzloff _____

Dr. Alan Whittington _____

ACKNOWLEDGEMENTS

I would like to first thank Dr. Stephen J. Lombardo for giving me the opportunity to work in his lab and for all the time he has spent with me on this project. Dr. Lombardo has been all that a teacher and mentor should be: an invaluable source of knowledge, one which motivates and challenges you to grow, all the while showing enormous patience. I really appreciate all you have done for me and wish you success in the future.

Secondly, I would like to thank the GAANN (Graduate Assistantship in Areas of National Need) Fellowship for financial support for both myself and the lab, and for the opportunity to meet other professionals by attending conferences.

I would also like to thank my Thesis Committee members Dr. Retzloff and Dr. Whittington for their time and input in the process of finishing this thesis. I also would not have been able to finish this without the help of the staff from the Chemical Engineering Department, specifically Rita Preckshot and Jennifer Keyzer-Andre, and the Engineering Technical Services electrician Rich Oberto.

A big thank you is also necessary to fellow graduate assistants Matt Schurwanz, Brandon Abeln, Ki-Yong Lee, Mojtaba Asadirad, and Jun Oh, and all of the previous graduate assistants who have worked for Dr. Lombardo and set the foundation for this work, especially Kai Feng, Chang Soo Kim, and Jeong Woo Yun.

Finally I would like to thank my beautiful wife Danielle for all of her love and dedication during my work. Our families have also been very supportive, for which I am very grateful.

TABLE OF CONTENTS

ACKNOWLEDGEMENTS	ii
LIST OF FIGURES	vi
LIST OF TABLES	x
ABSTRACT.....	xii
CHAPTERS	
1. INTRODUCTION	1
1.1 General Background	2
1.2 Analysis Techniques	6
1.3 Motivation, Objective, and Thesis Organization	8
1.4 References.....	11
2. EXPERIMENTAL AND SYSTEM DETAILS	15
2.1 Introduction.....	16
2.1.1 System Overview	16
2.2 System Details	17
2.2.1 Coolant Flow Paths	17
2.2.2 Gas Flow Paths	18
2.2.3 Dilatometer	20
2.2.4 Furnace.....	21
2.2.5 Mass Spectrometer.....	26
2.3 Improvements	27
2.4 Procedure	28
2.5 References.....	33

3.	EVOLVED GAS ANALYSIS OF BARIUM TITANATE, BARIUM CARBONATE, AND BARIUM SULFATE, WITH BACKGROUND CHEMISTRY OF THE CDMS	34
3.1	Introduction.....	35
3.2	Experimental	37
3.3	Results.....	40
3.3.1	Inert Conditioning Heating Cycle	40
3.3.2	Background Heating Cycle	44
3.3.3	Barium Sulfate	46
3.3.4	Barium Carbonate	50
3.3.5	Barium Titanate Heated at 14°C/min.....	53
3.3.6	Barium Titanate Heated at 8°C/min.....	61
3.3.7	Barium Titanate Heated at 20°C/min.....	64
3.3.8	Loose Barium Titanate Heated at 14°C/min.....	66
3.4	Discussion	69
3.5	Conclusions.....	70
3.6	References.....	72
4.	HIGH TEMPERATURE CHEMISTRY OF ZIRCONIUM DIBORIDE AND SINTERING ADDITIVES	74
4.1	Introduction.....	75
4.2	Experimental	78
4.3	Results.....	80
4.3.1	Boron Oxide.....	80
4.3.2	Boron Nitride Spray	82
4.3.3	Zirconium Diboride	86

4.3.4	Boron Carbide.....	91
4.3.5	Silicon Carbide.....	93
4.3.6	Zirconium Oxide.....	95
4.4	Discussion.....	98
4.5	Conclusions.....	99
4.6	References.....	100
5.	HIGH TEMPERATURE CHEMISTRY DURING THE HEATING OF MIXTURES OF ULTRA-HIGH TEMPERATURE MATERIALS	103
5.1	Introduction.....	104
5.2	Experimental.....	107
5.3	Results.....	110
5.3.1	Phenolic Resin	110
5.3.2	ZrO ₂ -B ₄ C.....	114
5.3.3	ZrB ₂ -B ₄ C-PR.....	118
5.3.4	ZrB ₂ -SiC-B ₄ C-PR-B-D-S	121
5.3.5	ZrB ₂ -5-ZrSi ₂	125
5.3.6	ZrB ₂ -10-ZrSi ₂	128
5.3.7	ZrB ₂ -20-ZrSi ₂	129
5.4	Discussion.....	132
5.5	Conclusions.....	133
5.6	References.....	134
6.	CONCLUSIONS AND FUTURE WORK	137
6.1	Conclusions.....	138
6.2	Future Work.....	140

LIST OF FIGURES

Figure	Page
1.1 Material transport mechanisms contributing to the sintering of a consolidated mass of polycrystalline particles: (1) surface diffusion, (2) vapor transport, (3) volume diffusion, and (4) grain boundary diffusion [1]	3
1.2 Physical states during the initial stage of sintering. (a) Starting particles, (b) rearrangement, and (c) neck formation [1]	4
1.3 Physical states during the intermediate stage of sintering. (a) Neck growth and volume shrinkage, (b) lengthening of grain boundaries, and (c) continued neck growth and grain boundary lengthening, volume shrinkage, and grain growth [1].....	5
1.4 Physical states during the final stage of sintering. (a) Grain growth with discontinuous pore phase, (b) grain growth with porosity reduction, and (c) grain growth with porosity elimination [1].....	5
2.1 Diagram of the liquid flow paths for the CDMS [1].....	17
2.2 Diagram of the gas flow paths for the CDMS [1].....	18
2.3 Diagram of the furnace to mass spectrometer interface [1]	19
2.4 Image of the positioning of the sample and spacers in the dilatometer [1]	20
2.5 Cross section diagram of the furnace [1]	22
2.6 Alumina combustion tube dimensions, modified from McDanel Ceramics combustion tube 30505	22
2.7 Actual temperature versus calculated temperature with best fit line and equation, taken from values displayed by furnace control window during heating cycles.....	24
2.8 Diagram of the primary thermocouple encasing.....	25
2.9 Image of the mass spectrometer top plate [1]	26

3.1	Temperature (Temp) and species intensity of the $m/z = 4, 12, 16, 18, 28, 32, 44, 48,$ and 64 signals versus time for the inert conditioning cycle heated at $10^{\circ}\text{C}/\text{min}$ in flowing helium	41
3.2	Temperature (Temp) and species intensity of the $m/z = 4, 16, 18, 28, 32, 44, 48,$ and 64 signals versus time for the background cycle heated at $15^{\circ}\text{C}/\text{min}$ in flowing helium	45
3.3	Temperature (Temp) and species intensity of the $m/z = 12, 16, 28, 44, 45,$ and 46 signals versus time for 0.2 g of BaSO_4 heated at $14^{\circ}\text{C}/\text{min}$ in flowing helium	47
3.4	Temperature (Temp) and species intensity of the $m/z = 16, 32, 34, 48, 49, 50, 64, 65,$ and 66 signals versus time for 0.2 g of BaSO_4 heated at $14^{\circ}\text{C}/\text{min}$ in flowing helium	48
3.5	Temperature (Temp) and species intensity of the $m/z = 12, 16, 28, 44, 45,$ and 46 signals versus time for 0.4 g of BaCO_3 heated at $14^{\circ}\text{C}/\text{min}$ in flowing helium	51
3.6	Temperature (Temp) and species intensity of the $m/z = 34, 48, 49, 50, 64, 65,$ and 66 signals versus time for 0.4 g of BaCO_3 heated at $14^{\circ}\text{C}/\text{min}$ in flowing helium	53
3.7	Temperature (Temp), length change (Dil), and species intensity of the $m/z = 28, 44, 48,$ and 64 signals versus time for 1.0 g of $\text{BaTiO}_3\text{-14}$ heated at $14^{\circ}\text{C}/\text{min}$ in flowing helium	54
3.8	Temperature (Temp), length change (Dil), and species intensity of the $m/z = 12, 16, 28, 44, 45,$ and 46 signals versus time for 1.0 g of $\text{BaTiO}_3\text{-14}$ heated at $14^{\circ}\text{C}/\text{min}$ in flowing helium	56
3.9	Temperature (Temp), length change (Dil), and species intensity of the $m/z = 16, 32, 34, 48, 49, 50, 64, 65,$ and 66 signals versus time for 1.0 g of $\text{BaTiO}_3\text{-14}$ heated at $14^{\circ}\text{C}/\text{min}$ in flowing helium	57
3.10	Temperature (Temp), length change (Dil), and species intensity of the $m/z = 28, 44, 48,$ and 64 signals versus time for 1.0 g of $\text{BaTiO}_3\text{-8}$ heated at $8^{\circ}\text{C}/\text{min}$ in flowing helium	62
3.11	Species intensity of the $m/z = 44$ and 64 signals for $\text{BaTiO}_3\text{-8}, \text{BaTiO}_3\text{-14}, \text{BaTiO}_3\text{-20},$ and $\text{BaTiO}_3\text{-14L}$ samples and length change (Dil) for $\text{BaTiO}_3\text{-8}, \text{BaTiO}_3\text{-14},$ and $\text{BaTiO}_3\text{-20}$ samples versus temperature in flowing helium	63

3.12	Temperature (Temp), length change (Dil), and species intensity of the m/z=28, 44, 48, and 64 signals versus time for 1.0 g of BaTiO ₃ -20 heated at 20°C/min in flowing helium	65
3.13	Temperature (Temp) and species intensity of the m/z=28, 44, 48, and 64 signals versus time for 0.2 g of BaTiO ₃ -14L heated at 14°C/min in flowing helium	67
4.1	Temperature (Temp) and species intensity of the m/z=18, 27, 28, 32, 44, 53, and 69 signals versus time for 0.02 g of boron oxide heated to 10°C/min in flowing helium	81
4.2	Temperature (Temp) and species intensity of the m/z=16, 28, 29, 31, 43, 44 and 45 signals versus time for 0.0001 g of boron nitride spray heated at 20°C/min in flowing helium	83
4.3	Temperature (Temp) and species intensity of the m/z=29, 31, 43, 91, 106, and 108 signals versus time for 0.0001 g of boron nitride spray heated at 20°C/min in flowing helium	85
4.4	Ethyl cellulose structure [29]	86
4.5	Temperature (Temp) and species intensity of the m/z=12, 16, 28, 44, and 45 signals versus time for 0.5 g of zirconium diboride heated at 10°C/min in flowing helium	87
4.6	Temperature (Temp) and species intensity of the m/z=29, 31, 43, 91, 106, and 108 signals versus time for 0.5 g of zirconium diboride heated at 10°C/min in flowing helium	88
4.7	Temperature (Temp) and species intensity of the m/z=12, 16, 28, 44, and 45 signals versus time for 0.5 g of boron carbide heated at 10°C/min in flowing helium	91
4.8	Temperature (Temp) and species intensity of the m/z=12, 16, 28, 44, and 45 signals versus time for 0.5 g of silicon carbide heated at 10°C/min in flowing helium	94
4.9	Temperature (Temp) and species intensity of the m/z=16, 28, 32, 44, 48, and 64 signals versus time for 0.015 g zirconium oxide heated at 10°C/min in flowing helium	96
5.1	Phenol formaldehyde (phenolic resin) repeat structure of MW=133	111

5.2	Temperature (Temp) and species intensity of the $m/z=29, 43, 45, 91, 94, 106,$ and 108 signals versus time for 0.004 g of phenolic resin heated at $10^{\circ}\text{C}/\text{min}$ in flowing helium	111
5.3	Temperature (Temp) and species intensity of the $m/z=12, 16, 28, 44,$ and 45 signals versus time for 0.004 g of phenolic resin heated at $10^{\circ}\text{C}/\text{min}$ in flowing helium	113
5.4	Temperature (Temp), length change (Dil), and species intensity of the $m/z=12, 16, 28, 44,$ and 45 signals versus time for 0.8 g of $\text{ZrO}_2\text{-B}_4\text{C}$ heated at $10^{\circ}\text{C}/\text{min}$ in flowing helium	115
5.5	Temperature (Temp), length change (Dil), and species intensity of the $m/z=12, 16, 28, 44,$ and 45 signals versus time for 0.5 g of $\text{ZrB}_2\text{-B}_4\text{C-PR}$ heated at $10^{\circ}\text{C}/\text{min}$ in flowing helium	118
5.6	Temperature (Temp) and species intensity of the $m/z=29, 31, 43, 45, 91, 94, 106,$ and 108 signals versus time for 0.5 g of $\text{ZrB}_2\text{-B}_4\text{C-PR}$ heated at $10^{\circ}\text{C}/\text{min}$ in flowing helium	119
5.7	Temperature (Temp), length change (Dil), and species intensity of the $m/z=12, 16, 28, 44,$ and 45 signals versus time for 0.5 g of $\text{ZrB}_2\text{-SiC-B}_4\text{C-PR-B-D-S}$ heated at $10^{\circ}\text{C}/\text{min}$ in flowing helium	122
5.8	Temperature (Temp) and species intensity of the $m/z=29, 31, 43, 45, 91, 94, 106,$ and 108 signals versus time for 0.5 g of $\text{ZrB}_2\text{-SiC-B}_4\text{C-PR-B-D-S}$ heated at $10^{\circ}\text{C}/\text{min}$ in flowing helium	123
5.9	Temperature (Temp), length change (Dil), and species intensity of the $m/z=12, 16, 28, 44,$ and 45 signals versus time for 0.8 g of $\text{ZrB}_2\text{-5-ZrSi}_2$ heated at $14^{\circ}\text{C}/\text{min}$ in flowing helium	126
5.10	Temperature (Temp), length change (Dil), and species intensity of the $m/z=12, 16, 28, 44,$ and 45 signals versus time for 0.8 g of $\text{ZrB}_2\text{-10-ZrSi}_2$ heated at $14^{\circ}\text{C}/\text{min}$ in flowing helium	128
5.11	Temperature (Temp), length change (Dil), and species intensity of the $m/z=12, 16, 28, 44,$ and 45 signals versus time for 0.8 g of $\text{ZrB}_2\text{-20-ZrSi}_2$ heated at $14^{\circ}\text{C}/\text{min}$ in flowing helium	130

LIST OF TABLES

Table	Page
1.1 Sintering types, mechanisms, and driving forces [Adapted from [1]]	3
1.2 Three stages of sintering [Adapted from [1]]	4
2.1 PID settings recommended by Linseis for a single thermocouple system [1]	24
2.2 Dilatometer settings for data acquisition [1]	31
2.3 Mass spectrometer settings that make up a Method [1]	32
2.4 Steps for dilatometer data analysis [1]	32
3.1 Heating cycles with atmosphere, heating and cooling rates, and high temperature holds and times performed with the CDMS	39
3.2 Species and natural isotopic abundances for C, O, S, and Ti [15]	40
3.3 Comparison of normalized m/z ratios evolved from the inert conditioning and the background cycles and tabulated values corresponding to the cracking pattern (CP) for oxygen and sulfur dioxide [14]	42
3.4 Comparison of normalized m/z ratios evolved from barium sulfate, barium carbonate, barium titanate, and carbon dioxide, and tabulated values for the isotopes of carbon dioxide [15]	43
3.5 Comparison of normalized m/z ratios evolved from barium sulfate and barium titanate, tabulated values for the isotopes of sulfur [15], and tabulated values corresponding to the cracking pattern (CP) for sulfur dioxide [14]	49
3.6 Comparison of relative density, linear shrinkage, sintering temperature, regions of similar signals starting temperatures, and peaks of the m/z=44 and 64 signals between barium titanate samples at different heating and cooling rates and between pressed and loose powder	55
3.7 Comparison of normalized isotope ratios that would be expected for TiO and observed data evolved at 900°C during the heating of barium titanate [15]	60

4.1	Components of boron nitride spray with the boiling temperature of each and four most abundant m/z ratios of the CPs [24].....	79
4.2	Heating and cooling rates, low and high temperature holds and times for samples examined.....	80
4.3	Select boron nitride spray CP mass to charge ratio with possible sources and possible chemical structures [24].....	84
4.4	Comparison of normalized m/z ratios evolved from zirconium diboride, boron carbide, silicon carbide, and carbon dioxide, and tabulated values corresponding to the cracking pattern (CP) for carbon monoxide [24].....	89
4.5	Comparison of normalized m/z ratios evolved from zirconium oxide, carbon dioxide, barium titanate, and strontium titanate.....	97
5.1	Heating and cooling rates, low and high temperature holds and times for different samples.....	109
5.2	Comparison of normalized m/z ratios evolved from phenolic resin, ZrO ₂ -B ₄ C, ZrB ₂ -B ₄ C-PR, ZrB ₂ -SiC-B ₄ C-PR-B-D-S, ZrB ₂ -5, -10, & -20-ZrSi ₂ , ZrB ₂ , B ₄ C and CO ₂ gas, and the isotopes for CO ₂ [21].....	114
5.3	Comparison of normalized m/z ratios evolved from ZrO ₂ -B ₄ C and the isotopes for CO [21].....	116
5.4	Temperatures of the major m/z=28 signal onset and peak and the onset of the sample length change, along with the final relative theoretical density for the ZrB ₂ -5-ZrSi ₂ , ZrB ₂ -10-ZrSi ₂ , and ZrB ₂ -20-ZrSi ₂ samples	131

**COMBINED DILATOMETRY AND MASS SPECTROMETRY OF SINTERING
AND EVOLVED GASES OF BARIUM TITANATE AND ZIRCONIUM
DIBORIDE WITH SINTERING ADDITIVES**

Murray Moss

Dr. Stephen J. Lombardo

Thesis Supervisor

ABSTRACT

The system components, improvements, and procedures of a combined dilatometer mass spectrometer system (CDMS) are described in detail. The CDMS is used to monitor the gas phase species and sintering progress in real time during the heating of barium titanate and ultra high temperature ceramics (UHTCs), including zirconium diboride and sintering additives. For loose powder and pressed samples of barium titanate heated at different rates, two families of signals were observed by mass spectrometry at mass to charge (m/z) ratios of 44 and 64 prior to the onset of sintering, which initiated at 1150°C. The assignment of these signals as carbon dioxide and sulfur dioxide was accomplished using reference cracking patterns, natural isotope abundances, a carbon dioxide gas reference, and comparison to the gases evolved from the model compounds barium carbonate and barium sulfate. The sources for carbon dioxide evolution at low temperatures below 500°C include organic impurities arising from processing, exposure to ambient organic material, and adsorbed carbon dioxide. The sources for the higher temperature above 600°C evolution of carbon dioxide and sulfur

dioxide are likely from residual unreacted or surface barium carbonate and barium sulfate, respectively.

The UHTCs and common sintering aids heated in the CDMS individually and in mixtures include zirconium diboride, boron carbide, silicon carbide, boron oxide, zirconium oxide, zirconium disilicide, boron nitride spray, and organic binder, dispersant, and surfactant. Low temperature signals below 660°C for these UHTCs are attributed to the decomposition of organics present in the boron nitride spray, binder, dispersant, and surfactant. The high temperature signals above 900°C were determined to be CO and CO₂ using reference cracking patterns and natural isotope abundances. The carbon sources are identified as arising from unreacted carbon from the synthesis methods for some of the powders and from the carbon inherent in the chemical formula. The oxygen sources were attributed to synthesis reactions for the powders and to the presence of surface oxides. An additional source for CO and CO₂ production at high temperature for the powders in mixture is the reactive sintering that occurs. Zirconium disilicide was the only additive that decreased the sintering temperature of zirconium diboride below the maximum hold temperature of 1648°C, thereby allowing sintering to occur.

Chapter 1

Introduction

1.1 General Background

Ceramic materials can be divided into general groups: traditional ceramics and advanced ceramics. Traditional ceramics such as concrete, whitewares, and refractories have in the past and continue to hold a large portion of the ceramics industry and are used for their strength, hardness, and thermal stability at high temperatures. Advanced ceramics are included in applications that utilize the electrical, magnetic, structural, chemical, and optical properties of the compounds, which can be modified through doping of the bulk material with a smaller amount of another material. The difficulty in machining most ceramics because of their high hardness and brittleness had led to the development of the near net shape forming method of powder processing. In powder processing, the solid ceramic particles are pressed into a shape, called the green body, which is then heated or "sintered" to remove the pores between particles. The body experiences many types of mass transport and chemical changes during sintering, all of which can greatly influence the properties of the dense finished body.

Table 1.1 summarizes the different mechanisms that can occur during sintering, along with both the transport mechanisms and driving forces behind each. These mechanisms can occur as a solitary mechanism or can occur along with one or more other mechanisms. The sintering of BaTiO_3 , for example, is mostly solid-state sintering but includes surface diffusion, vapor transport, volume diffusion, and grain boundary diffusion (see Figure 1.1) [1]. Grain boundary diffusion and volume diffusion are the only transport types of the four listed to bring the centers of particles closer together, resulting in densification. Surface diffusion and vapor transport do not contribute to densification because they only involve molecules on the surface of the material.

Table 1.1: Sintering types, mechanisms, and driving forces [Adapted from [1]].

Type of Sintering	Transport Mechanism	Driving Force
Vapor-phase	Evaporation/condensation	Difference in vapor pressure
Solid-state	Diffusion	Differences in free energy or chemical potential
Liquid-state	Viscous flow, diffusion	Capillary pressure, surface tension
Reactive liquid	Viscous flow, solution precipitation	Capillary pressure, surface tension

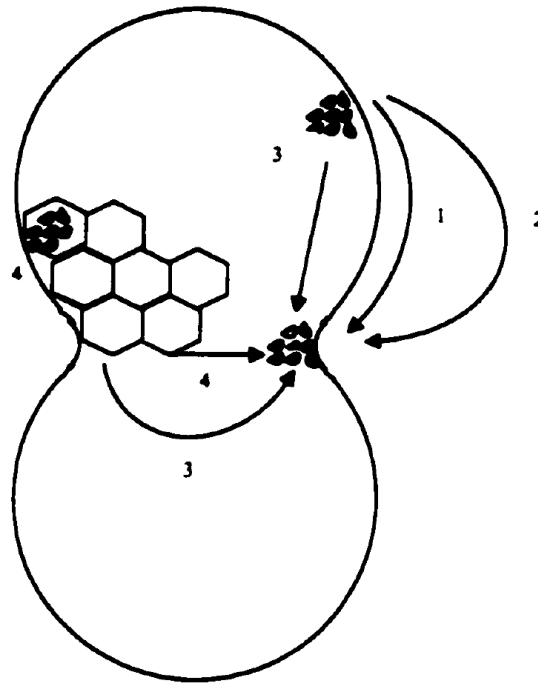


Figure 1.1: Material transport mechanisms contributing to the sintering of a consolidated mass of polycrystalline particles: (1) surface diffusion, (2) vapor transport, (3) volume diffusion, and (4) grain boundary diffusion [1].

The process of sintering is divided into three stages, according to the physical changes and methods of material transport that occur, as listed in Table 1.2. Figure 1.2 illustrates how the rearrangement of particles and initial neck formation by surface diffusion is observed in the initial stage. The mechanisms in first stage have relatively low activation energy and cause an increase in contact between particles.

Table 1.2: Three stages of sintering [Adapted from [1]].

Sintering stage	Physical changes
First stage (initial)	Rearrangement
	Neck formation
Second stage (intermediate)	Neck growth
	Grain growth
	High shrinkage
Third stage (final)	Pore phase continuous
	Much grain growth
	Discontinuous pore phase
	Grain boundary pores eliminated

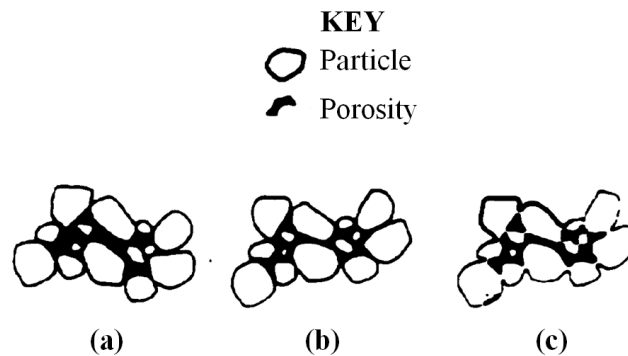


Figure 1.2: Physical states during the initial stage of sintering. (a) Starting particles, (b) rearrangement, and (c) neck formation [1].

The intermediate sintering stage is when most of the shrinkage, caused by grain boundary diffusion, occurs as shown in Figure 1.3. The grain boundary diffusion causes pores to move to the exterior of the interface, which takes place as grain and neck growth occurs. The intermediate stage ends when the pore channels are closed and the pores become isolated.

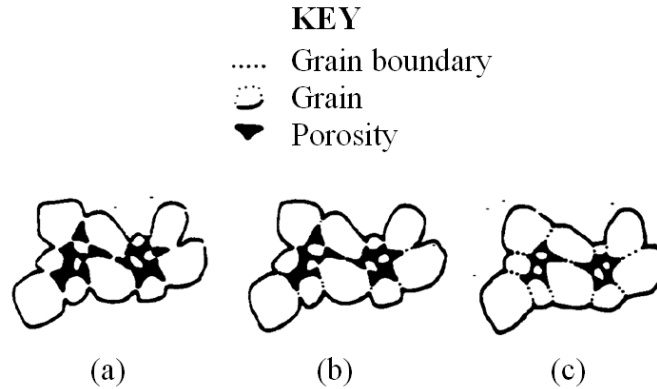


Figure 1.3: Physical states during the intermediate stage of sintering. (a) Neck growth and volume shrinkage, (b) lengthening of grain boundaries, and (c) continued neck growth and grain boundary lengthening, volume shrinkage, and grain growth [1].

Figure 1.4 shows the final stage of sintering, which continues densification by the elimination of almost all porosity through surface diffusion along grain boundaries. This surface diffusion is accomplished by the diffusion of vacancies in the crystal lattice and aided by grain boundary movement and grain growth. The control of grain growth determines how much porosity remains; sintering that occurs too quickly can trap pores in the final microstructure.

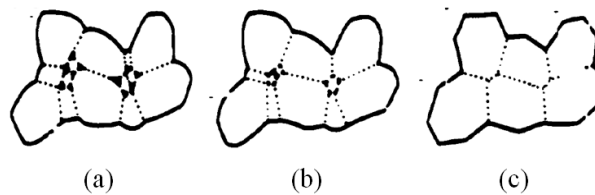


Figure 1.4: Physical states during the final stage of sintering. (a) Grain growth with discontinuous pore phase, (b) grain growth with porosity reduction, and (c) grain growth with porosity elimination [1].

1.2 Analysis Techniques

Dilatometry is the most common method of determining sintering progress. Sintering causes a significant volume change in a material which corresponds to changes in length of the sample that is then measured by the dilatometer. The length change as a function of time or temperature can then be used to find the activation energy of sintering, which is the energy needed to rearrange the particles of the material to a lower energy state. The changes in the microstructure as a result of sintering cannot be monitored in real time, but can be examined when the sample is rapidly cooled, cut, polished, and then analyzed using other equipment, such as a scanning electron microscope (SEM) or X-ray diffraction (XRD).

In order to identify species that are evolved in the gas phase during the heating of inorganic materials to high temperatures, different techniques have been discussed elsewhere [2-6]. A Knudsen diffusion cell is one method, where the material is heated and the evolved species are directly monitored or captured for later analysis. Another method uses a carrier gas that flows around the heated material to transport the evolved gas species to the analyzer. The Knudsen method is for measuring in chemical equilibrium conditions, but the carrier gas method can be used in non-equilibrium conditions, which are present during sintering. None of the various methods used for analyzing chemical processes that occur during sintering have emerged as a clear standard.

The above techniques have provided a great deal of information into reactions that occur at high temperatures, but there is not as much in the literature that discusses the connection between such reactions and the rate of sintering of ceramics. The exploration

of the concentrations and temperatures at which species are evolved and their effect on sintering and final microstructure could lead to major changes in how ceramics are processed. Possible reactions [3-41] that occur at high temperatures are the decomposition of organic material, the evolution of sintering aids, and the removal or modification of surface layers. Apart from the reactions that occur from the sample, the furnace environment may affect sintering by contributing to or initiating reactions [40].

The combination of both high temperature dilatometers [27-36] and mass spectrometers [14, 16-18, 34, 35] is not common; however, the results from such measurements could be utilized to expand on the knowledge that has been gained from each analytical device independently. To demonstrate the possible uses of these types of measurements, Honstein et al. [42] investigated the effect of heat treatments and varying $\text{SiO}_2\text{:SiC}$ ratio on the evaporation behavior of SiC by monitoring the evolution of CO and SiO gas using a mass spectrometer. The SiO gas pressure was decreased with the presence of excess SiO_2 which was explained by two steady-state vaporization processes. A study by Baud et al. [43] using mass spectrometry revealed that the vaporization processes of the $\text{SiC-Al}_2\text{O}_3$ powder bed system are not in equilibrium and are kinetically hindered. From these results, a more fitting powder bed can be developed for the sintering of oxide-containing SiC. The benefits of using mass spectrometry in order to identify reactions that occur, which can influence sintering behavior and final microstructure, are summarized in the two examples above.

1.3 Motivation, Objective, and Thesis Organization

The motivation for this work is the continued development of the combined dilatometer mass spectrometer (CDMS) as a characterization tool that can be used to expand the knowledge of reactions that occur during the heating of various ceramic systems through the real time monitoring of gas phase species. The development of the CDMS will allow for the observation of how starting powder characteristics affect gas phase reactions, which can then affect the sintering behavior along with the final microstructure and properties of the ceramic. The data provided by the CDMS can be combined with other analytical techniques to generate tailored sintering cycles that optimize desired properties while minimizing production costs.

The main objective of this work is to identify the sources of all the evolved species for each ceramic powder system that was heated in the CDMS. As previously mentioned, there are many possible sources for gas phase species, including species originating from the ceramic powder and from the furnace environment. Another objective that is addressed in this work is the improvement of both the CDMS apparatus and the methods for the use of the CDMS. These improvements allow a wider variety of ceramic powders to be analyzed using the CDMS and decrease the amount of background signals present in the CDMS.

Chapter 2 details the CDMS and outlines the general procedures used to measure the progress of sintering and the evolved gases in real time. Diagrams showing the coolant liquid flow path that cools both the furnace and dilatometer and for both the tube and shell side gas flow paths are provided. The chapter also discusses how the procedure has been improved to include oxidizing and inert conditioning heating cycles between

samples to remove residual species that may be present on the interior surfaces of the furnace. The primary thermocouple is now separated from gas phase species that can cause degradation using a thermocouple protection tube and the powder pressing procedure has been modified to reduce background signals.

In chapter 3, the CDMS is used to examine high temperature chemistry that occurred during the sintering of barium titanate at varied heating rates and as both pressed and loose powder. Barium titanate is a ferroelectric material that, through doping with metal oxides, has highly modifiable electrical properties which has led to its development into widespread use in capacitors. The synthesis routes of barium titanate, from the mineral barite (BaSO_4) to barium carbonate, which is then mixed with titanium dioxide to produce barium titanate, allows for the introduction of several impurities into the final powder that could potentially be evolved into the gas phase.

The high temperature chemistry of carbides, oxides, and other additives that are commonly combined for ultra-high temperature applications were examined using the CDMS individually in chapter 4 and combined in chapter 5. Ultra-high temperature ceramics (UHTCs) are utilized as refractories, electrodes, and structural components in high temperature and high chemical reactivity environments. Classes of UHTCs that are currently being explored include borides, which have excellent hardness and thermal and electrical conductivity, along with stable oxides, and carbides, which have higher melting temperatures and high strength. Because of the high melting temperatures of the UHTCs, and therefore high sintering temperatures, additives such as B_4C , SiC , excess carbon in the form of phenolic resin, and ZrSi_2 , have been incorporated into the UHTCs. These additives can have multiple effects on the powder system, such as improving or

worsening desired physical properties, removing surface oxide layers, and reducing the sintering conditions which expands the techniques available for sintering. These powders are reactive systems that produce species in the gas phase during heating, which will be monitored by the CDMS.

1.4 References

1. D. W. Richerson, *Modern Ceramic Engineering*. Marcel Dekker, New York, 1992.
2. J. L. Margrave, *The Characterization of High-Temperature Vapors*. John Wiley & Sons, New York, 1967.
3. J. H. Hastie, *High Temperature Vapors: Science and Technology*. Academic Press, New York, 1975.
4. *Characterization of High Temperature Vapors and Gases, Vol. 1*, Edited by J. H. Hastie, NBS Special Publication 561, U. S. Department of Commerce, 1979.
5. G. A. Somorjai, "Studies of the Sublimation Mechanism of Solids," in *Advances in High Temperature Chemistry, Vol. 2*, Edited by L. Eyring, Academic Press, New York, 1969.
6. W. L. Worrel, "Dissociation of Gaseous Molecules on Solids at High Temperature" in: *Advances in High Temperature Chemistry, Vol. 4*, L. Eyring, Academic Press, New York, 1971.
7. D. A. Northrop, "Vaporization of Lead Zirconate-Lead Titanate Materials"; *J. Am. Ceram. Soc.*, **50** 441-45 (1967).
8. D.A. Northrop, "Vaporization of Lead Zirconate-Lead Titanate Materials: II, Hot-Pressed Compositions at Near Theoretical Density"; *J. Am. Ceram. Soc.*, **51** 357-61 (1968).
9. R.B. Atkin and R.M. Fulrath, "Point Defects and Sintering of Lead Zirconate-Titanate"; *J. Am. Ceram. Soc.*, **54** 265-70 (1971).
10. R.L. Holman and R.M. Fulrath, "Intrinsic Nonstoichiometry in Single Phase $\text{Pb}(\text{Zr}_{.5}\text{Ti}_{.5})\text{O}_3$ "; *J. Am. Ceram. Soc.*, **55** 192-97 (1972).
11. A.I. Kingon and J.B. Clark, "Sintering of PZT Ceramics: I, Atmosphere Control"; *J. Am. Ceram. Soc.*, **66** 253-56 (1983).
12. A.I. Kingon and J.B. Clark, "Sintering of PZT Ceramics: II, Effect of PbO Content on Densification Kinetics"; *J. Am. Ceram. Soc.*, **66** 256-60 (1983).
13. B.V. Hiremath, A.I. Kingon, and J.V. Biggers, "Reaction Sequence in the Formation of Lead Zirconate-Titanate Solid Solution: Role of Raw Materials"; *J. Am. Ceram. Soc.*, **66** 790-93 (1983).
14. K.H. Hardtl and H. Rau, "PbO Vapor Pressure in the $\text{Pb}(\text{Ti}_{1-x}\text{Zr}_x)\text{O}_3$ System"; *Solid State Commun.*, **7** 41-45 (1969).

15. N.G. Schmahl, G.K. Schwitzgebel, H. Kling and E. H. Speck, "Thermodynamic Investigations of the Solid Solution of Lead Zirconate–Titanate"; *Mater. Res. Bull.*, **14** 1213-1218 (1979).
16. Popovic, B. Malic, and L. Bencze, "Knudsen Cell Mass Spectrometric Investigation of the PbO-ZrO₂-TiO₂ System"; *Rapid Commun. Mass Spectrom.*, **13** 1129-37 (1999).
17. P. Rocabois, C. Chatillon, and C. Bernard, "Thermodynamics of the Si-O-N System: I, High-Temperature Study of the Vaporization Behavior of Silicon Nitride by Mass Spectrometry"; *J. Am. Ceram. Soc.*, **79** 1351-60 (1996).
18. S.-S. Lin, "Mass Spectrometric Analysis of Vapors in Oxidation of Si₃N₄ Compacts"; *J. Am. Ceram. Soc.*, **58** 160 (1975).
19. M. A. Mulla, V. D. Krstic, "Pressureless Sintering of β -SiC with Al₂O₃ Additions"; *J. Mater. Sci.*, **29** 934-38 (1994).
20. T. Grande, H. Sommerset E. Hagen, K. Wiik, and M. Einarsrud, "Effect of Weight Loss on Liquid-Phase-Sintered Silicon Carbide"; *J. Am. Ceram. Soc.*, **80** 1047-52 (1997).
21. W. van Rijswijk, "Effect of Carbon as a Sintering Aid in Silicon Carbide"; *J. Am. Ceram. Soc.*, **73** 148-49 (1990).
22. W. J. Clegg, "Role of Carbon in the Sintering of Boron-Doped Silicon Carbide"; *J. Am. Ceram. Soc.*, **83** 1039-43 (2000).
23. T. Quadir and D. W. Readey, "Microstructure Development of Zinc Oxide in Hydrogen"; *J. Am. Ceram. Soc.*, **72** 297-302 (1989).
24. H. Wada, Ming-Jong Wang, and Tseng-Ying Tien, "Stability of Phases in the Si-C-N-O System"; *J. Am. Ceram. Soc.*, **71** 837-40 (1998).
25. U. Neidhardt, H. Schubert, E. Bischoff, and G. Petzow, "Gas Pressure Sintering of Si₃N₄ in N₂/CO/CO₂ Atmosphere"; *Key Engineer. Mater.*, **89-91** 187-92 (1994).
26. E. A. Ness, and W. Rafaniello, "Origin of Density Gradients in Sintered β -Silicon Carbide Parts"; *J. Am. Ceram. Soc.*, **77** 2879-84 (1994).
27. H. Lee and R.F. Speyer, "Pressureless Sintering of Boron Carbide"; *J. Amer. Ceram. Soc.*, **86** 1468-73 (2003).
28. C. Boberski, H. Bestgen, and R. Hamminger, "Microstructural Development during Liquid-Phase Sintering of Si₃N₄ Ceramics"; *J. Eur. Ceram. Soc.*, **9** 95-99 (1992).

29. J. Jung, "Body-Controlled Sintering and Differential Thermal Analysis up to 2400°C"; *Keramische Zeit.*, **42** 830-32 (1990).
30. O. Abe and S. Kanzaki, "High-Temperature Dilatometer for Non-Oxide Ceramics"; *J. Ceram. Soc. Japan*, **97** 187-91 (1989).
31. M. L. Mecartney, "Influence of Dissolved Si₃N₄ on the Properties of Al₂O₃-MgO-SiO₂ Glass"; *J. Mat. Sci. Lett.*, **6** 370-72 (1987).
32. H-J. Kleebe, W. Braue, and W. Luxem, "Densification Studies of SRBSN with Unstabilized Zirconia by Means of Dilatometry and Electron Microscopy"; *J. Mat. Sci.*, **29** 1265-75 (1994).
33. S. Siegel, M. Hermann, and G. Putzky, "Effect of Process Atmosphere on Dilatometer Controlled Sintering"; *Key Engineer. Mater.*, **89-91** 237 (1994).
34. L. Chen, W. Lengauer, P. Ettmayer, K. Dreyer, H.W. Daub, and D. Kassel, "Fundamentals of Liquid Phase Sintering for Modern Cermets and Functionally Graded Cemented Carbonitrides (FGCC)"; *Inter. J. of Refractory & Hard Metals*, **18** 307 (2000).
35. L. Chen, W. Lengauer, and K. Dreyer, "Advances in Modern Nitrogen-Containing Hardmetals and Cermets"; *Inter. J. of Refractory & Hard Metals*, **18** 153-61 (2000).
36. E.A. Oliber, E.R. Benavidez, G. Requena, J.E. Fiscina, and C.J.R. Gonzalez Oliver, "High Temperature Reactions, Densification and the Peritectic Decomposition of YBa_{2-x}Sr_xCu₃O_{7-δ} (YBCO) Superconducting Ceramics"; *Physica C*, **384** 247-257 (2003).
37. H. Ishida, Nanri, Sh. Takechi, N. Watanabe, and K. Wakamatsu, "Oxidation Behavior of Si₃N₄ at Low Oxygen Partial Pressures"; *J. Soc. Mat. Sci. Japan*, **45** 694-99 (1996).
38. D.F. Carroll, A.W. Weimer, S.D. Dunmead, G.A. Eisman, J.H. Hwang, G.A. Cochran, D.W. Susnitzky, D.R. Beaman, and C.L. Conner, "Carbothermally Prepared Nanophase SiC/Si₃N₄ Composite Powders and Densified Parts"; *AIChE J.*, **43** 2624-35 (1997).
39. K. Feng and S. J. Lombardo "Kinetic Analysis from Dilatometry and Mass Spectrometry Measurements of the Decomposition and Sintering of Calcium Carbonate"; *J. of Ceram. Proc. Res.*, **3** 101-108 (2002).
40. K. Feng and S. J. Lombardo, "High-Temperature Reaction Networks in Graphite Furnaces," *J. of Mat. Sci.*, **37** 2747 (2002).

41. M. Schurwanz, J. W. Yun, C. S. Kim, and S. J. Lombardo, "Evolved Gas Analysis During Sintering of Strontium Titanate," *Adv. Appl. Ceram.*, **111** 443 (2012).
42. G. Honstein, C. Chatillon, and F. Baillet, "High Temperature Mass Spectrometric Study of the Vaporization Behaviour of SiC-SiO₂ System," *Journal of Alloys and Compounds*, **452** 85 (2008).
43. S. Baud, F. Thevenot, and C. Chatillon, "High Temperature Sintering of SiC with Oxide Additives: III. Quantitative Vaporization of SiC-Al₂O₃ Powder Beds as Revealed by Mass Spectrometry," *Journal of the European Ceramic Society*, **23** 19 (2003).

Chapter 2

Experimental and System Details

2.1 Introduction

This chapter discusses the components of the combined dilatometer mass spectrometer (CDMS), which is used to measure the rate of sintering and the evolved gas species from the sample in real time during heating. The hardware and software type and setup are discussed, along with improvements to the system and the experimental procedure executed. For further information on the CDMS see Schurwanz [1].

2.1.1 System Overview

The combined dilatometer mass spectrometer (CDMS) includes a pushrod dilatometer (Push-Rod Dilatometer, L-75/260, Linseis, Selb, Germany) and high temperature furnace (High Temperature Tube Furnace, 1640, Thermal Technologies, Santa Rosa, CA) in conjunction with a mass spectrometer (Quadrupole Mass Filter Spectrometer, 5971A, Agilent Technologies, Santa Clara, CA). There are two gas flow paths that are separated by an alumina combustion tube (Combustion Tube, 30505-modified, McDanel Advanced Ceramic Technologies, Beaver Falls, PA), the Tube Side and the Shell Side, along with two flow paths that carry coolant to the furnace and dilatometer. The Tube Side flow path is along the interior of the dilatometer and combustion tube, and then is split near the exit of the furnace by a T-junction to enter either the mass spectrometer or to vent. The Shell Side flow path is along the exterior of the combustion tube and in the shell of the furnace that contains the graphite heating element and graphite insulating felt, and then is vented. The separation of the two gas flow paths allows for an inert atmosphere that is necessary for the graphite heating elements in the furnace and for another inert carrier gas that is not exposed to the heating

elements to enter the mass spectrometer. The liquid flow paths consist of one path between the furnace shell, the chiller, and the circulator and another path between the circulator and the housing around the dilatometer.

2.2 System Details

2.2.1 Coolant Flow Paths

Figure 2.1 shows how the shell of the furnace is cooled by circulating coolant that travels from the furnace, through a flow indicator, to the chiller, through the circulator, and back to the furnace. If the flow indicator detects that the water flow is halted during furnace use, the power to the furnace will be shut off. The section of the dilatometer that connects the end of the alumina sample holder to the metal mounting apparatus is cooled by water that is pumped from the circulator [1].

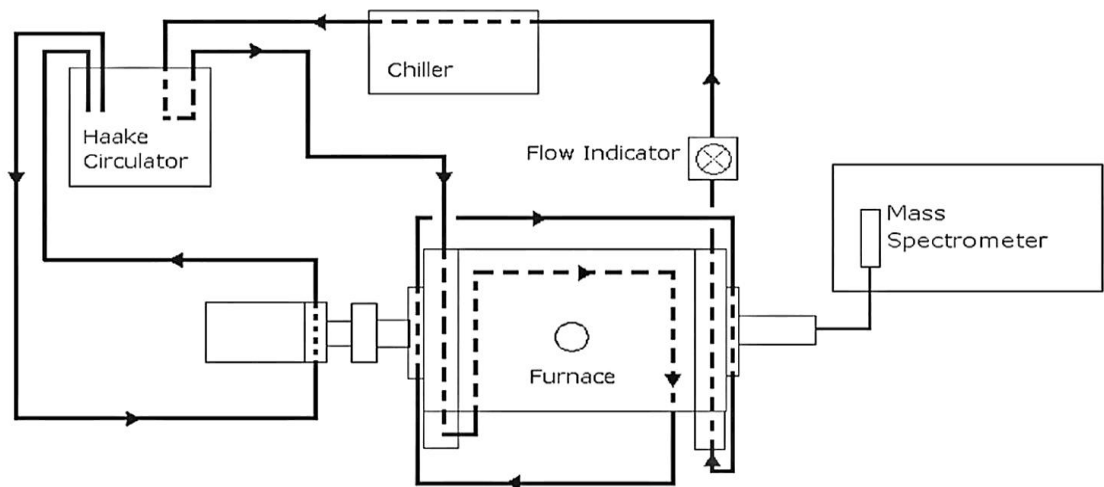


Figure 2.1: Diagram of the liquid flow paths for the CDMS [1].

2.2.2 Gas Flow Paths

The Tube Side gas flow path initiates at high pressure gas cylinders that then flow gas to a mixing board (FL-5GP-41SA-41SA, Omega Engineering, Stamford, CT), where up to three gases can be mixed and flow rates can be established for each as seen in Figure 2.2. The gas is then directed into the dilatometer and to the interior of the combustion tube in the furnace where it passes over the sample. The gas exits the furnace where part of the gas is siphoned to the mass spectrometer via a silica capillary and the rest of the gas is vented [1].

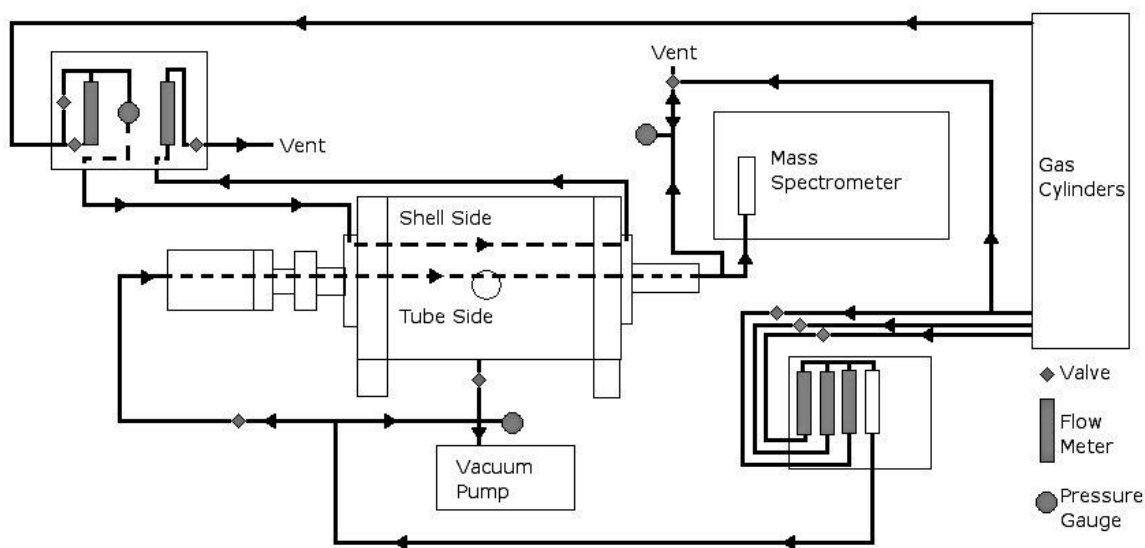


Figure 2.2: Diagram of the gas flow paths for the CDMS [1].

The furnace and mass spectrometer are connected by a series of bellows, tubing, and fittings through which a silica capillary (B) runs along the entire length as shown in Figure 2.3. One set of bellows connects to an end flange (F) of the furnace and also has a fitting with a floating o-ring that encases the restricted end of the alumina combustion tube (between F & G). This prevents damage to the alumina combustion tube from the

length expansion during heating and maintains the separation of the gases in tube and shell sides of the furnace. The bellows should measure 7.8 cm long when the shell is under vacuum and should measure 8.3 cm when the shell is close to atmospheric pressure. If the bellows are extended past those lengths, the fitting that is on the end of the combustion tube may need to be adjusted to sit tighter on the end of the tube. Connected to the fitting on the bellow is a series of tubing that includes a T-junction where one arm continues to either vent or rapid fill and the other arm continues to the mass spectrometer. The tubing connects to a gas chromatography inlet heater that maintains the tubing at around 320°C. The resistance of the resistance temperature detector can be measured and related to the temperature by the following equation:

$$T_{Inlet\ Heater}(^{\circ}C) = 2.6445 * \Omega(ohms) - 265.11 \quad 2.1$$

A bellows connects the GC inlet heater to the mass spectrometer to allow shifting to occur throughout the furnace and mass spectrometer interface during evacuating and filling of the shell side [1].

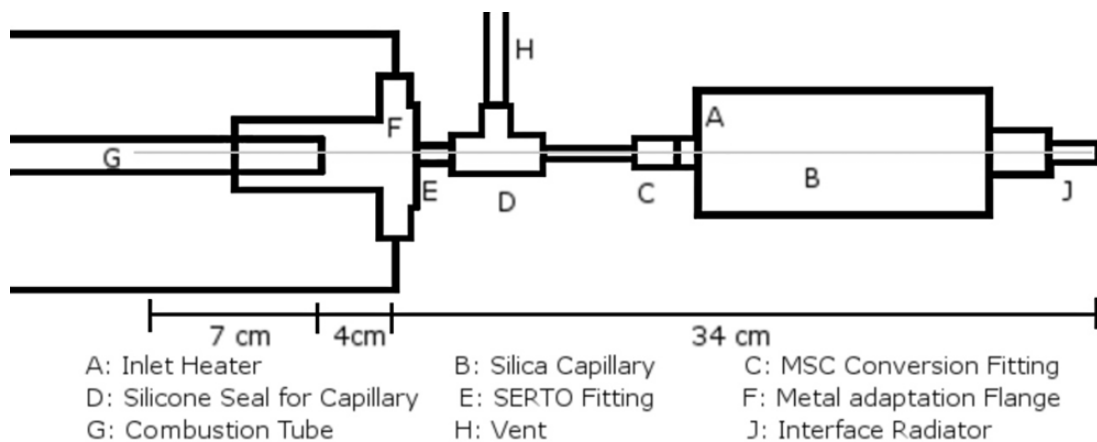


Figure 2.3: Diagram of the furnace to mass spectrometer interface [1].

2.2.3 Dilatometer

The sample, usually between 0.2 and 1 g, is placed in an alumina sample holder and suspended between two spacers that are held in place by the alumina pushrod of the dilatometer and an alumina key that acts as a stationary wall; this setup can be seen in Figure 2.4. The spacers are 5 mm in diameter and 0.7 mm thick and the composition depends on the composition of the sample. Calcia-stabilized zirconia was used for the barium containing ceramic powders and alumina was used for the zirconium containing ceramic powders. Low density alumina paper is also placed in the sample holder, covering the area directly beneath the sample, spacers, and pushrod in order to protect the sample holder from pieces of the sample that could potentially break off during loading or during the heating cycle. The sample holder slides into the interior of the combustion tube in the furnace and is sealed by a high vacuum fitting [1].

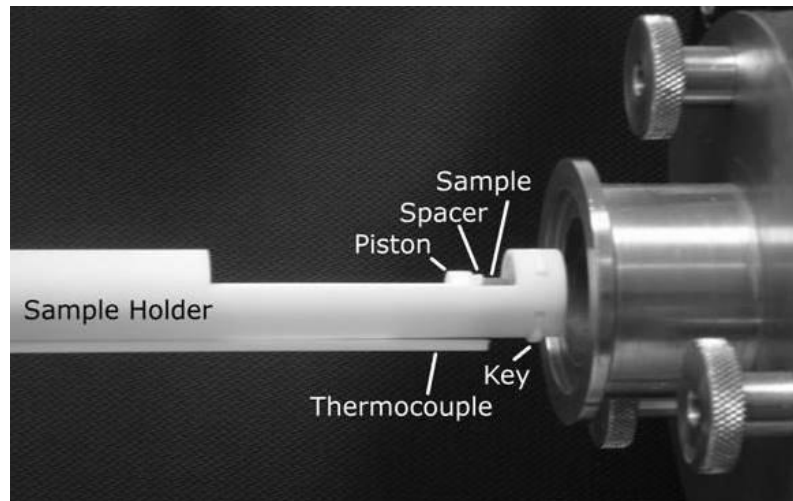
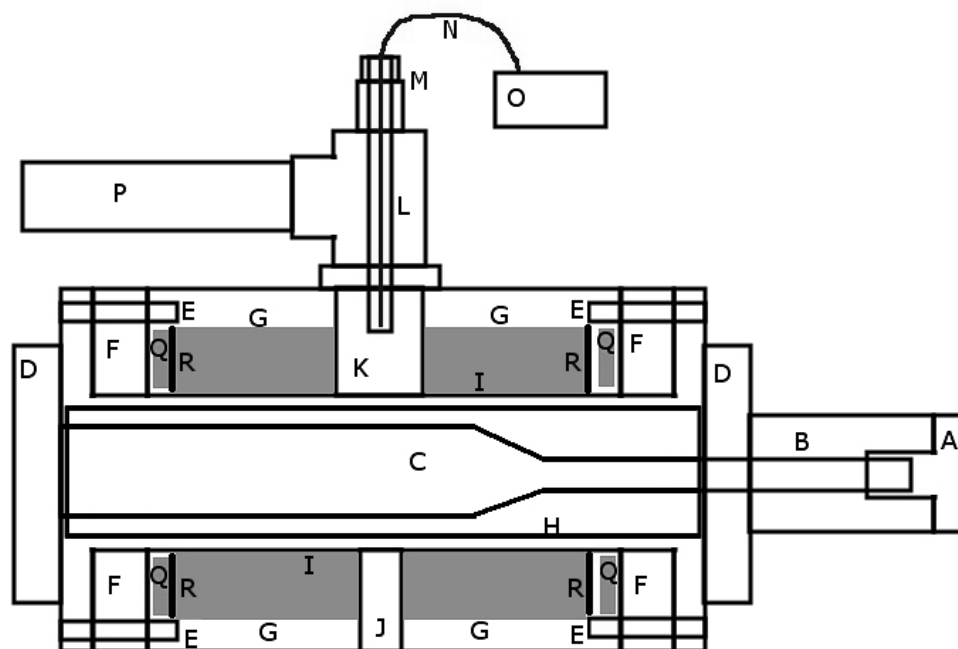


Figure 2.4: Image of the positioning of the sample and spacers in the dilatometer [1].

2.2.4 Furnace

Figure 2.5 shows the furnace components and the position of the cylindrical graphite heating element for heating, surrounded by graphite insulating felt inside a felt retainer. A vacuum port is located in the rear of the furnace and has a T-section attached to it that allows for both venting of the shell side and the space for a thermocouple. The furnace also features a viewing port that provides a line of sight to the heating element and would allow the temperature to be read by an optical pyrometer. The hole through the felt is framed by a graphite cylinder and the window is made of quartz [1].

The furnace is separated by the alumina combustion tube into the tube side, or interior of the tube where the sample holder enters, and the shell side, which houses the graphite heating element and thermal insulation. The combustion tube is fixed firmly to one of the flanges of the furnace by applying the silicon gasket maker (Ultra Blue Silicone Gasket Maker, 77B, Permatex, Hartford, CT) that is thermally stable up to 260 °C. Figure 2.6 shows the combustion tube in our system as a modified version of the McDanel Ceramics 30505 combustion tube, shortening both ends to an overall length of 17 and 5/8 inches and adding a bevel to the restricted end to prevent chipping.



- | | | |
|--------------------|-------------------------|------------------------|
| A: Adaptor Flange | G: Graphite Felt | M: Ultra Torr Fitting |
| B: Bellows | H: Heating Element | N: Safety Thermocouple |
| C: Combustion Tube | I: Radial Felt Retainer | O: Safety Controller |
| D: End Flanges | J: Sighting Tube | P: to Vacuum |
| E: Hex Screw Wells | K: Vacuum Port | Q: Felt Spacer |
| F: Electrodes | L: Thermocouple Tube | R: Axial Felt Retainer |

Figure 2.5: Cross section diagram of the furnace [1].

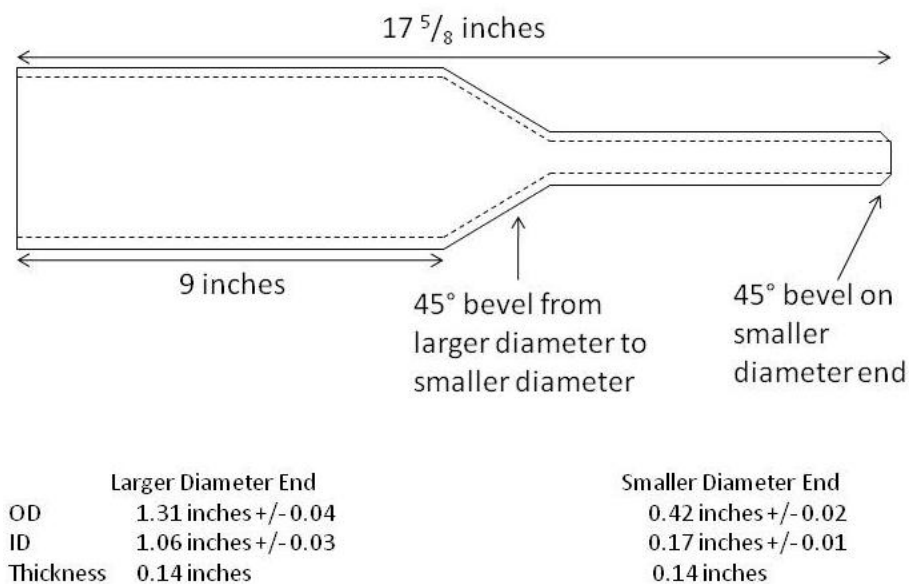


Figure 2.6: Alumina combustion tube dimensions, modified from McDanel Ceramics combustion tube 30505.

The temperature in the furnace is measured using two type B thermocouples, (17 inch butt-welded, unsheathed, type B thermocouple, P30R-010-BW-17, Omega Engineering, Stamford, CT) with PID controller settings listed in Table 2.1. One, the primary thermocouple, is located on the underside of the sample holder and the other, the safety thermocouple, is located opposite of the viewing port. The actual temperature is consistently lower than the calculated temperature by about 10°C, as seen in Figure 2.7, which is an artifact from the furnace controller settings. The primary thermocouple should be aligned so that the tip is directly under the sample to get the most accurate temperature reading in the hot zone of the furnace, which is about 5 cm long. Figure 2.8 shows the primary thermocouple encased in a closed one end alumina tube 12 inches long with 3.0 mm OD and 1.5 mm ID (Ceramic Thermocouple Protection Tube, PTR-11618-12, Omega Engineering, Stamford, CT) with another alumina tube 12 inches long with 0.78 mm OD and 0.5 mm ID (Single-Bore Extruded Alumina Tube, 031020AE, Accuratus Ceramic Corporation, Phillipsburg, NJ) around one of the thermocouple leads to protect the thermocouple from chemical attack. This thermocouple protection tube system was devised after it was discovered that primary thermocouples were being degraded and failing due to carbon replacement of platinum at high temperatures. The lead wires of the primary thermocouple exiting the alumina tubes are protected by insulation taken from old wires as they travel back to the thermocouple lead connectors in the dilatometer.

Table 2.1: PID settings recommended by Linseis for a single thermocouple system [1].

		Controller 1	Controller 2
Proportional	(P)	0	200
Integral	(I)	0	1100
Derivative	(D)	0	0

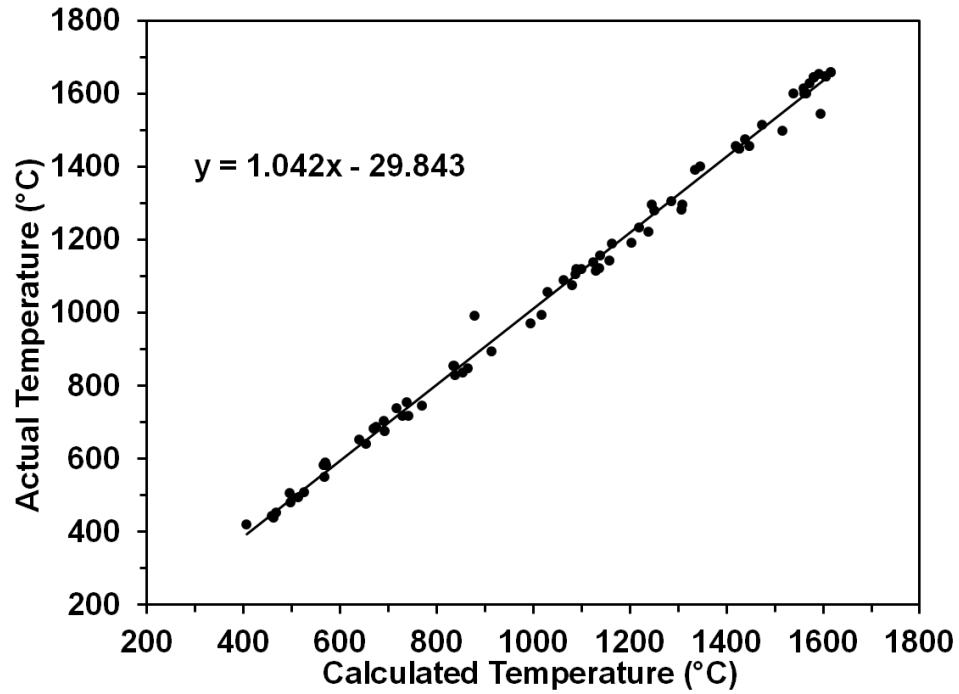


Figure 2.7: Actual temperature versus calculated temperature with best fit line and equation, taken from values displayed by furnace control window during heating cycles.

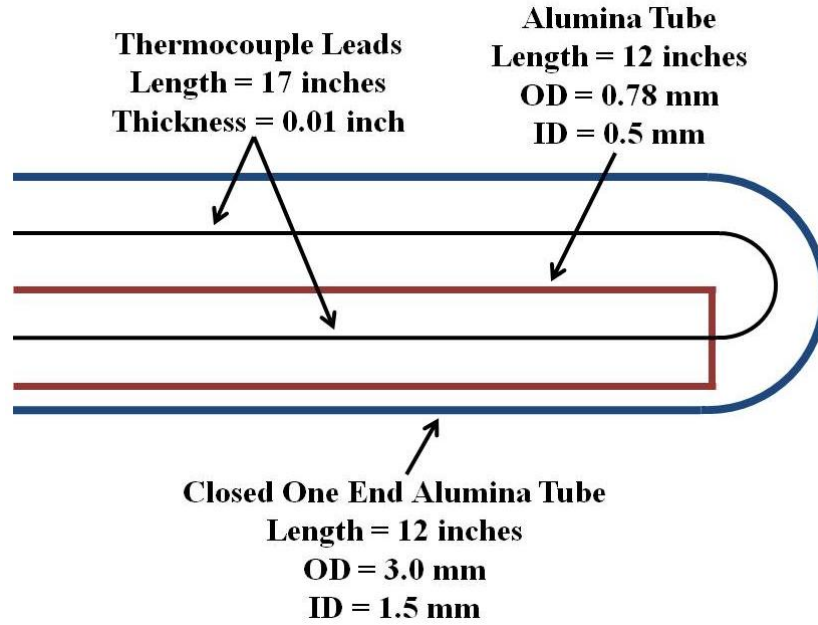


Figure 2.8: Diagram of the primary thermocouple encasing.

The safety thermocouple entering the rear of the furnace through the vacuum port is also protected by a closed one end alumina tube and the leads are separated by a double bored alumina rod and insulation taken from old wires. The safety thermocouple displays a temperature that is always below the temperature displayed by the primary thermocouple on the interior of the furnace since it is open to the air and the protection tube is further away and on the exterior of the heating element and combustion tube. An equation that relates the temperature from the safety thermocouple to the temperature of the primary thermocouple is:

$$T_{Primary}(^{\circ}C) = 1.1353 * T_{Safety}(^{\circ}C) + 287.08(^{\circ}C) \quad 2.2$$

The safety thermocouple is wired to a temperature/process controller that can shut the power off to the furnace if the temperature reaches above 1215°C, corresponding to 1666°C in the hot zone, even though the furnace is capable of temperatures above

3200°C. This cut off temperature is chosen to protect the alumina from damage if the furnace were to heat to a higher temperature than programmed because alumina begins to creep at 1650°C [1].

2.2.5 Mass Spectrometer

The mass spectrometer consists primarily of a top plate, an ionization gauge, a diffusion pump and a foreline pump. Figure 2.9 shows an image of the top plate and the positions of the gas inlet socket and detection apparatus, including the interface socket, filaments, lenses, mass filter, and electron multiplier. The ionization gauge is a device to measure the pressure inside the top plate. The diffusion pump produces the high vacuum inside the top plate and ionization gauge. The foreline pump aids the diffusion pump in removing gas back to the atmosphere [1].

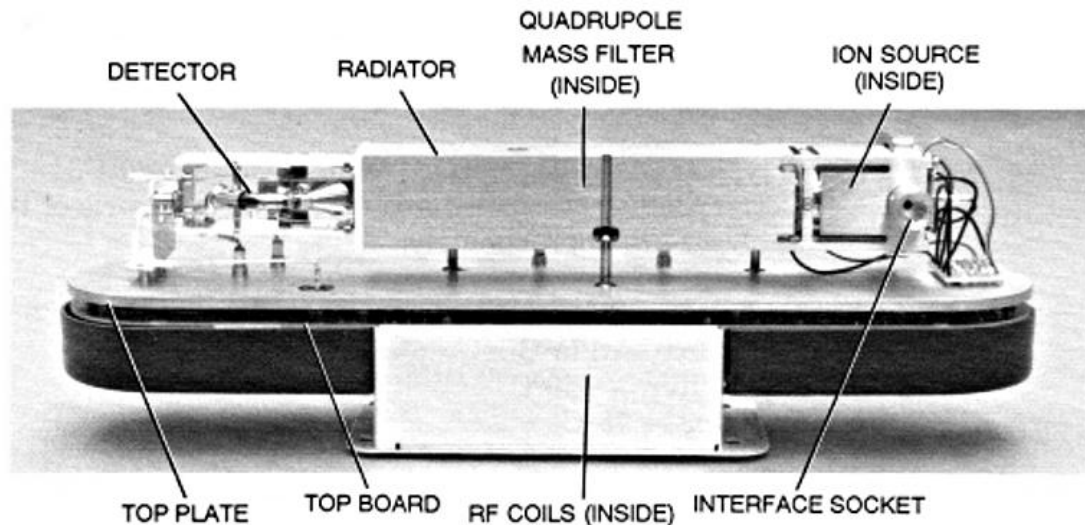


Figure 2.9: Image of the mass spectrometer top plate [1].

2.3 Improvements

Several improvements to the CDMS have been implemented in order to attain better results and expand the functionality of the system. In response to several primary thermocouples breaking during heating cycles from large amounts of carbon monoxide being evolved from the sample, the lead diameter of the thermocouple was increased from 0.010 inch to 0.015 inch. To provide even more protection to the thermocouple, an alumina protection tube with a closed end in the hot zone was installed to separate the thermocouple from any gases that are evolved from the sample. This also allows the lead diameter of the primary thermocouple to be reduced back to 0.010 inch. The mullite combustion tube was replaced with an alumina tube to increase the maximum operating temperature of the CDMS from 1500°C to 1650°C. Alumina spacers (A-16, Alcoa, New York, NY) were also fabricated to replace the calcia-stabilized zirconia (CSZ) spacers, machined from our supply of CSZ (Machined Ceramics, Inc., Bowling Green, KY), that were degrading at temperatures above 1500°C. The 0.7 mm thick, 11 mm diameter alumina spacers were fabricated by pressing powder to 3000 psi gauge pressure (approximately 160 MPa applied load), holding for 3 minutes using a 12.5 mm diameter die and sintering in air to 1630°C for 3 hours.

Changes were also made to the standard operating procedure to eliminate mass spectrometer signals that were identified to be originating from sample preparation processes. A metal scoop and polystyrene weigh boat (Disposable Polystyrene Weigh Dish, 2-202B, Thermo Fisher Scientific, Waltham, MA) was used to weigh the ceramic powder and transfer the pressed sample. During heating cycles that used this process, a family of mass spectrometer peaks was observed from several powder compositions and

was eventually traced back to the styrene in the boat. The substitution of a metal weigh scoop instead of the polystyrene boat has eliminated this family of peaks from sample signals.

It was also discovered that peaks associated with a sample were observed when there was no sample in the furnace on the subsequent heating cycle. This led to the conclusion that gases evolved from the sample were diffusing into the sample holder apparatus or combustion tube and were being evolved during the next heating cycle. Before each sample, an oxidation and inert conditioning heating cycle must be completed to remove contaminants from the system.

2.4 Procedure

To determine if a powder composition that has not been tested before in the CDMS will react with either the calcia-stabilized zirconia or the alumina spacers, a small pressed pellet (0.2 g) should be placed on scrap CSZ and alumina and heated in the box furnace up to the desired soak temperature. The boron nitride spray (Boron Nitride Aerosol Spray, SP-108, Materion Advanced Chemicals, Milwaukee, WI) can be used to coat the ends of the sample to prevent the pellet from reacting with the spacers if it is determined to react with both the CSZ and alumina. Another option would be to press and sinter new spacers out of a ceramic that won't react with the alumina sample holder and the new sample material.

In order to prepare the furnace environment for the sample heating cycle, an oxidation heating cycle must be performed using air up to 1650°C, with a high temperature hold for one hour. The spacers that will be used with the sample, along with

new alumina paper should be placed in the hot zone for this heating cycle. Mass spectrometer data is not collected during this heating cycle because the tube side gas is air, which contains a significant amount of oxygen that can damage the mass spectrometer filaments. The pressure during the evacuation of the shell side should be reduced to around 0.04 torr and a continuous purge of nitrogen and air in the shell and tube side, respectively, should be established.

The execution of an inert conditioning cycle is next to remove species that have been incorporated into the sample holder and combustion tube during the oxidation heating cycle. The furnace should be heated to 1650°C and held for one and a half hours, while using helium as the carrier gas on the tube side. An inert gas was chosen to avoid possible reactions between the sample and the carrier gas that may have occurred using gases such as nitrogen or air. Helium was chosen over other inert gases for the very low mass to charge (m/z) ratio signal produced by helium in the mass spectrometer, which is lower than most signals expected. The same spacers and alumina paper used in the oxidation heating cycle should again be present in the sample holder for this heating cycle. The pressure during the evacuation of the tube side should reach about 0.06 torr and the pressure in the shell side should again be reduced to around 0.04 torr. Continuous purges of helium and nitrogen are then established for the tube and shell side, respectively. The mass spectrometer should be acquiring data during the inert conditioning cycle to confirm the signals are consistent with other inert conditioning cycles.

The final heating cycle before the heating of the sample is a background heating cycle, which is used to determine the background mass spectrometer signals and to record

the length changes of the spacers that are then corrected for in the sample heating cycle. The background heating cycle uses helium as the carrier gas in the tube side and should have the same temperature profile as the sample heating cycle, which usually has a different maximum temperature and hold time than the inert conditioning cycle. The spacers must be held in place between the dilatometer plunger and key to record their length changes during the heating cycle. The zero point is auto-adjusted using the dilatometer software and the water circulator should be turned on. The tube and shell sides are then evacuated and continuous purges are established as described in the inert conditioning cycle above. After starting the mass spectrometer, establish a baseline by waiting about twenty minutes before turning on the furnace controller, and then start the data acquisition when the calculated temperature reaches 150°C.

To prepare a sample, uniaxially press one gram of powder to a gauge pressure of 1000 psi (approximately 200 MPa applied load), and hold for 1 minute using a 6.4 mm diameter die. Depending on the type and particle size of the powder, the pressure can be adjusted to prevent the sample from breaking during pressing. If the sample contains elements that could damage the mass spectrometer, such as sulfur, only about 0.2 grams should be used for the pellet. After measuring the mass and dimensions of the sample, the sample is loaded between the spacers in the sample holder and continuous purges on both the tube and shell side are established. Using the dilatometer software, auto-adjust the dilatometer zero point, define the sample length, and select the previous background heating cycle as the dilatometer correction file. The dilatometer settings found in Table 2.2 should be reviewed and the water circulator should be turned on. In the 'manual tune' view on the MS, the 'ms temp' should read between 165-180°C and the 'vacuum' needs to

be in the range of 6-10 mTorr, and the rest of the MS settings in Table 2.3 should be reviewed. The mass spectrometer should again collect data for about twenty minutes to establish a baseline, after which the furnace controller can be turned on and the data acquisition can start when the calculated temperature reaches 150°C. Table 2.4 shows the data analysis steps for the dilatometer that allows for the length change of the spacers to be subtracted from the sample heating cycle via the background heating cycle measurements. The correction for the spacers is on the order of tens of microns whereas the sample length change is about a millimeter.

Table 2.2: Dilatometer settings for data acquisition [1].

Setting	Value (units)	Comments
Range	2500 μm	Must match analog numbers on control board
Zero Point	85%	Allows for thermal expansion and full shrinkage
Power Output	75%	Allows for ramp rate up to 21 $^{\circ}\text{C}/\text{min}$ to 1600 $^{\circ}\text{C}$
Ramp Rate	Linear	Power output should be <40% below 1000 $^{\circ}\text{C}$
Soak	≤ 1650 $^{\circ}\text{C}$	Between sintering and melting points of material
Cooling	Same as Ramp	-- -- --
Length	~ 10 mm	Used for Piston Correction during analysis
Duration	Variable	Auto shut-off for furnace control
Max Temperature	1675 $^{\circ}\text{C}$	Auto shut-off for furnace control
Sampling Interval	20 seconds	-- -- --
Pressure Control	300 mN	Set on the control board above the thyristor

Table 2.3: Mass spectrometer settings that make up a Method [1].

Setting	Value (units)	Comments
Mode (1)	Scan	Allows quick data collection over a range of masses
Range	2-200	M/z ratios scanned during heating cycle
N value	0-7	Data for each m/z will be collected 2^N times
Mode (2)	SIM	Selected Ion Monitoring, higher precision than Scan
Group	Up to 50	Group of masses that will be monitored for a set time
Start Time	Minutes	When collection for a group begins; 1 group at a time
Masses	Up to 30	Specific masses that will be monitored for this group
Dwell	200 ms	How long data will be collected for a given m/z
Tune File	AT1211.U	Suite of settings for mass filter and ion collector

Table 2.4: Steps for dilatometer data analysis [1].

Step	Setting	Comments
Signal Correction	Zero File	Time based, specified while preparing heating cycle
Signal Correction	Piston Correction	Whole trace, Alumina
Y-Smoothing	Default	-- -- --
Export	ANSI Format	Creates a file that can be opened in Excel

2.5 References

1. M. Schurwanz, "Development of a Combined Dilatometer and Mass Spectrometer Analysis System for Studying Gas Phase Chemistry and Kinetics During Sintering," Master's Thesis submitted to the University of Missouri, December 2010.

Chapter 3

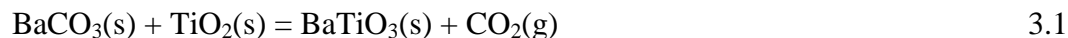
Evolved Gas Analysis of Barium Titanate, Barium Carbonate, and Barium Sulfate, with Background Chemistry of the CDMS

3.1 Introduction

Barium titanate (BaTiO_3) is a ferroelectric material that has a high permittivity and can exhibit tailored electrical properties when doped with metal oxides [1]. These properties have allowed barium titanate to be used extensively as the dielectric material in capacitors. The drive for smaller electronic components necessitates increasing volumetric efficiency through the manipulation of the properties listed above and others such as mechanical strength, and grain size and grain uniformity, which are dependent on multiple factors, such as initial powder particle size, powder purity, amount of dopant, and sintering conditions [2-4].

Evolved gas phase species were compared to the amount of shrinkage observed for barium titanate using the CDMS. The sources for these evolved species are investigated through the evaluation of heating cycles of the background furnace environment and two common production precursors of barium titanate, barium sulfate, and barium carbonate. The traditional methods of barium titanate synthesis are reviewed in depth in order to highlight the sources of possible impurities in the final powder.

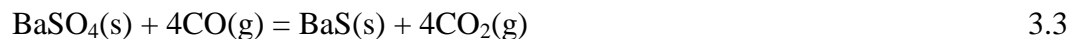
The most common method used to produce barium titanate is by the solid state reaction between barium carbonate and titanium dioxide:



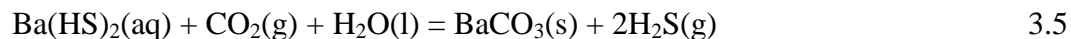
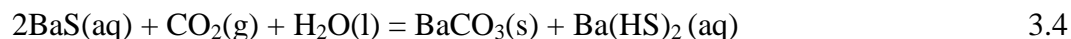
which has a byproduct of carbon dioxide evolution [5]. The production methods of barium carbonate will be discussed first, followed by those of titanium oxide.

The mineral barite (BaSO_4) is first exposed to carbon gasification to reduce the barite mineral into barium sulfide [6] via:





The barium sulfide is then either 1) precipitated with carbon dioxide or 2) precipitated with soda. The first path has two reactions that occur concurrently to produce barium carbonate [7-9]:



The second route to barium carbonate uses barium sulfide dissolved in a lye and soda solution which has sodium sulfide as a byproduct [7] via:

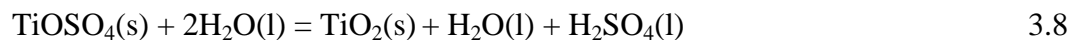


The solution is then filtered, washed, and dried to separate the barium carbonate from the sodium sulfide [10]. Depending on the method of preparation, possible impurities in the final barium carbonate powder may include sulfur, carbon, oxygen, hydrogen, and sodium and compounds thereof.

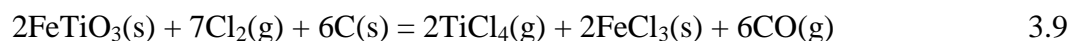
Titanium dioxide (TiO_2) is found in three mineral forms: anatase, brookite, and rutile, and can also be processed from ilmenite (FeTiO_3) using either the sulfate or chloride process. The sulfate route begins with the mineral reacting with sulfuric acid via:



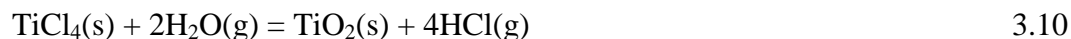
and is then magnetically separated to remove the iron-containing species [11, 12]. The titanium dioxide is then precipitated from the mixture according to:



which is then washed and calcined to form titanium dioxide [11]. The chloride process begins with the reaction of the ilmenite in reducing conditions:



The products from Equation 3.9 are then condensed and purified through distillation and crystallization of the chlorides and separation of the iron compounds. The final reactions occur simultaneously at high temperature to produce the titanium dioxide [11]:



Depending on which process is used, the final impurities in the titanium oxide powder can include oxygen, sulfur, iron, hydrogen, chlorine, carbon and compounds thereof.

In summary, the compounds and reactions used to synthesize barium titanate allow for the possibility of various impurities to be introduced into the final powder. The objective of this evolved gas analysis of the sintering of barium titanate is to provide insight into the composition of evolved species, the temperatures at which they appear, and their possible sources. The identification of impurity sources and temperatures of evolution can allow tailored sintering cycles to remove species at specific temperatures, potentially reducing the amount of time needed to hold at high temperature to completely sinter the green body and thereby lowering the cost of production. The removal of impurities at lower temperatures can also influence final properties of the finished product.

3.2 Experimental

The CDMS utilized for these experiments consists of a furnace/dilatometer that is connected to a mass spectrometer and includes both a gas and a coolant flow system. This apparatus allows for the acquisition of the length change and the evolved gas during the heating of the ceramic powders. The gas flow system utilizes gas cylinders and a mixing

station to set the gas composition and flow rate. A mullite combustion tube separates the alumina pushrod dilatometer and alumina sample holder from the heating element environment of the furnace. The combustion tube is evacuated twice to 0.06 mbar and backfilled with high purity helium (99.999%) to 1 bar, and then a gas flow rate is set at 135 mL/min. A fused silica capillary of 0.1 mm ID and 45 cm long is held near 320°C and facilitates the flow of a portion of the carrier gas to enter the mass spectrometer. The flow rate is sustained for 1-2 hours before the heating cycle begins to allow further purging of the system and to establish baseline signals in the mass spectrometer.

It has been observed in the CDMS that the evolved gas signals from samples at high temperatures are commonly present in the signals of subsequent heating cycles. The first three heating cycles in Table 3.1 are performed prior to each sample in order to obtain the most consistent data from the CDMS. The retention of species from previous heating cycles is most likely caused by the evolved species being incorporated into the spacers, pushrod, sample holder, and combustion tube, which are then evolved during the next heating cycle. The species may be retained either in the form of compounds, such as carbonates, or by diffusion into pores or grain boundaries. The removal of these species is accomplished by performing an oxidation heating cycle with air and then an inert conditioning heating cycle using helium to lower the intensity of background gases in the furnace. The high temperature hold times of these cycles are 1-3 hours, 3-9 times as long as the high temperature holds of the sample heating cycles, to allow adequate time for the reacted species to be removed. After the inert conditioning cycle but before each sample heating cycle, a background heating cycle in helium is performed without a

sample, using only spacers, in order to get the most accurate dilatometer correction file and background signals in the mass spectrometer.

Table 3.1: Heating cycles with atmosphere, heating and cooling rates, and high temperature holds and times performed with the CDMS.

Run Designation	Atmosphere	Heat & cool rate (°C/min)	High temperature hold (°C, min)
Oxidation Cycle	Air	21	1500, 120
Inert Conditioning Cycle	He	21	1500, 150
Background Cycle	He	15	1500, 20
BaSO ₄	He	14	1350, 20
BaCO ₃	He	14	1350, 20
BaTiO ₃ -14	He	14	1350, 20
BaTiO ₃ -8	He	8	1350, 20
BaTiO ₃ -20	He	20	1350, 20
BaTiO ₃ -14L	He	14	1350, 20

The BaTiO₃-8, -14, and -20 (TAM Ceramics, New York) pressed samples were prepared using powder of >99.0% purity. One gram of powder is dry pressed to 122 MPa in a 6.4 mm ID cylindrical steel die and held for 1 min; this results in a relative green density of 0.50, based on a theoretical density of 6.02 g/cm³ for barium titanate. The BaTiO₃-14L (loose powder) sample consists of 0.2 g of powder placed on a calcia stabilized zirconia (CSZ) boat and no dilatometer data was gathered. The 0.4 g BaCO₃ (Aldrich, Milwaukee, WI) of 99.98% purity sample and the 0.2 g BaSO₄ (Aldrich, Milwaukee, WI) sample of 99% purity were prepared using the same pressing method as described above. Dilatometer data was not collected for the BaCO₃ and BaSO₄ samples because they were observed to cause the spacers to become brittle at temperatures achieved during the heating cycles. The CSZ spacers, machined from our supply of CSZ by (Machined Ceramics, Inc., Bowling Green, KY), were used on either side of the

pressed BaTiO₃ samples to prevent reaction between the samples and the alumina sample holder and pushrod.

The temperature profiles for each of the heating cycles are listed in Table 3.1. The acquired dilatometer data for the pressed samples were corrected and smoothed using the data analysis software (Linseis Data Evaluation, v. 2.18, Linseis GmbH, Germany). The methods used to facilitate the identification of evolved species included comparing the signals from the mass spectrometer to cracking patterns (CP) [13] of suspected chemicals and the isotopes [14] of elements that comprise these chemicals. These elements and their natural isotopic abundances are listed in Table 3.2. Another method was to compare the signals with other samples previously run, such as CO₂ gas or samples of similar composition.

Table 3.2: Species and natural isotopic abundances for C, O, S, and Ti [14].

C	Abundance	O	Abundance	S	Abundance	Ti	Abundance
12	0.9894	16	0.9976	32	0.9499	46	0.0825
13	0.0108	17	0.0004	33	0.0075	47	0.0744
		18	0.0021	34	0.0425	48	0.7372
				36	0.0001	49	0.0541
						50	0.0518

3.3 Results

3.3.1 Inert Conditioning Heating Cycle

Figure 3.1 shows the plots of the m/z=4, 12, 16, 18, 28, 32, 44, 48, and 64 signals and temperature versus time during the inert conditioning cycle at a heating rate of 21°C/min in flowing helium. The m/z=4 signal, assigned to the helium carrier gas, experiences a slight decrease when the maximum temperature is reached at t=95 min and

subsequently gradually increases through the end of the run. The slight but steady decrease during the heating cycle of the water and nitrogen signals, typified by the $m/z=18$ and 28 signals, respectively, is evidence that water vapor and nitrogen from the small amount of air that was not evacuated from the system beforehand is being removed via the continuous purge of helium.

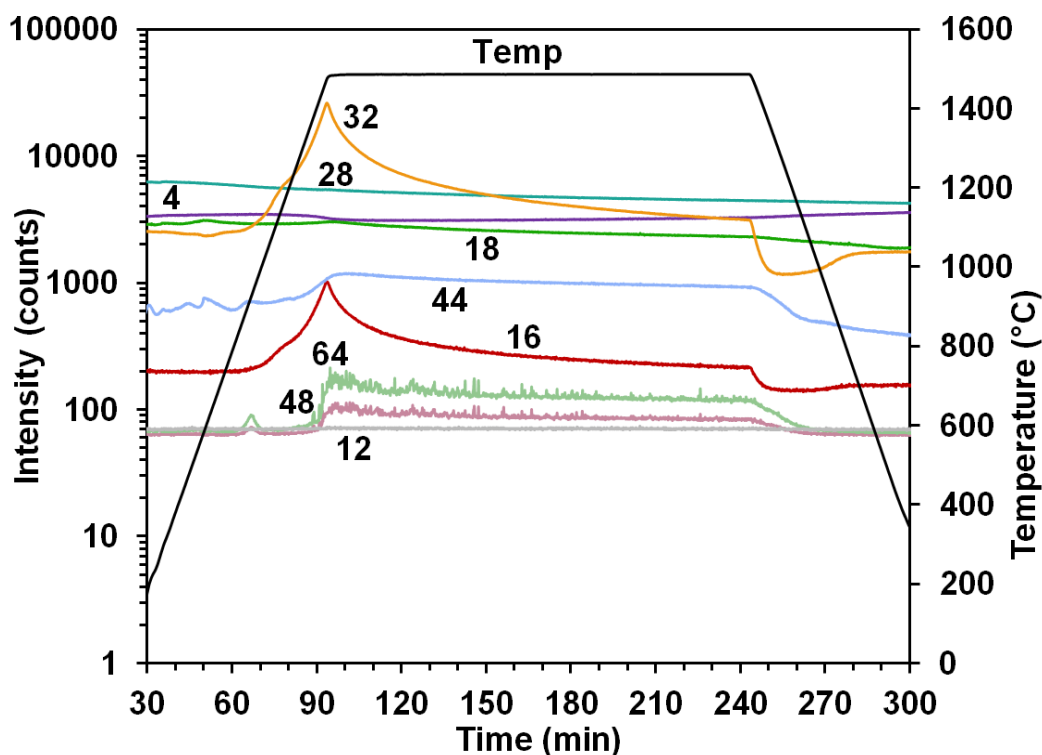


Figure 3.1: Temperature (Temp) and species intensity of the $m/z=4, 12, 16, 18, 28, 32, 44, 48,$ and 64 signals versus time for the inert conditioning cycle heated at $10^{\circ}\text{C}/\text{min}$ in flowing helium.

The $m/z=16$ and 32 signals exhibit similar features during the high temperature hold in Figure 3.1. Both signals peak at $t=95$ min when the maximum temperature is reached, decrease throughout the hold, and sharply decrease at $t=245$ min at the end of

the high temperature hold. The peak intensities of the $m/z=16$ and 32 signals were normalized and compared to the known tabulated CP values for oxygen listed in Table 3.3. The $m/z=16$ signal ratio is lower than what is expected when compared to the tabulated CP for oxygen; in spite of this discrepancy, however, the evolved gas is most likely oxygen, which was approximately 21% of the carrier gas (air) from the previous heating cycle. The majority of the composition of air is nitrogen (~78%) which is less reactive and not likely to be incorporated into the furnace environment. It is expected that the oxygen from the air during the previous cycle had been taken up by the spacers, sample holder, and combustion tube and is being evolved due to the low partial pressure of oxygen in the inert conditioning cycle.

Table 3.3: Comparison of normalized m/z ratios evolved from the inert conditioning and the background cycles and tabulated values corresponding to the cracking pattern (CP) for oxygen and sulfur dioxide [13].

Source	Temp (°C)	Peak intensity at m/z ratios normalized to $m/z=32$		Peak intensity at m/z ratios normalized to $m/z=64$	
		16	32	48	64
Inert Conditioning Cycle	1485	3.8	100	40.3	100
Background Cycle	1482	5.1	100	45.7	100
NIST CP for O ₂		21.8	100	-	-
NIST CP for SO ₂		-	-	49.2	100
Possible Compounds		¹⁶ O	¹⁶ O ₂	³² S ¹⁶ O	³² S ¹⁶ O ₂

In Figure 3.1 it is observed that the $m/z=48$ and 64 signals have low intensity peaks during heating at 67 min (930°C) and a low and nearly constant intensity feature during the high temperature hold. Table 3.3 compares the normalized ratios of the inert

conditioning cycle to tabulated values for SO₂, showing it is a plausible source for the signals [15]. The source of the SO₂ is likely from previous compounds that have evolved SO₂ gas, which has incorporated into the spacers, sample holder and combustion tube, and is then evolved during the inert conditioning cycle. The m/z=44 signal has multiple features during the ramp period of the heating cycle and a feature similar to the m/z=48 and 64 signals throughout the high temperature hold. This signal is assigned to CO₂, a gas that is commonly evolved from samples heated in the CDMS (see Table 3.4) and, similarly to the SO₂ signals, is expected to be from gas that had in previous heating cycles been retained in the spacers, sample holder, and combustion tube, and is evolved during the inert conditioning cycle.

Table 3.4: Comparison of normalized m/z ratios evolved from barium sulfate, barium carbonate, barium titanate, and carbon dioxide, and tabulated values for the isotopes of carbon dioxide [14].

Source	Peak Temp (°C)	Peak intensity at m/z ratios normalized to m/z = 44					
		12	16	28	44	45	46
BaSO ₄	660	-	5.4	-	100	2.2	-
BaSO ₄	1160	-	3.4	-	100	0.7	-
BaSO ₄	1340	-	11.4	-	100	0.9	-
BaCO ₃	1170	0.4	1.4	2.6	100	1.2	0.5
BaCO ₃	1310	0.7	2.7	4.4	100	1.2	0.5
BaTiO ₃ -14	800	0.2	1.0	6.8	100	1.3	0.5
BaTiO ₃ -8	760	0.2	1.1	3.9	100	1.3	0.5
BaTiO ₃ -20	810	0.2	1.0	3.4	100	1.3	0.4
BaTiO ₃ -14L	760	0.2	1.0	1.4	100	1.2	0.4
CO ₂ gas	1500	0.3	1.3	3.2	100	1.2	
Isotopes for CO ₂		-	-	-	100	1.1	0.4
Possible Compounds		¹² C	¹⁶ O	¹² C ¹⁶ O	¹² C ¹⁶ O ₂	¹³ C ¹⁶ O ₂	¹² C ¹⁶ O ¹⁸ O

The nearly constant intensities of the $m/z=44$, 48, and 64 signals during the constant temperature hold period may arise from two mechanisms. The first is a reaction rate that is zero order in concentration. Although such reactions are postulated [16-18], very few reactions have been assigned as zero order. An alternative interpretation is that the decomposition reaction is equilibrium limited. For example, the decomposition reactions for divalent compounds, along with the form of their equilibrium constants, are given below [7]:



$$K_p = (P_{\text{XO}} \cdot P_{\text{CO}_2}) / a_{\text{XCO}_3} \approx P_{\text{CO}_2} \quad 3.13$$



$$K_p = (P_{\text{XO}} \cdot P_{\text{SO}_2} \cdot P_{1/2\text{O}_2}) / a_{\text{XSO}_4} \approx P_{\text{SO}_2} \cdot P_{\text{O}_2}^{1/2} \quad 3.15$$



$$K_p = (P_{\text{X}_2\text{O}_3} \cdot P_{\text{CO}_2}) / a_{\text{X}_2(\text{CO}_3)_3} \approx P_{\text{CO}_2}^3 \quad 3.17$$

where P_i is the partial pressure of species i and a_i is the activity of species i . If the activities or concentrations of the solids are taken as unity or constant, then the partial pressure of the gas over the solid is constant, as is approximately seen in the data in Figure 3.1 during the hold period.

3.3.2 Background Heating Cycle

The $m/z=4$, 16, 18, 28, 32, 44, 48, and 64 signals and temperature are plotted versus time in Figure 3.2 for the background heating cycle conducted at a ramp rate of $15^\circ\text{C}/\text{min}$ in flowing helium. These signals are examined to identify species that may or may not be evolved from the furnace environment and spacers when no sample is

present. The carrier gas signal represented by the $m/z=4$ helium signal is shown to be constant throughout the entire heating cycle, indicating a constant flow rate of helium. As in the inert conditioning cycle, the $m/z=18$ and 28 signals corresponding to water and nitrogen respectively, are steadily decreasing throughout the entire run.

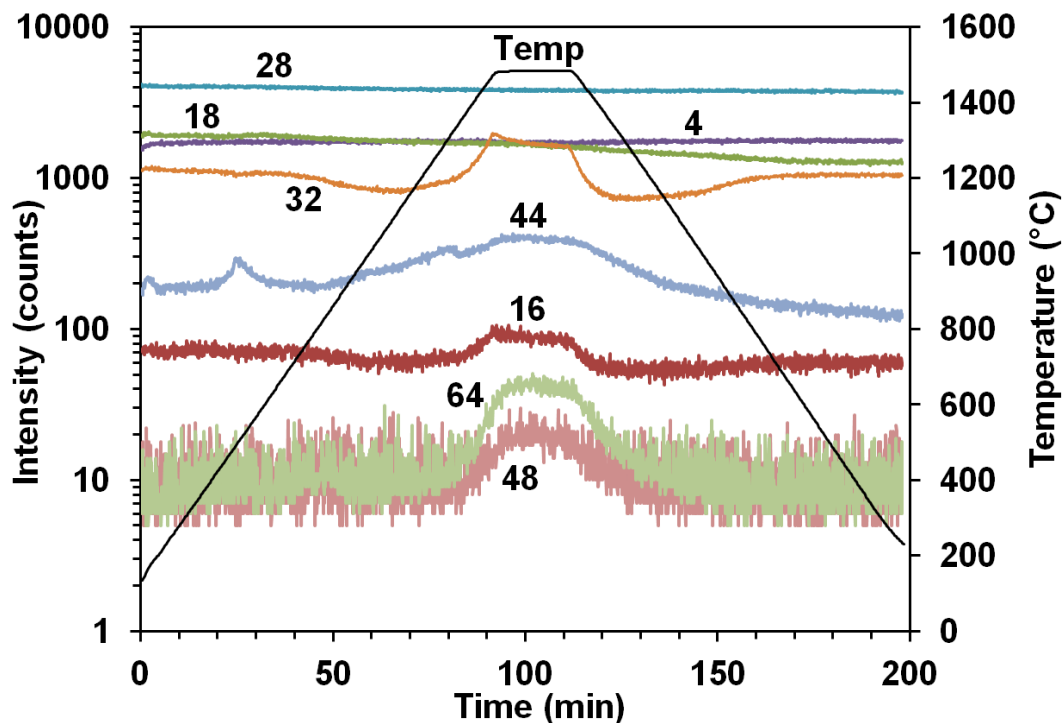


Figure 3.2: Temperature (Temp) and species intensity of the $m/z=4, 16, 18, 28, 32, 44, 48$, and 64 signals versus time for the background cycle heated at $15^{\circ}\text{C}/\text{min}$ in flowing helium.

The oxygen CP signals, O ($m/z=16$) and O_2 ($m/z=32$) exhibit similar features during the high temperature hold in Figure 3.2. The peak intensities of these signals are normalized in Table 3.3 and show agreement with the $m/z=16$ and 32 signals from the inert conditioning cycle. The similarities between the CP and shape of these signals

relative to the inert conditioning and background heating cycles support a shared source: oxygen being released that was incorporated into the spacers, sample holder, and combustion tube during the previous heating cycle. The sizeable intensity difference between the oxygen signal of the inert conditioning and background cycles is because the cycle prior to the inert conditioning cycle used an oxygen rich carrier gas and the cycle prior to the background cycle is the inert conditioning cycle, which used helium as the carrier gas.

The $m/z=44$, 48, and 64 signals in Figure 3.2 are very similar to the same signals in Figure 3.1, with low temperature features during heating and a sustained low intensity feature during the high temperature hold. These signals are assigned to the same sources as in the inert conditioning cycle, namely: CO_2 for the $m/z=44$ signal and SO_2 for the $m/z=48$ and 64 signals. In light of the relative differences in signal intensity between the inert conditioning cycle and the background heating cycle, the background intensity in the furnace environment has decreased as a consequence of performing the inert conditioning cycle following the oxidation cycle.

3.3.3 Barium Sulfate

Figure 3.3 shows the intensities of the $m/z=12$, 16, 28, 44, 45, and 46 signals and temperature versus time for the BaSO_4 sample heated at $14^\circ\text{C}/\text{min}$ in helium. The pressed sample expanded and became very porous due to decomposition during the heating cycle. The $m/z=16$, 44, and 45 signals, along with the $m/z=17$ and 18 signals not shown here, peak at 63 min (660°C) and are indicative of CO_2 ($m/z=44$) and H_2O ($m/z=18$) evolution. The same signals from the CP of CO_2 also peak at 100 min (1160°C) and during the high

temperature hold that begins at 115 min (1340°C). The $m/z=12$, 28, and 46 signals are also present in the CP of CO_2 , but do not exhibit peaks in Figure 3.3. A comparison of the $m/z=16$, 44, and 45 signals to the CP of CO_2 gas and the isotopes of CO_2 in Table 3.4, however, do not show good agreement. A tentative assignment to CO_2 is made for the peaks observed for the signals in Figure 3.3 and the larger $m/z=16$ signal compared to the CO_2 gas is explained below.

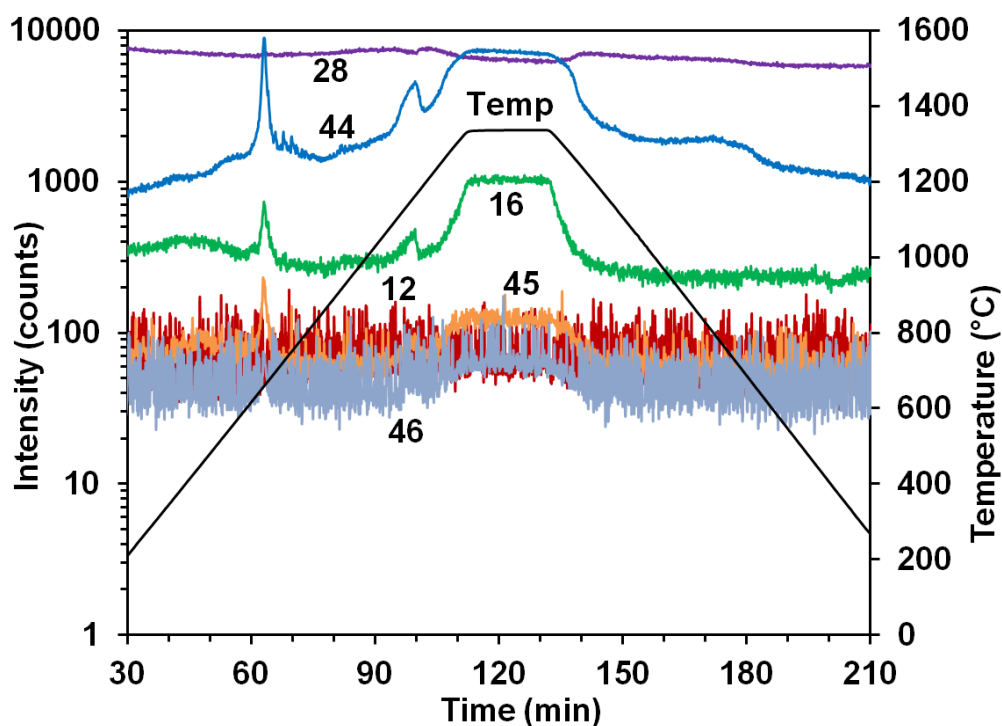


Figure 3.3: Temperature (Temp) and species intensity of the $m/z=12$, 16, 28, 44, 45, and 46 signals versus time for 0.2 g of BaSO_4 heated at $14^\circ\text{C}/\text{min}$ in flowing helium.

The $m/z=16$, 32, 34, 48, 49, 50, 64, 65, and 66 signals are plotted versus time for the BaSO_4 sample in Figure 3.4. These signals all share peaks at 83 min (930°C), 100 min (1160°C), and throughout the high temperature hold beginning at 115 min (1340°C).

The two largest signals, the $m/z=48$ and 64 signals, are potentially from the decomposition product SO_2 ($m/z=64$) and one of its cracked species SO ($m/z=48$). Table 3.5 compares the normalized signal ratios from Figure 3.4 to tabulated values for the CP of SO_2 [13] and to SO_2 isotopes. Overall, there is good agreement for all of the signals, except for the $m/z=16$ and 32 signals.

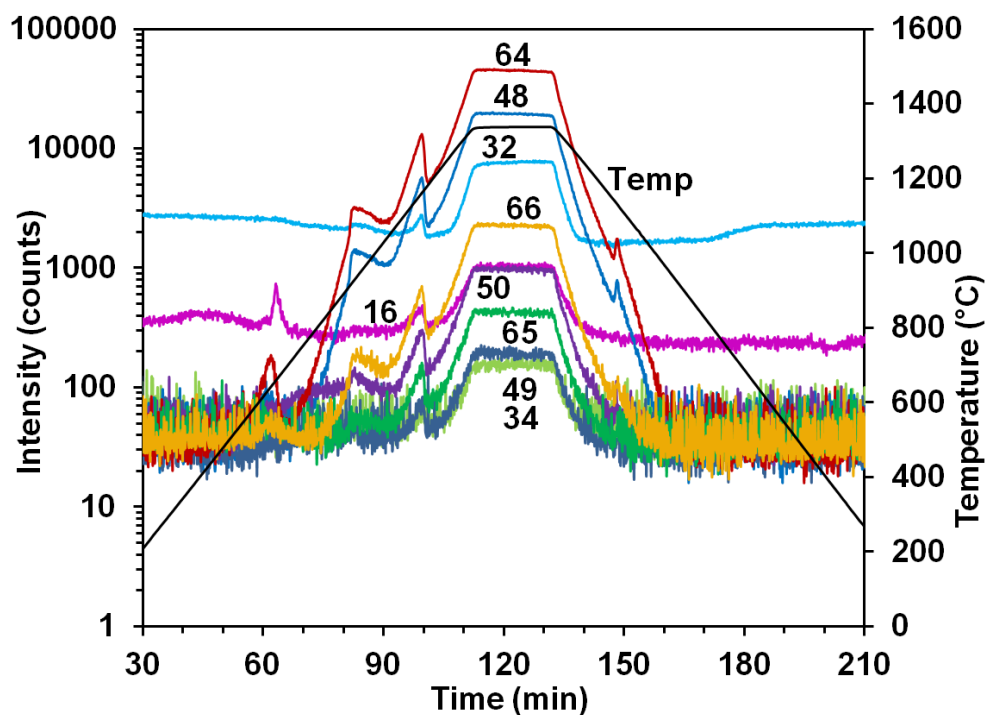


Figure 3.4: Temperature (Temp) and species intensity of the $m/z=16$, 32 , 34 , 48 , 49 , 50 , 64 , 65 , and 66 signals versus time for 0.2 g of BaSO_4 heated at $14^\circ\text{C}/\text{min}$ in flowing helium.

Table 3.5: Comparison of normalized m/z ratios evolved from barium sulfate and barium titanate, tabulated values for the isotopes of sulfur [14], and tabulated values corresponding to the cracking pattern (CP) for sulfur dioxide [13].

Source	Peak	Peak intensity at m/z ratios normalized to m/z = 64								
	Temp (°C)	16	32	34	48	49	50	64	65	66
BaSO ₄	930	1.2	17.4	0.5	43.1	0.2	2.7	100	0.6	4.5
BaSO ₄	1160	1.7	8.1	0.1	43.4	0.3	1.9	100	0.8	5.0
BaSO ₄	1340	1.8	12.2	0.3	43.5	0.3	2.1	100	0.9	5.1
BaTiO ₃ -14	900	1.9	5.5	0.2	38.4	0.3	2.0	100	1.0	5.0
BaTiO ₃ -14	1000	1.9	9.3	0.2	38.0	0.4	1.9	100	0.9	5.0
BaTiO ₃ -8	990	2.1	3.9	0.2	39.2	0.4	1.9	100	0.9	4.9
BaTiO ₃ -20	930	1.9	4.7	0.1	39.3	0.4	1.9	100	0.9	5.0
BaTiO ₃ -20	990	1.9	5.6	0.1	39.4	0.4	2.0	100	1.0	5.0
BaTiO ₃ -14L	975	0.9	9.6	0.3	39.4	0.5	2.0	100	1.1	5.2
SO ₂ Isotopes		-	-	-	-	-	-	100	0.9	4.9
NIST CP for SO ₂		5.9	10.4	0.4	49.2	0.4	2.2	100	0.9	4.9
Possible Compounds		¹⁶ O	¹⁶ O ₂ ³² S	³⁴ S	⁴⁸ Ti ³² S ¹⁶ O	⁴⁹ Ti ³³ S ¹⁶ O	⁵⁰ Ti ³⁴ S ¹⁶ O	⁴⁸ Ti ¹⁶ O ³² S ¹⁶ O ₂	⁴⁹ Ti ¹⁶ O ³³ S ¹⁶ O ₂	⁵⁰ Ti ¹⁶ O ³⁴ S ¹⁶ O ₂

Possible sources of SO₂ include the decomposition of a sulfate as in Equation 3.14 or from the oxidation of trace sulfur or sulfur containing species via:



The discrepancy in the CPs of the m/z=16 and 32 signals in Table 3.5 can thus be accounted for by the additional release of oxygen gas, as shown in Equation 3.14. The actual weight loss experienced by the BaSO₄ sample was only about 7.7% of the stoichiometric weight loss that accompanies full decomposition. A more complete decomposition would have occurred if the maximum temperature were raised to 1500°C.

A salient feature of all of the m/z signals that appear during the hold period is that they have nearly constant intensity for the entire duration of the hold. This again may be

indicative of equilibrium-limited reactions for sulfate and carbonate decomposition, as given by Equations 3.12-17.

3.3.4 Barium Carbonate

The $m/z=12$, 16, 28, 44, 45, and 46 signals and temperature versus time are plotted in Figure 3.5 for the pressed BaCO_3 sample heated at $14^\circ\text{C}/\text{min}$ in helium. These signals all begin to appear at 80 min (760°C) and share similar high temperature features with the first peak occurring for the $m/z=44$, 45, and 46 signals at 110 min (1170°C) and for the $m/z=12$, 16, and 28 signals a short time later. The next feature is a high temperature shoulder immediately before the temperature hold at 120 min (1310°C) for all of the signals in Figure 3.5. The major peak of this family, the $m/z=44$ signal, is suggestive of CO_2 evolution and the intensity of the two peaks at 110 min (1170°C) and 120 min (1310°C) are used to normalize the other signals, as seen in Table 3.4. The normalized ratios for the peaks at 110 min (1170°C) show very good agreement to both the CP of CO_2 gas and to the isotopes for CO_2 . The signals at 120 min (1310°C) also agree very well with the isotopes for CO_2 ; however, the $m/z=12$, 16, and 28 signals are significantly larger than the CP of CO_2 gas and approximately twice as large as compared to the peak signals at 110 min (1170°C).

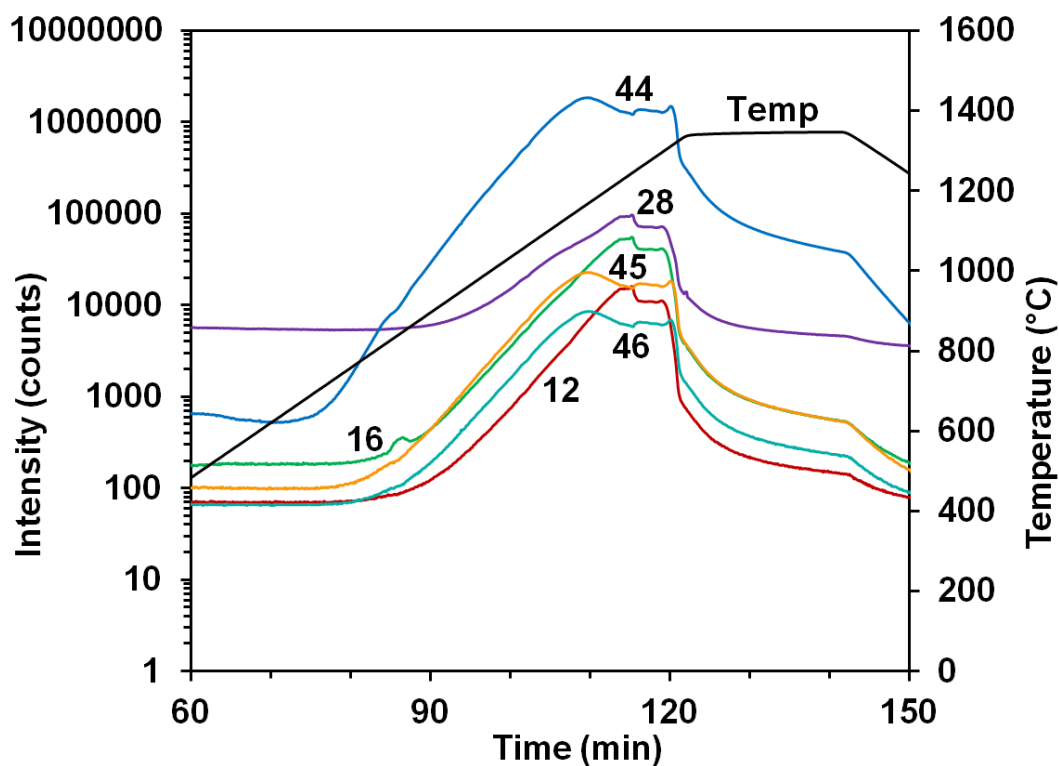


Figure 3.5: Temperature (Temp) and species intensity of the $m/z=12$, 16, 28, 44, 45, and 46 signals versus time for 0.4 g of BaCO_3 heated at $14^\circ\text{C}/\text{min}$ in flowing helium.

The source for the CO_2 from the BaCO_3 sample is well documented to be from the decomposition of the powder into BaO and CO_2 [7]. The increase in normalized amounts of the $m/z=12$, 16, and 28 signals at 120 min (1310°C) is possibly from an increased relative amount of CO compared to CO_2 . From the equilibrium reactions of carbon and oxygen:



Equation 3.20 has been shown to be dominant over Equation 3.19 at elevated temperatures ($T > 500^\circ\text{C}$), resulting in an increased relative CO signal to CO_2 in the presence of excess carbon [19-21]. The source for the excess carbon must come from

impurities inherently in the powder or were picked up during the pressing of the pellet because previous tests have shown that the CO/CO₂ ratio of pure CO₂ gas at elevated temperatures in the CDMS does not change.

Barium carbonate begins to decompose at temperatures above 900°C and the rate of decomposition increases with temperature to the melting point at 1360°C [7]. Based on the expected stoichiometric weight loss due to full decomposition of the BaCO₃ sample, about 30% more mass was lost, which is attributed to powder broken off the sample during handling after the heating cycle.

Figure 3.6 shows the m/z=34, 48, 49, 50, 64, 65, and 66 signals and temperature versus time for the BaCO₃ sample. High temperature features between 100-122 min (1035-1330°C) occur for many of these signals at very low intensity. The only larger intensity signals that occur over the same time period occur in Figure 3.5 and have previously been assigned to CO₂. The absence of any other large intensity peaks that occur along with the signals shown in Figure 3.6 does not allow an assignment for the majority of these signals. The exception is the m/z=64 signal that is elevated during the high temperature hold, similar to what is observed for the background heating cycle in Figure 3.2, which has been assigned to SO₂.

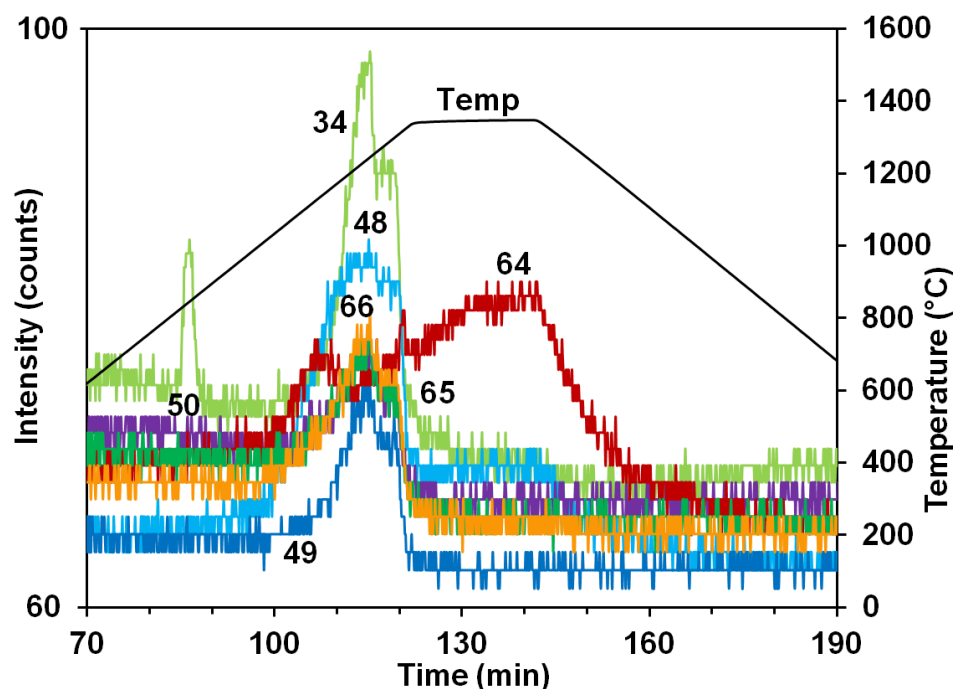


Figure 3.6: Temperature (Temp) and species intensity of the $m/z=34, 48, 49, 50, 64, 65$, and 66 signals versus time for 0.4 g of BaCO_3 heated at $14^\circ\text{C}/\text{min}$ in flowing helium.

3.3.5 Barium Titanate Heated at $14^\circ\text{C}/\text{min}$

The four largest intensity signals for BaTiO_3 -14, the $m/z=28, 44, 48$, and 64 signals, along with the sample length and temperature, versus time are shown in Figure 3.7. The pressed sample was heated at $14^\circ\text{C}/\text{min}$ and the results for density, shrinkage, and sintering temperature can be found in Table 3.6. Figure 3.7 also shows that the evolution of species into the gas phase can be divided into three primary regions. The onset temperature of the three regions along with the peak temperature for the $m/z=44$ and 64 signals are listed in Table 3.6. In region I, the $m/z=28$ and 44 signals are observed to peak at 90 min , preceded by a low temperature shoulder which may consist of several additional features that overlap. Region II shows two peaks each of the $m/z=48$ and 64 signals at 96 and 104 min . The $m/z=28, 44, 48$, and 64 signals are evolved at lower

concentrations in region III which extends into the high temperature hold period at 1345°C. Taken together, these signals indicate that species are evolved into the gas phase during a majority of the heating ramp and high temperature hold period of the sintering cycle.

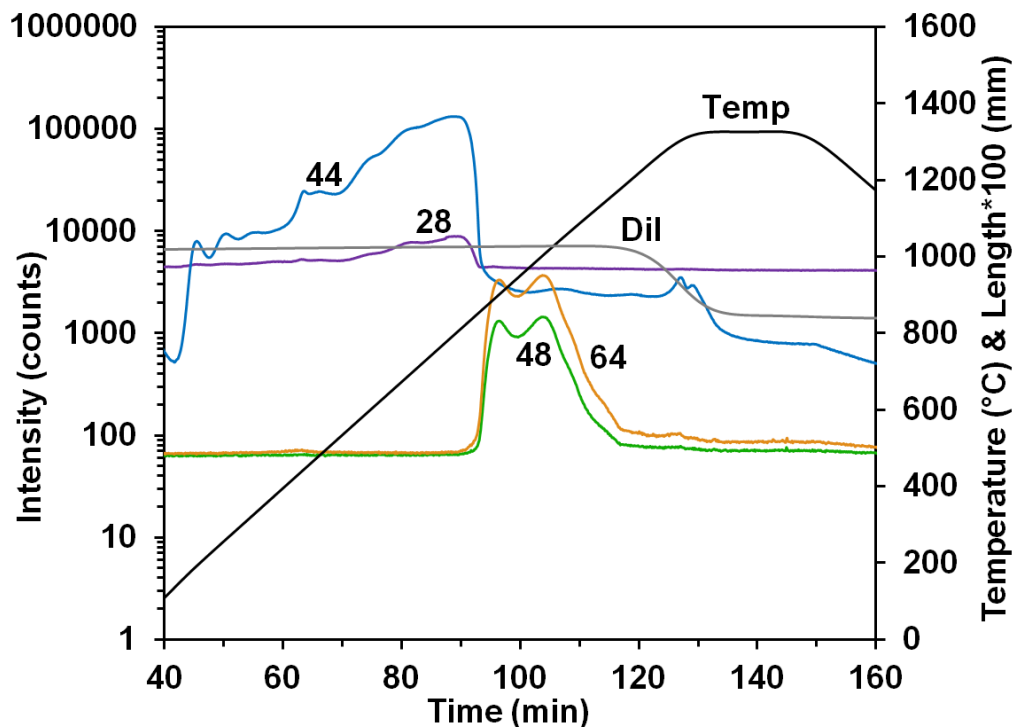


Figure 3.7: Temperature (Temp), length change (Dil), and species intensity of the $m/z=28$, 44, 48, and 64 signals versus time for 1.0 g of BaTiO_3 -14 heated at $14^\circ\text{C}/\text{min}$ in flowing helium.

Table 3.6: Comparison of relative density, linear shrinkage, sintering temperature, regions of similar signals starting temperatures, and peaks of the m/z=44 and 64 signals between barium titanate samples at different heating and cooling rates and between pressed and loose powder.

Sample with heating and cooling rate designation	Relative density (pressed, sintered)	Linear shrinkage (%)	Sintering temperature (°C)	Region I, II, and III start temperatures (°C)	Peak temperatures of the m/z=44 and 64 signals (44; 64 in °C)
BaTiO ₃ -8	0.51, 0.95	19.2	1155	170, 835, 1155	760; 990
BaTiO ₃ -14	0.50, 0.92	18.7	1150	125, 800, 1150	800; 900 & 1000
BaTiO ₃ -20	0.50, 0.92	18.4	1160	240, 860, 1160	810; 930 & 990
BaTiO ₃ -14L	-	-	-	265, 810, 1115	760; 975

The intensities of additional signals are shown in Figures 3.8 and 3.9 to assist in the identification of the species being evolved in the three different temperature regions. For the time period of 40-90 min (125-800°C) of region I, Figure 3.8 shows that the m/z=12, 16, 28, 44, 45, and 46 signals are evolved with similar shapes that include the multiple low temperature features and a single peak at 89 min (800°C). Carbon dioxide is a likely candidate as indicated by the dominant m/z=44 signal. The CO₂ assignment is supported by the agreement of the normalized ratios of the measured ion intensities arising from the BaTiO₃-14 sample as compared to measured CPs and to the isotopes of CO₂ gas of ¹²C¹⁶O₂ (m/z=44), ¹³C¹⁶O₂ (m/z=45), and ¹²C¹⁶O¹⁸O (m/z=46) in Table 3.4. The measured ratios of all of the m/z=12, 16, 28, 45, and 46 signals arising from the sample show good agreement as compared to the CP data for CO₂ measured with the mass spectrometer for pure CO₂ gas and to the isotopes of CO₂.

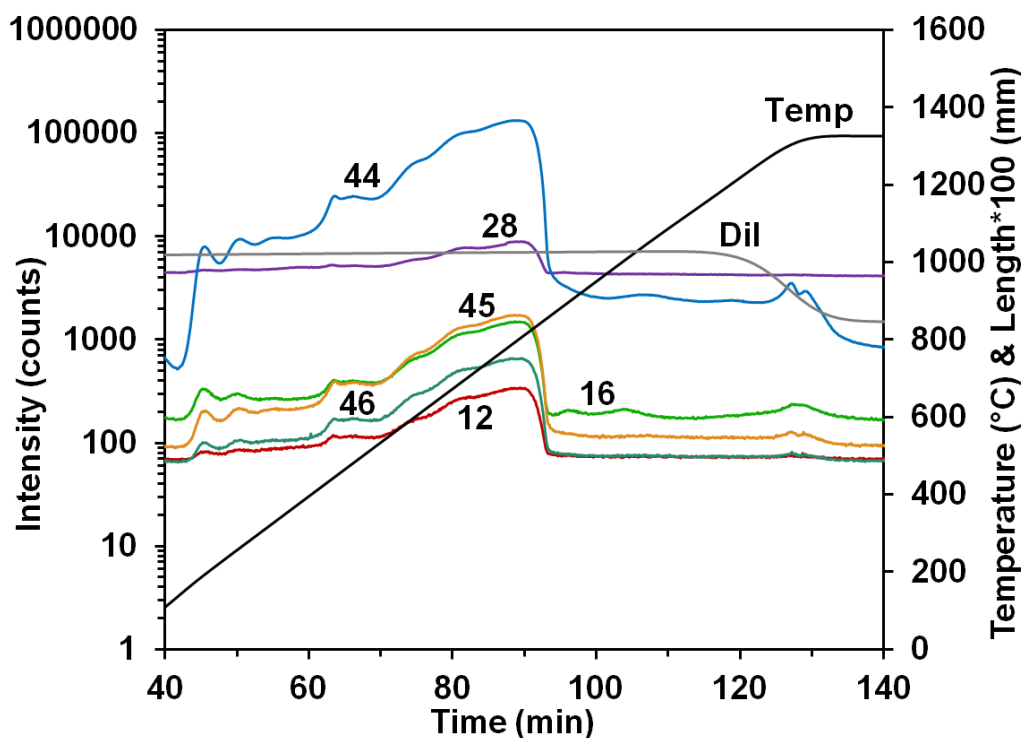


Figure 3.8: Temperature (Temp), length change (Dil), and species intensity of the $m/z=12, 16, 28, 44, 45,$ and 46 signals versus time for 1.0 g of $\text{BaTiO}_3\text{-14}$ heated at $14^\circ\text{C}/\text{min}$ in flowing helium.

The source of CO_2 at low temperature, namely below 500°C , may be from trace organic impurities arising from processing, exposure to ambient organic material, or adsorption of carbon dioxide [22]. In Cabrera *et al.* [22], the amount of BaTiO_3 surface area covered by CO_2 on varying diameter particle sizes were measured based on desorption of the gas up to about 250°C , which can then be used to estimate the moles of CO_2 originally present on the surface. This information can then be used to calibrate the mass spectrometer signal and apply it to the data from the pressed sample, resulting in approximately 20% of the amount of CO_2 released below 250°C attributed to the adsorption of CO_2 on the surface of the powder. Though the samples from the referenced

study above were only heated to 250°C, the signal representing CO₂ desorption at 250°C was well above the baseline signal that occurred near room temperature, indicating the continuing evolution of surface CO₂ at increased temperatures.

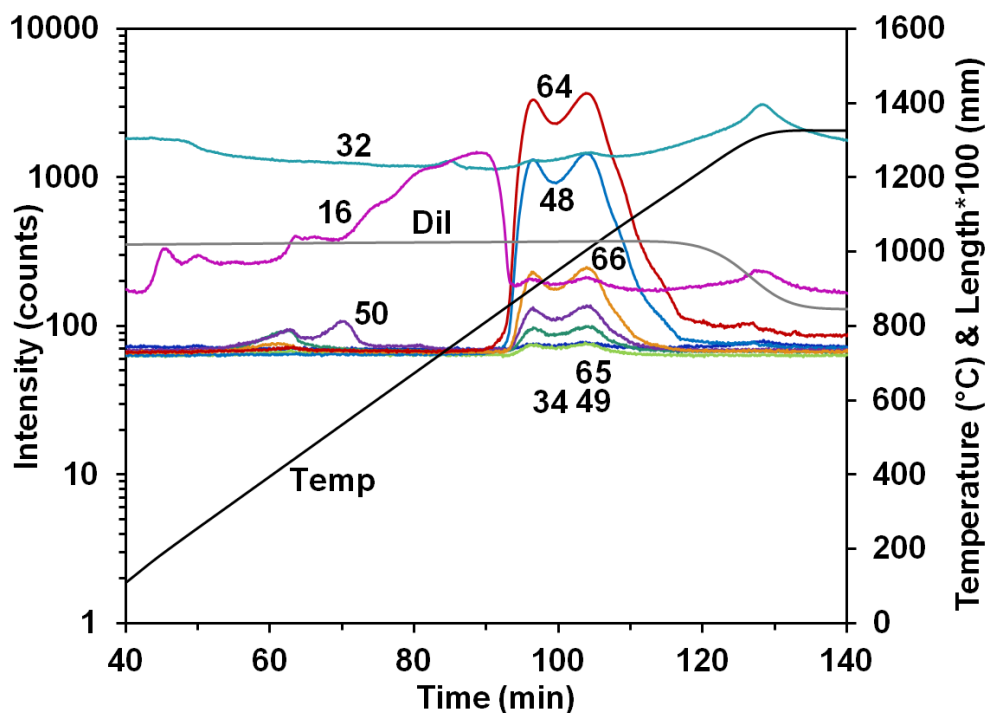


Figure 3.9: Temperature (Temp), length change (Dil), and species intensity of the $m/z=16, 32, 34, 48, 49, 50, 64, 65,$ and 66 signals versus time for 1.0 g of BaTiO₃-14 heated at 14°C/min in flowing helium.

At higher temperature, the source of the CO₂ may be from residual unreacted or surface BaCO₃ (see Equation 3.1), which is a common precursor used to produce BaTiO₃. Studies on multiple commercial BaTiO₃ powders have shown that carbon in the form of BaCO₃ is removed by surface treatments of calcination at 500°C followed by leaching in pure water or acetate buffer solution [23]. Figure 3.5 showed large intensities for the

$m/z=12, 16, 28, 44, 45,$ and 46 signals arising from the BaCO_3 sample over the temperature range of $960\text{-}1310^\circ\text{C}$, which is at higher temperatures than the CO_2 evolution observed in region I seen in Figure 3.7. A plausible explanation for the evolution of CO_2 at lower temperatures in the BaTiO_3 than in the BaCO_3 is that the BaCO_3 is not in bulk crystalline form in the BaTiO_3 powder, but is possibly present as a surface carbonate, which decomposes more easily.

For the second period (region II) of gas evolution from $90\text{-}115$ min ($800\text{-}1150^\circ\text{C}$), Figure 3.9 shows a family of similarly shaped peaks for the $m/z=16, 32, 48,$ and 64 signals that occurs prior to the onset of sintering at 115 min. Based on these four signal ratios, one possible source is TiO ($m/z=64$), with cracked species Ti ($m/z=48$), O_2 ($m/z=32$), and O ($m/z=16$). The defect chemistry reaction corresponding to these species in the gas phase is:



where the Ti ($m/z=48$) and O ($m/z=16$) signals arise from the cracking of TiO during ionization in the mass spectrometer [15]. The source for TiO in Equation 3.21 could be trace unreacted TiO_2 impurities from the synthesis scheme for BaTiO_3 , as seen in Equation 3.1. Another source could be the vaporization of TiO , although this is not expected since the powder was likely synthesized in an oxygen-rich environment. The detection of TiO would also be surprising given its low vapor pressure and the relatively low temperature of 320°C for the capillary between the dilatometer and mass spectrometer.

Another possible reaction is the evolution of SO_2 ($m/z=64$), and its corresponding cracked species of $^{32}\text{S}^{16}\text{O}$ ($m/z=48$), ^{32}S ($m/z=32$), and ^{16}O ($m/z=16$) according to either

the oxidation of trace sulfur or sulfur containing species as in Equation 3.18 or from the decomposition of a sulfate as in Equation 3.14. Impurity testing on commercial BaTiO_3 powders has shown sulfur to be a common impurity, seen at about 0.5 wt% on average between five commercial powders [23]. A sulfur source can arise via the standard synthesis route of BaTiO_3 that comes from BaCO_3 , which is derived from mined barite (BaSO_4) as seen in Equations 3.2-3.6.

The different natural isotopic abundances of S and Ti in Table 3.2 can be useful in distinguishing between TiO and SO_2 evolution. Figure 3.9 shows many of the signals corresponding to the isotope combinations of the species appearing in Table 3.2. These signals follow the trends seen for the $m/z=64$, 48, 32, and 16 signals in the same figure for the time period of 90-115 min. Consequently, the presence, absence, and amounts of these signals are used to distinguish between TiO and SO_2 .

Table 3.7 shows the peak intensity ratios, normalized to the parent compounds, of the $m/z=48$ and 64 signals for the case where TiO is suspected to be evolved from the BaTiO_3 -14 sample. With the exception of the $m/z=50$ and 66 signals, there is very little agreement between the observed intensity ratios and the expected ratios based on the isotopic abundances for TiO . There are also no peaks observed for the $m/z=46$, 47, 62, and 63 signals that are expected based on the isotopic abundances of Ti.

Table 3.7: Comparison of normalized isotope ratios that would be expected for TiO and observed data evolved at 900°C during the heating of barium titanate [14].

Source	Peak intensity at m/z ratios normalized to m/z=48					Peak intensity at m/z ratios normalized to m/z=64				
	46	47	48	49	50	62	63	64	65	66
BaTiO ₃ -14	0.0	0.0	100	1.2	5.1	0.0	0.0	100	1.0	5.0
TiO Isotopes	11.2	10.1	100	7.3	7.5	11.2	10.1	100	7.4	7.2
Possible Compounds	⁴⁶ Ti	⁴⁷ Ti	⁴⁸ Ti ³² S ¹⁶ O	⁴⁹ Ti ³³ S ¹⁶ O	⁵⁰ Ti ³⁴ S ¹⁶ O	⁴⁶ Ti ¹⁶ O	⁴⁷ Ti ¹⁶ O	⁴⁸ Ti ¹⁶ O ³² S ¹⁶ O ₂	⁴⁹ Ti ¹⁶ O ³³ S ¹⁶ O ₂	⁵⁰ Ti ¹⁶ O ³⁴ S ¹⁶ O ₂

Table 3.5 shows the observed peak intensity ratios where SO₂ is suspected to be evolved, normalized to the m/z=64 signal. The intensities of the m/z=65 and 66 signals for the BaTiO₃-14 sample are near identical to the expected isotopes for sulfur at both 900°C and 1000°C. There is also good agreement between the measured cracking patterns for the BaTiO₃-14 and the BaSO₄ samples, and the tabulated cracking pattern [13] for SO₂, with exception of the m/z=16 and 32 signals, which can be accounted for by the additional release of oxygen gas as shown in Equation 3.14. As seen in Figure 3.4, BaSO₄ decomposes between 100-130 min (1160°C through the soak period at 1350°C), which is at a higher temperature than what was observed for the corresponding signals in Figure 3.9. In a similar explanation as to why the CO₂ evolved at a lower temperature in the BaTiO₃ sample, the SO₂ source evolved at a lower temperature because it could be on the surface as BaSO₄ [23] and not in bulk crystalline form as in the BaSO₄ sample, and is therefore easier to decompose. In summary, there is very good agreement between the intensities and CPs arising from the BaTiO₃-14 and BaSO₄ samples, suggesting that the decomposition of a sulfate compound is the common source of the family of peaks seen in Figure 3.9.

Figure 3.7 also shows that a majority of the impurities from CO₂ and SO₂ are evolved before evidence of sintering is observed in region III at 115 min (1150°C). There are several smaller features of the m/z=28, 44, 48, and 64 signals during the length change of the sample, corresponding to CO₂ and SO₂ evolution that is evolved during sintering. These gases that are evolved during sintering are a very small portion of the overall amount evolved over all three regions.

3.3.6 Barium Titanate Heated at 8°C/min

The m/z=28, 44, 48, and 64 signals, temperature, and sample length versus time are plotted in Figure 3.10 for BaTiO₃-8 heated at 8°C/min in flowing helium. Table 3.6 shows the relative density, linear shrinkage, and sintering temperature for the pressed sample. As in the BaTiO₃-14 sample, the major evolved gas signals for this sample can be divided into three temperature regions, which are listed along with the m/z=44 and 64 peak temperatures in Table 3.6. The low temperature features and peaks of the m/z=28 and 44 signals occur in region I and region II is defined by the m/z=48 and 64 signal features. Region III extends into the high temperature hold and contains small amounts of the m/z=28, 44, 48, and 64 signals.

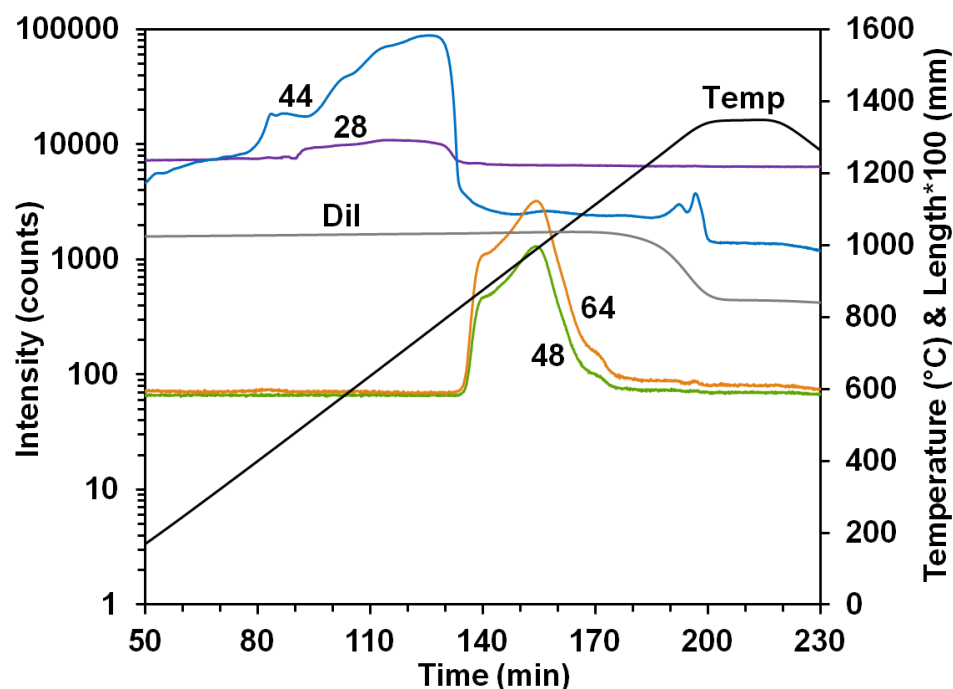


Figure 3.10: Temperature (Temp), length change (Dil), and species intensity of the $m/z=28$, 44, 48, and 64 signals versus time for 1.0 g of $\text{BaTiO}_3\text{-8}$ heated at $8^\circ\text{C}/\text{min}$ in flowing helium.

Region I of the $\text{BaTiO}_3\text{-8}$ sample also contains $m/z=12$, 16, 45, and 46 signals (not shown) with corresponding features to the $m/z=28$ and 44 signals seen in Figure 3.10. The peaks for these signals occur at 126 min (760°C) and the normalized intensity ratios are compared in Table 3.4. From this comparison, it is observed that all of the mass ratios are similar to what was observed for the $\text{BaTiO}_3\text{-14}$ sample at 800°C , except that the $m/z=28$ signal ratio is about half of what was observed for the $\text{BaTiO}_3\text{-14}$ sample. The comparison of peaks in Table 3.4 allows for the assignment of CO_2 to the signals seen in region I. The increase in heating rate from 8 to $14^\circ\text{C}/\text{min}$ caused the $m/z=44$ signal peak temperature to shift 40°C , seen in Figure 3.11, which is to be expected since activated kinetic processes shift to higher temperature when the heating rate is increased.

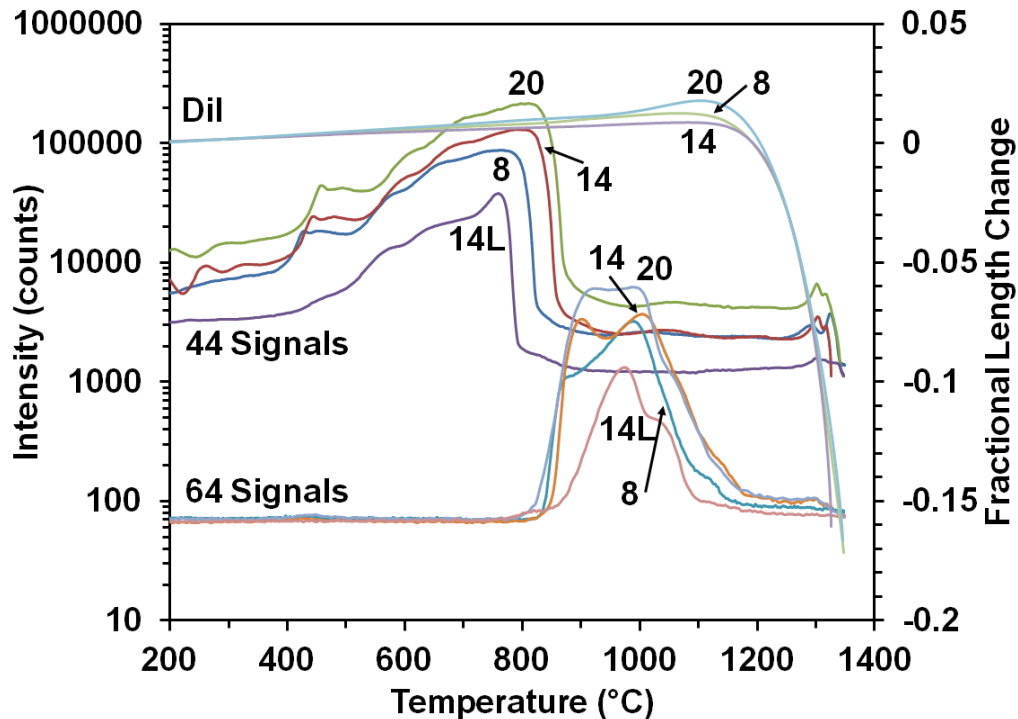


Figure 3.11: Species intensity of the $m/z=44$ and 64 signals for $\text{BaTiO}_3\text{-8}$, $\text{BaTiO}_3\text{-14}$, $\text{BaTiO}_3\text{-20}$, and $\text{BaTiO}_3\text{-14L}$ samples and length change (Dil) for $\text{BaTiO}_3\text{-8}$, $\text{BaTiO}_3\text{-14}$, and $\text{BaTiO}_3\text{-20}$ samples versus temperature in flowing helium.

The features for the $m/z=48$ and 64 signals in region II observed in Figure 3.10 are coupled with similar features for the $m/z=16$, 32, 34, 49, 50, 65, and 66 signals (not shown). There is a low temperature shoulder and peak at 155 min (990°C) for these signals, and a comparison of the normalized peak intensities in Table 3.5. The comparison shows good agreement with the $\text{BaTiO}_3\text{-14}$ sample at a similar temperature which allows SO_2 to be assigned to these signals. Similar to the CO_2 signals mentioned above and seen in Figure 3.11, increasing the heating rate increased the main peak temperature of SO_2 by 10°C , when the second $m/z=64$ signal peak for the $14^\circ\text{C}/\text{min}$

sample is compared to the 8°C/min signal peak. The increased signal at the start of the m/z=64 signal from a shoulder feature to a distinguishable peak when increasing the heating rate is worth noting. This may be related to the decrease in the time gap between the end of the m/z=44 signal and the beginning of the 64 signals when increasing the heating rate, as seen in Figure 3.11.

Region III of Figure 3.10 shows smaller features corresponding to CO₂ and SO₂ evolved during sintering in a similar way Figure 3.7 showed evolution during the length change for the BaTiO₃-14 sample. The amount evolved during region III is very small compared to what was evolved in regions I and II.

3.3.7 Barium Titanate Heated at 20°C/min

Figure 3.12 shows the m/z=28, 44, 48, and 64 signals, temperature and sample length plotted versus time for BaTiO₃-20 heated at 20°C/min in flowing helium. The relative density, linear shrinkage, and sintering temperature of the pressed sample are listed in Table 3.6. As in the other two barium titanate samples, the major evolved gas signals in Figure 3.12 are divided into three regions and are listed along with the m/z=44 and 64 signal peaks in Table 3.6. Region I contains the low temperature features and peaks of the m/z=28 and 44 signals and the two peaks of the m/z=48 and 64 signals are included in region II. Region III contains low intensity features of the m/z=28, 44, 48, and 64 signals.

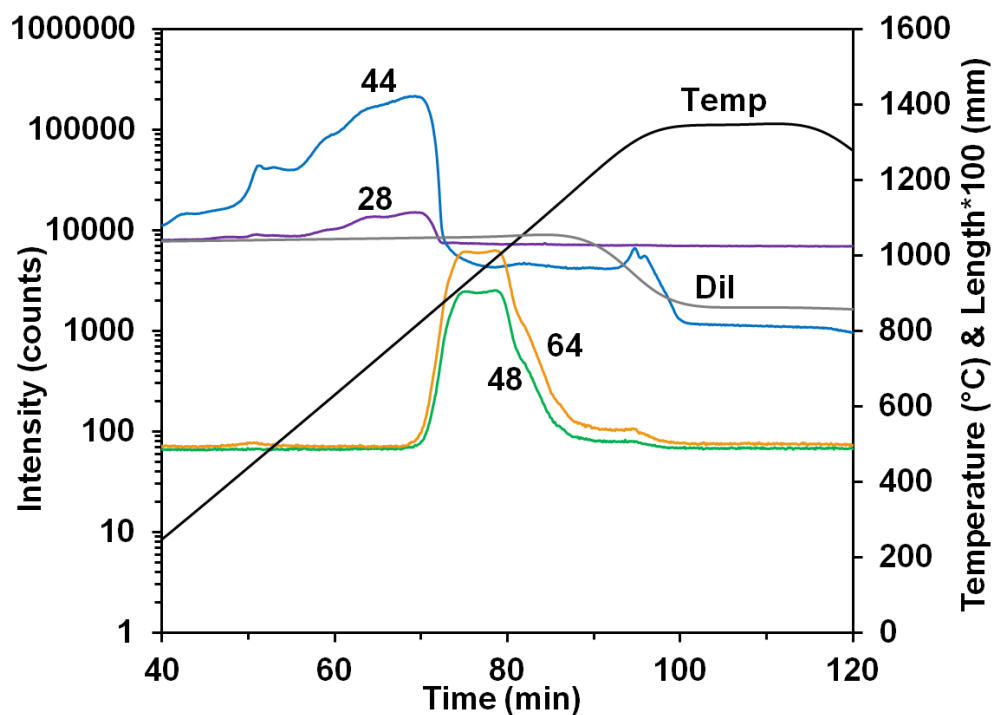


Figure 3.12: Temperature (Temp), length change (Dil), and species intensity of the $m/z=28$, 44, 48, and 64 signals versus time for 1.0 g of $\text{BaTiO}_3\text{-20}$ heated at 20°C/min in flowing helium.

The $\text{BaTiO}_3\text{-20}$ sample, similarly to the $\text{BaTiO}_3\text{-8}$ sample, has $m/z=12$, 16, 45, and 46 signals with features that correspond to the $m/z=28$ and 44 signals in region I and $m/z=16$, 32, 34, 49, 50, 65, and 66 signals with features that correspond to the $m/z=48$ and 64 signals in region II from Figure 3.12. Table 3.4 compares the peak signal ratios in region I normalized to the $m/z=44$ signal at 69 min (810°C), which show good agreement with the $\text{BaTiO}_3\text{-8}$, CO_2 gas, and tabulated values for the isotopes for CO_2 . Figure 3.11 shows the CO_2 peak in region I for the $\text{BaTiO}_3\text{-20}$ sample occurs at 50°C and 10°C higher than the 8°C/min and 14°C/min BaTiO_3 samples, respectively. This is again consistent with activated kinetic processes.

The signals in region II from Figure 3.12 show two small peaks at 75 min (930°C) and 78 min (990°C), one at either end of a plateau-like feature, which are where the peak intensity ratios are normalized to the $m/z=64$ signal in Table 3.5. The comparison of these SO_2 signals match well to what was observed with the other BaTiO_3 samples. The first peak is 30°C higher than the first peak of the BaTiO_3 -14 sample, and is consistent with what has been mentioned above. The second peak, however, is at the same temperature of the second peak from the BaTiO_3 -8 sample and both are 10°C lower than the second peak of the BaTiO_3 -14 sample.

The lower intensity features related to CO_2 and SO_2 signals in region III of Figure 3.12 are similar to what is observed in both the BaTiO_3 -8 and BaTiO_3 -14 samples.

3.3.8 Loose Barium Titanate Heated at 14°C/min

The evolved intensities for the $m/z=28$, 44, 48, and 64 signals and temperature are plotted versus time in Figure 3.13 for the BaTiO_3 -14L loose powder sample heated at 14°C/min in flowing helium. The time over which the signals are observed is divided into three regions, similarly to the previous BaTiO_3 samples, and are shown along with the peak temperatures for the $m/z=44$ and 64 signals in Table 3.6. Region I contains the low temperature features and peaks of the $m/z=28$, and 44 signals, the peak and high temperature shoulder of the $m/z=48$ and 64 signals appear in region II, and region III includes the $m/z=28$, 44, 48, and 64 signals of lower intensity.

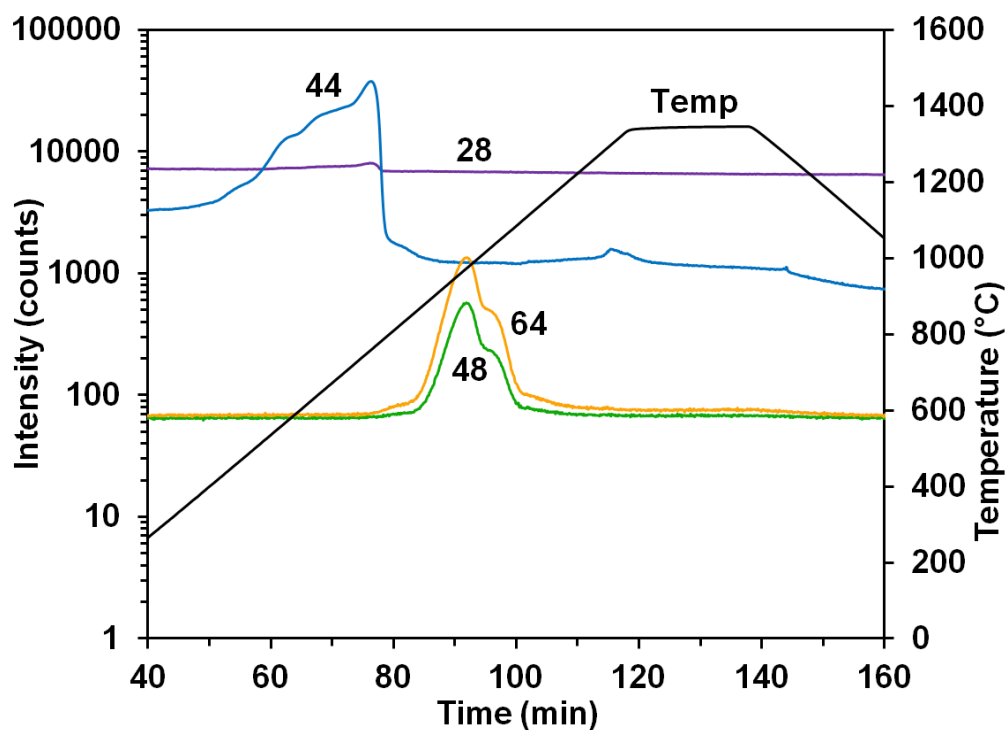


Figure 3.13: Temperature (Temp) and species intensity of the $m/z=28$, 44, 48, and 64 signals versus time for 0.2 g of $\text{BaTiO}_3\text{-14L}$ heated at 14°C/min in flowing helium.

The CO_2 signals, typified by the $m/z=44$ signal in region I of Figure 3.13, are listed in Table 3.4 and show agreement with what was observed for the pressed BaTiO_3 samples. Figure 3.11 shows that the $m/z=44$ signal for the loose sample is at a lower intensity overall at about 1/4-1/5 the intensity than the pressed sample at the same heating rate, which is expected since the mass of the pressed sample is five times the mass of the loose sample. The $m/z=44$ signal has less pronounced lower temperature features ($T < 600^\circ\text{C}$) and the main peak is sharper than the pressed samples at all heating rates, along with the peak occurring 40°C earlier than the pressed sample of the same heating rate. The differences in the CO_2 signal between the pressed and loose powder samples may be caused by the different source locations, whether the gas is being evolved from

the particle surface or if the gas is diffusing out from the interior of the particles. As hypothesized by Schurwanz *et. al.* [15] after examining a similar system using the CDMS, pressing the powder may cause particle fragmentation, allowing gas to be evolved at lower temperatures due to shorter diffusion lengths. The loose powder shows more gas evolution at higher temperatures, where diffusion and surface area changes are occurring in the early stages of sintering.

The main SO₂ signals in region II ($m/z=48$ and 64) of Figure 3.13 have similar signals of lower intensity with similar features as in the previous BaTiO₃ samples, which are listed in Tables 3.5. Through the normalization of the peak intensities in region II to the $m/z=64$ signal in Table 3.5, it is observed that the ratios are consistent with the values for the other BaTiO₃ samples. As listed in Table 3.6 and seen in Figure 3.11, the SO₂ signal peak temperature of the loose sample is between the two peaks of the pressed BaTiO₃ sample, but the loose sample also contained a high temperature shoulder near 1000°C. The total amount of the SO₂ signal evolved from the loose sample is about 18% larger than what is evolved by the pressed sample at the same heating rate, after correcting for the lower weight of the loose sample. The shift of SO₂ evolution from a higher to a lower temperature when pressing the powder is consistent with what is observed in with the evolution of CO₂ as mentioned above and is likely to be caused by the same means.

Region III in Figure 3.13 shows low intensity features from the same signals as the CO₂ and SO₂ signals in regions I and II. These features were also present in the pressed BaTiO₃ samples, although in the loose sample, the features are much less pronounced. Since this was not a pressed sample and no dilatometer data was gathered, it

is not observable when sintering took place. The final powder was friable, evidence that very little sintering occurred.

3.4 Discussion

A combined dilatometer mass spectrometer was used to study the gases evolved at high temperature during the heating and sintering of barium titanate and compounds used to synthesize barium titanate. Mass spectrometry is a valuable analytical tool for assessing gas phase chemistry in that it has a rapid detection time and provides real-time data acquisition. A difficulty in using the MS is that it also commonly causes fragmentation of larger species during ionization that result in multiple signals. Another difficulty is that the MS only detects mass/charge ratios. To circumvent these shortcomings, tabulated cracking patterns and isotopic abundances, along with model compounds, were used to identify the evolved gases.

The completion of the evolution of CO₂ gas before the evolution and conclusion of the SO₂ gas, which occur before the onset of sintering, provide useful insight into the sequence of events that happen before the sample sinters. This information can be used to tailor sintering cycles, such as inserting constant temperature holds when gases are evolved, which could potentially reduce the cost of manufacturing.

Changing the atmosphere to a different inert gas or using oxygen-rich or reducing gases could allow greater control over desired properties in the final product. Properties that have been shown to affect the dielectric behavior of barium titanate and that can be influenced by the sintering atmosphere include oxygen vacancies, microstructure interfaces, and internal stresses and defects. Inert or reducing atmospheres also allows for

the use of base metal electrodes in the manufacturing of barium titanate capacitors, which are cheaper than other metals that can withstand the oxygen-rich atmospheres used to sinter the barium titanate.

The ability to direct microstructure evolution of the material during sintering can also be accomplished by altering the heating rates over different temperature ranges. These tailored sintering cycles take advantage of the competition between the grain growth and densification of the particles. Examples of these cycles include rate-controlled sintering, two-step sintering, and non-isothermal rapid-rate sintering, all of which attempt to control grain growth behavior before densification occurs. These tailored sintering cycles produce a more uniform microstructure, and consequently, more uniform properties throughout the final product, producing less variability in performance at smaller scales.

3.5 Conclusions

Throughout the heating cycles of barium sulfate, barium carbonate, and both loose and pressed barium titanate samples heated at different rates, high temperature reactions and length changes were observed using a combined dilatometer mass spectrometer. Gas phase species were observed for all of the samples, and the sample length was monitored for the pressed barium titanate samples. At lower temperature, the evolution of carbon dioxide from the samples is observed along with the major evolution occurring at an intermediate temperature. Immediately following the peak and subsequent signal drop of carbon dioxide, the species evolved at high temperature, near the onset of sintering, was assigned to sulfur dioxide. The identification of the gas phase species was

accomplished by using reference cracking patterns, isotope abundances, carbon dioxide gas reference, barium carbonate, and barium sulfate. The CDMS has shown to be a useful analytical tool in identifying impurities, which would be helpful in quality control when developing new methods of BaTiO₃ powder synthesis and sintering.

3.6 References

1. H. Morikawa and T. Ishizuka, "Determination of Impurities in Barium Titanate by Inductively Coupled Plasma Atomic Emission Spectrometry," *Analyst*, **112** 999-1002 (1987).
2. D. Hilton and R. Frost, "Recent Developments in the Manufacture of Barium Titanate Powders," *Key Engr. Mats.*, **66-7** 145-184 (1992).
3. D. S. Filimonov, Z.-K. Liu, and C. A. Randall, "Phase Relations in the BaO-TiO_{2-δ} System Under Highly Reducing Conditions," *Materials Research Bulletin*, **38** 545-553 (2003).
4. S. Lee, C. A. Randall, and Z.-K. Liu "Comprehensive Linkage of Defect and Phase Equilibria through Ferroelectric Transition Behavior in BaTiO₃-Based Dielectrics: Part 2. Defect Modeling under Low Oxygen Partial Pressure Conditions," *Journal of the American Ceramic Society*, **91** 1753-1761 (2008).
5. P. Turlier, "BaTiO₃ Synthesis and some of its Properties," *Chimie Moderne*, **4** 135-6 (1959).
6. L. A. Malysh, L. G. Gaisin, M. F. Volkova, A. G. Prokhorov, and K. V. Tkachev, "Reduction of Recycled Barium Sulfate," *Russian Journal of Applied Chemistry*, **75** 15-18 (2002).
7. R. Kresse, "Barium and Barium Compounds"; pp.1-21 in *Ullmann's Encyclopedia of Industrial Chemistry*, John Wiley & Sons, 2007, http://dx.doi.org/10.1002/14356007.a03_325.pub2, (retrieved April 17, 2012).
8. N. Kubota, T. Sekimoto, K. Shimizu, "Precipitation of BaCO₃ in a Semi-Batch Reactor with Double-Tube Gas Injection Nozzle," *Journal of Crystal Growth*, **102** 434-440 (1990).
9. D. L. Perry, "Inorganic Compound Data," p. 51 in *Handbook of Inorganic Compounds (2nd ed.)*, CRC Press, 2011.
10. P. Patnaik, p. 119 in *Handbook of Inorganic Chemical Compounds*, McGraw-Hill, 2003.
11. E. Reck and M. Richards, "TiO₂ Manufacture and Life Cycle Analysis," *Pigment & Resin Technology*, **28** 149 (1999).
12. Landolt-Börnstein, "Numerical Data and Functional Relationships in Science and Technology"; pp. 4-131-136 in *Handbook of Chemistry and Physics (92 ed.)*, CRC Press, Boca Raton, FL, 2011-12.

13. S. E. Stein, "Mass Spectra"; in *NIST Chemistry WebBook, NIST Standard Reference Database Number 69*, Edited by P. J. Linstrom and W. G. Mallard, National Institute of Standards and Technology, <http://webbook.nist.gov>, (retrieved August 31, 2010).
14. J. S. Coursey, D. J. Schwab, J. J. Tsai, and R. A. Dragoset, *Atomic Weights and Isotopic Compositions*, National Institute of Standards and Technology, <http://www.nist.gov/pml/data/comp.cfm>, (retrieved August 31, 2010).
15. M. Schurwanz, J. W. Yun, C. S. Kim, and S. J. Lombardo, "Evolved Gas Analysis During Sintering of Strontium Titanate," *Adv. Appl. Ceram.*, **111** 443 (2012).
16. J. A. S. Bett and W. K. Hall, "The Microcatalytic Technique Applied to a Zero Order Reaction: The Dehydration of 2-butanol over Hydroxyapatite Catalysts," *Journal of Catalysis*, **10** 105 (1968).
17. M. Riazi, "Estimation of Rates and Enhancement Factors in Gas Absorption with Zero-Order Chemical Reaction and Gas-Phase Mass-Transfer Resistances," *Chemical Engineering Science*, **41** 2925 (1986).
18. N. Bhaskarwar, "Analysis of Gas Absorption Accompanied by a Zero-Order Chemical Reaction in a Foam Film Surrounded by Limited Gas Pockets," *Journal of Chemical Technology and Biotechnology*, **38** 183 (1987).
19. U. Neidhardt, H. Schubert, E. Bischoff, and G. Petzow, "Gas Pressure Sintering of Si_3N_4 in $\text{N}_2/\text{CO}/(\text{CO}_2)$ Atmosphere," *Key Engineering Materials*, **89-91** 187-192 (1994).
20. P. Rocabois, C. Chatillon, C. Bernard, "Thermodynamics of the Si-O-N System: II, Stability of $\text{Si}_2\text{N}_2\text{O}(\text{s})$ by High-Temperature Mass Spectrometric Vaporization," *Journal of the American Ceramic Society*, **79** 1361 (1996).
21. K. Feng and S. J. Lombardo, "High-Temperature Reaction Networks in Graphite Furnaces," *J. Mat. Sci.*, **37** 2747-2753 (2002).
22. L. Cabrera, F. Vargas, and R. A. Zarate, "Adsorption of Carbon Dioxide by Barium Titanate: Evidence of Adsorption Process Mediated by a Dipole-Dipole Interaction," *Journal of Physics and Chemistry of Solids*, **55** 1303 (1994).
23. C. Hérard, A. Faivre, and J. Lamaître, "Surface Decontamination Treatments of Undoped BaTiO_3 -Part I: Powder and Green Body Properties," *Journal of the European Ceramic Society*, **15** 135 (1995).

Chapter 4

High Temperature Chemistry of Zirconium Diboride and Sintering Additives

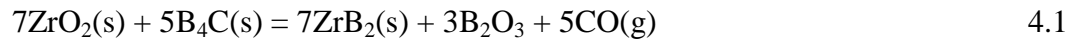
4.1 Introduction

Zirconium diboride (ZrB_2) is an ultra-high temperature ceramic (UHTC) with a melting temperature $>3000^\circ\text{C}$, and also exhibits high hardness (23 GPa) and Young's modulus (489 GPa) [1]. The high thermal conductivity (60 W/(m K)), low electrical resistivity ($10^{-5} \Omega \text{ cm}$), and resistance to chemical degradation of this material, combined with the physical properties, make this material useful for applications in high temperature environments such as refractory linings, cutting tools, high temperature electrodes, and hypersonic flight vehicles [2].

The most common densification method of pure ZrB_2 is hot pressing [3] at high temperatures ($>2000^\circ\text{C}$) and pressures ($>20 \text{ MPa}$). The difficulty in attaining dense ZrB_2 is caused by its high melting temperature, strong covalent bonds, low self-diffusion rates, and the presence of surface oxides of ZrO_2 and B_2O_3 [4] that cause mass transfer without densification. The activation of grain boundary and volume diffusion necessary for sintering occurs at temperatures above 1800°C [5].

Many recent studies reduce the temperature and pressure needed for densification through the use of additives, and these additives also allow for the exploration of other sintering techniques [6-13]. Successful additives include metals and non-oxide ceramics [14], but these frequently change the properties of the pure ZrB_2 to less than desirable values through modifications to the microstructure. The current search for the ideal additive includes the ability to lower the temperature and pressure necessary for densification while maintaining the values of pertinent properties. The additives used with ZrB_2 and their suspected influence on chemistry are reviewed below.

The excellent hardness (25-35 GPa) and high melting temperature (2450°C) of boron carbide (B_4C) are attractive for use as an additive with ZrB_2 . Pressureless sintering to 2050°C of ZrB_2 with the addition of 4 wt% of B_4C by Zhang et al. [15] resulted in a 95% relative density sample, compared to 62% without B_4C . The enhancement in sintering was attributed to the removal of surface ZrO_2 via the formation of a boron oxide (B_2O_3) liquid by the following reaction [1]:



The above reaction occurs at temperatures $>1220^\circ\text{C}$ and allows higher densification by preventing ZrB_2 coarsening. Boron carbide itself is highly inert and TGA measurements by Lee and Speyer [16] for B_4C pressed pellets show a 3-4% weight loss for samples heated in argon above 1400°C , with the major weight loss occurring between 1200°C and 1400°C . The species evolved during the period of weight loss were not identified but were speculated to be B_2O_3 based on mass loss after heating to 380°C , 800°C , 1000°C , 1200°C and 1400°C and mass recovery in moist and dry air.

Another additive for ZrB_2 is silicon carbide (SiC), which has a high decomposition temperature ($>2800^\circ\text{C}$) [17], Young's modulus (>400 GPa), and hardness (>24 GPa) [18]. The role of SiC is to reduce both the amount of oxidation [19] and the oxidation rate of ZrB_2 [19, 20]. In air, pure ZrB_2 oxidizes and forms a B_2O_3 liquid layer by the following mechanism [21]:

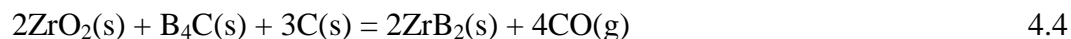


which prevents oxygen transport to the ZrB_2 surface. At temperatures $>1400^\circ\text{C}$, the rapid evaporation of the B_2O_3 layer causes an increase in the rate of ZrB_2 oxidation. The oxidation of SiC via [22]:

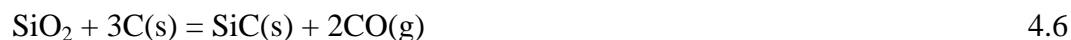
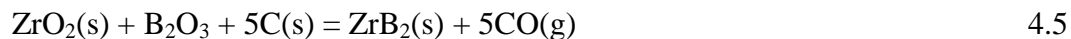


occurs at temperatures $>1400^\circ\text{C}$ and produces an SiO liquid layer that is able to, when added to ZrB_2 powder, prevent oxygen transport to the ZrB_2 surface at higher temperatures since SiO is less volatile than B_2O_3 [19].

Some studies have also used multiple additives. For example, a powder system of ZrB_2 with 5 wt% excess carbon, 4 wt% B_4C , and 10-30 vol% SiC has been used to pressureless sinter to $>98\%$ relative density at 1950°C [10]. Excess carbon is added since the addition of B_4C alone to the ZrB_2 -SiC system is ineffective at removing all of the oxide impurities. The formation of a B_2O_3 liquid layer, via Equation 4.1, can be prevented by the addition of excess carbon by the mechanism:



which is favorable beginning at 1400°C . The B_2O_3 - SiO_2 liquid layer can also be removed by the addition of excess carbon:



Equation 4.5 occurs above 1510°C [1] and Equation 4.6 occurs above 1520°C [23].

In summary, a number of additives can be used with ZrB_2 , and these additives lead to evolution of species into the gas-phase at high temperature. Equations 4.1 and 4.3-4.6 all lead to CO evolution, and Equations 4.1 and 4.2 lead to B_2O_3 which can also appear in the gas phase. In this chapter, the concurrent collection of gas phase chemistry and length change data during the heating of ZrB_2 , B_4C , SiC, B_2O_3 , and ZrO_2 powders was investigated using a combined dilatometer mass spectrometer (CDMS). The purpose of examining the individual ceramic powders before they are combined is to establish an

understanding of the reactions that occur and which can ultimately influence the final sintering behavior of the mixtures.

4.2 Experimental

The CDMS was used to measure the length change and evolved gas during the heating of the different individual powders. An alumina pushrod dilatometer and sample holder is separated from the furnace element environment by a mullite combustion tube. The furnace is evacuated to 0.06 mbar twice and re-filled with high purity helium (99.999%) to approximately 1 bar, after which a flow rate of 135 mL/min is set. The carrier gas enters the mass spectrometer via a fused silica capillary 0.1 mm ID and 45 cm long that is heated to approximately 320°C. A period of 1-2 hours before heating begins is used to allow the flow system to purge completely and to establish baseline signals with the mass spectrometer.

The individual powders ZrB₂ (Grade B, HC Starck, Karlsruhe, Germany), B₄C (Grade HS, HC Starck, Karlsruhe, Germany) and SiC (UF-10, HC Starck, Karlsruhe, Germany) were used to press 0.5 g cylindrical samples to 875 MPa in a 6.4 mm ID steel die and sustained for 1 min. For the pressed samples, calcia-stabilized zirconia spacers were used along with boron nitride sprayed on the sample ends to prevent reaction with the spacers. The 0.015 g of loose ZrO₂ (Aldrich, Milwaukee, WI) powder and the 0.016 g of loose B₂O₃ (¹¹B₂O₃, Aldrich, Milwaukee, WI) powder were placed on the sintered alumina paper and could therefore not be recovered after the heating cycle.

The boron nitride spray (Boron Nitride Aerosol Spray, SP-108, Materion Advanced Chemicals, Milwaukee, WI) sample was prepared by applying approximately

the same amount on the ends of pressed samples to already sintered alumina paper. The amount of mass applied was roughly 0.0001 g after the alumina paper had dried in the hood for 5 minutes. The components of the boron nitride spray are listed in Table 4.1 in the order as they appear on the container, along with the boiling temperatures and four most abundant signals observed in the cracking pattern, if applicable.

Table 4.1: Components of boron nitride spray with the boiling temperature of each and four most abundant m/z ratios of the CPs [24].

Component	Boiling temp (°C)	M.W.	1st CP m/z	2nd CP m/z	3rd CP m/z	4th CP m/z
Acetone	56	58	43	58	15	42
Ethanol	78	46	31	45	29	27
Boron Nitride	2500 [#]	25	-	-	-	-
Ethyl Cellulose	325*	455	-	-	-	-
Xylene	139	106	91	106	105	77
Propane	-42	44	29	28	27	44
n-Butane	-1	58	43	29	27	28

[#]Sublimation Temperature at 1 atm in N₂ [25]

*Decomposition Temperature [26]

The heating rates and hold temperatures for each sample are listed in Table 4.2. The raw dilatometer data were corrected for the spacers and smoothed using the data analysis software (Linseis Data Evaluation, v. 2.18, Linseis GmbH, Germany). To aid in identifying evolved species, the signals were analyzed using several different methods. Cracking patterns (CP) [24] of suspected chemicals and the isotopes [27] of those elements were used when the signals were from expected chemicals. The comparison of unknown signals to other samples that had been heated, such as CO₂ gas, or to a sample of similar composition, such as another oxide or boride, was also used.

Table 4.2: Heating and cooling rates, low and high temperature holds and times for samples examined.

Samples	Heat & cool rate (°C/min)	Low temperature hold (°C, min)	High temperature hold (°C, min)
ZrB ₂	10	300, 40	1500, 20
B ₄ C	10	400, 60	1500, 20
SiC	10	-	1500, 20
ZrO ₂	10	-	1500, 20
B ₂ O ₃	10	-	1400, 20
Boron Nitride Spray	20	-	1648, 20

A common occurrence in the mass spectrometer data for the samples was the contribution of both CO and CO₂ to the m/z=12, 16, and 28 signals. In order to determine the CP of CO when signals for CO₂ were also present, the contribution of CO₂ was subtracted from these signals. The known CP of CO₂ for the CDMS, taken from the CO₂ gas results, was applied to the m/z=44 signal from the sample, and the proportional amount was subtracted from the m/z=12, 16, and 28 signals. For example, the normalized value of the m/z=28 signal according to the CO₂ gas results is 3.2. The m/z=44 signal from the sample is multiplied by 0.032 and the resulting value is subtracted from the m/z=28 signal of the sample. The remaining amount for each signal is then attributed to CO and the CP of CO can then be determined.

4.3 Results

4.3.1 Boron Oxide

Figure 4.1 shows the m/z=18, 28, 32, 44, and 69 signals and temperature versus time for the loose B₂O₃ powder heated at 10°C/min in helium. The final powder was not agglomerated after heating, but appears to have been absorbed into the alumina paper and

formed a dry, brittle flake on the surface of the paper. The low temperature peak of the $m/z=18$ signal occurs at $t=29$ min (230°C) and coincides with a peak of the $m/z=17$ signal of lower intensity. This group of signals is observed in all sample heating cycles and is assigned to H_2O ($m/z=18$) and OH ($m/z=17$). The $m/z=28$, 32, and 44 signal intensities are constant throughout the heating and high temperature soak, indicating that N_2 ($m/z=28$), CO ($m/z=28$), O_2 ($m/z=32$), or CO_2 ($m/z=44$) are not being evolved in significant amounts during the heating cycle.

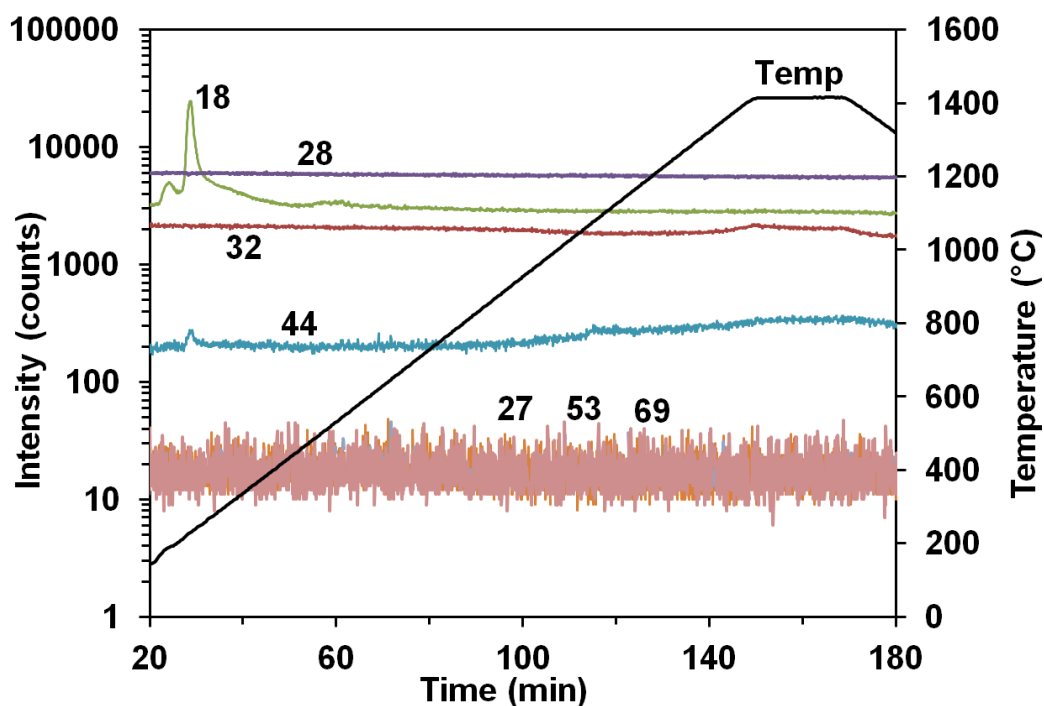


Figure 4.1: Temperature (Temp) and species intensity of the $m/z=18$, 27, 28, 32, 44, 53, and 69 signals versus time for 0.02 g of boron oxide heated to $10^{\circ}\text{C}/\text{min}$ in flowing helium.

The B_2O_3 sample was heated well past the melting temperature of B_2O_3 at 450°C [28] and near the boiling temperature at 1500°C [30]. However, no peaks that can be

assigned to B_2O_3 ($m/z=69$) or its possible cracked species B_2O_2 ($m/z=53$) or BO ($m/z=27$) are observed in Figure 4.1. A previous experiment by Blackburn et al. [31], where the Al_2O_3 - B_2O_3 system was studied using a mass spectrometer in line of sight mode with a Knudsen cell under vacuum conditions, showed that B_2O_3 and fragments thereof such as B , BO , and B_2O_2 were observed up to $1467^\circ C$. The cause for the lack of B_2O_3 related peaks in Figure 4.1 is likely that the vapors condensed in the capillary interface that is maintained at $320^\circ C$, below the melting temperature of B_2O_3 .

4.3.2 Boron Nitride Spray

The boron nitride spray sample was heated at $20^\circ C/min$ in helium and after heating had some residue remaining on the alumina paper which resembled the wetted surface seen immediately after applying the spray. Figure 4.2 shows peaks for the $m/z=16$, 28, 29, 31, 43, 44, and 45 signals that occur at $t=28$ min ($T=340^\circ C$). These signals correspond to some of the main signals (See Table 4.1) for acetone ($m/z=43$, 58, 15, and 42), ethanol ($m/z=31$, 45, 29, and 27), propane ($m/z=29$, 28, 27, and 44), and n-butane ($m/z=43$, 29, 27, and 28) and may correspond to species such as C_2H_3 , C_2H_4 , C_2H_5 , and C_3H_7 , or C_2H_3O respectively, which are listed with their possible sources in Table 4.3. These structures, along with O for the $m/z=16$ signal, can be assigned as the likely sources for the signals in Figure 4.2.

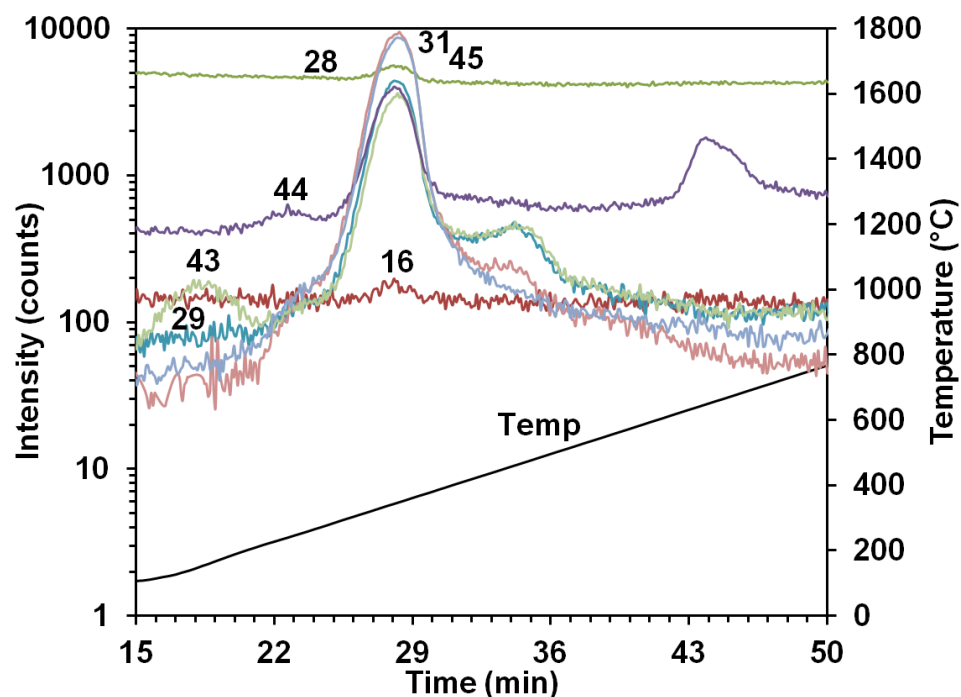


Figure 4.2: Temperature (Temp) and species intensity of the $m/z=16, 28, 29, 31, 43, 44$ and 45 signals versus time for 0.0001 g of boron nitride spray heated at $20^{\circ}\text{C}/\text{min}$ in flowing helium.

The $m/z=44$ signal peak at $t=44$ min ($T=645^{\circ}\text{C}$) is suggestive of propane evolution; however, the larger signals in the CP of propane, the $m/z=29, 28$, and 27 signals, do not have observable peaks at the specified time. The lack of any signal peaks coinciding with the $m/z=44$ signal peak at $t=44$ min does not allow any assignment to be made.

Table 4.3: Select boron nitride spray CP mass to charge ratio with possible sources and possible chemical structures [24].

m/z	Possible sources	Possible chemical structures
15	Acetone, Ethanol, Propane, n-Butane, or Ethyl Cellulose*	CH ₃
27	Propane, n-Butane, Ethanol, Acetone or Ethyl Cellulose*	H ₂ C-CH
28	Propane, n-Butane, Ethanol, Acetone or Ethyl Cellulose*	H ₂ C-CH ₂
29	Propane, n-Butane, Ethanol, Acetone or Ethyl Cellulose*	H ₂ C-CH ₃
31	Ethanol or Ethyl Cellulose*	H ₂ C-OH
42	Acetone, or n-Butane	H ₂ C-CH ₂ -CH ₂
43	Propane, n-Butane, or Acetone	H ₂ C-CH ₂ -CH ₃
43	Ethanol, Acetone or Ethyl Cellulose*	H ₂ C-CH-O
44	Propane	H ₃ C-CH ₂ -CH ₃
45	Ethanol or Ethyl Cellulose*	H ₃ C-CH ₂ -O
58	Acetone	H ₃ C-C(-O)-CH ₃
58	n-Butane	H ₃ C-CH ₂ -CH ₂ -CH ₃
58	Ethyl Cellulose*	H ₃ C-CH ₂ -O-CH
77	Xylene	C ₆ H ₅
77	Ethyl Cellulose*	HC ₅ O
91	Xylene	C ₆ H ₄ -CH ₃
105	Xylene	H ₃ C-C ₆ H ₄ -CH ₂
106	Xylene	C ₆ H ₄ -(CH ₃) ₂

*This work

Other signals arising from the boron nitride spray are shown in Figure 4.3. Peaks appear for the m/z=29, 31, 43, 45, 91, 106, and 108 signals that occur at t=35 min (T=480°C), with the m/z=91, 106, and 108 signals present at a much lower intensity than the other signals. The lower intensity m/z signals are high temperature shoulders of signal peaks that were identified previously to be from acetone, ethanol, propane, n-butane, and ethyl cellulose sources. From the CPs in Table 4.1, an immediate assignment of xylene to the m/z=91 and 106 (C₇H₇ and C₈H₁₀ respectively) signals is possible. Ethyl cellulose,

the structure of which is given in Figure 4.4, has a high molecular weight and decomposes above 325°C. This is a likely source for the $m/z=108$ signal and could contribute to the $m/z=29$, 31, 43, and 45 signals among others from the products of decomposition not shown here.

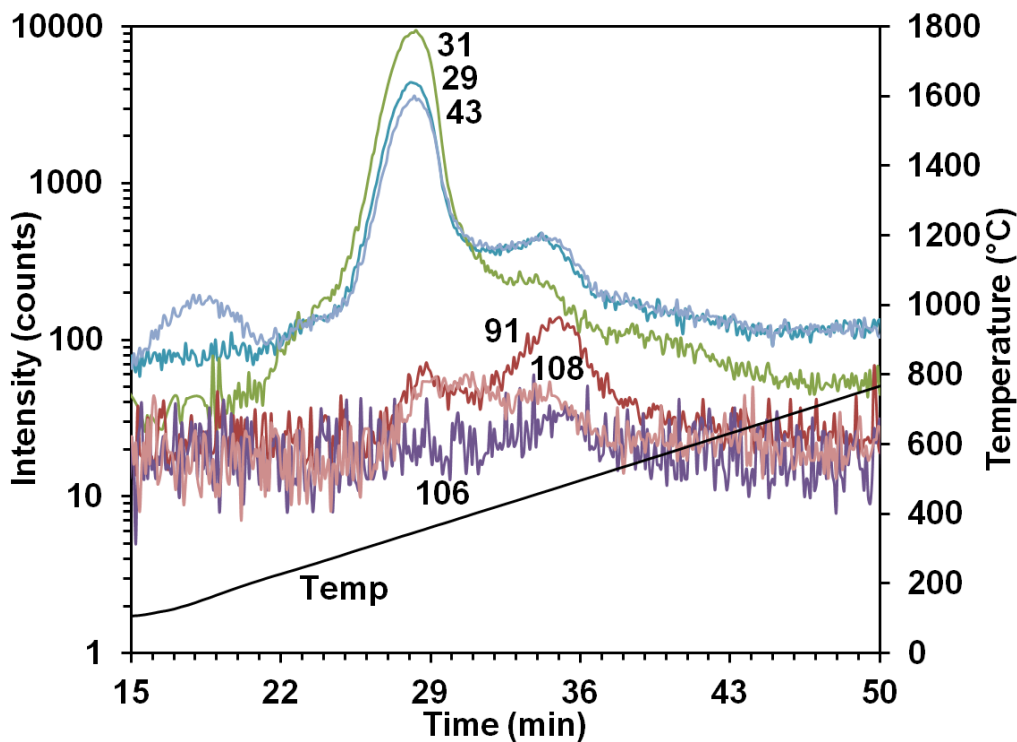


Figure 4.3: Temperature (Temp) and species intensity of the $m/z=29$, 31, 43, 91, 106, and 108 signals versus time for 0.0001 g of boron nitride spray heated at 20°C/min in flowing helium.

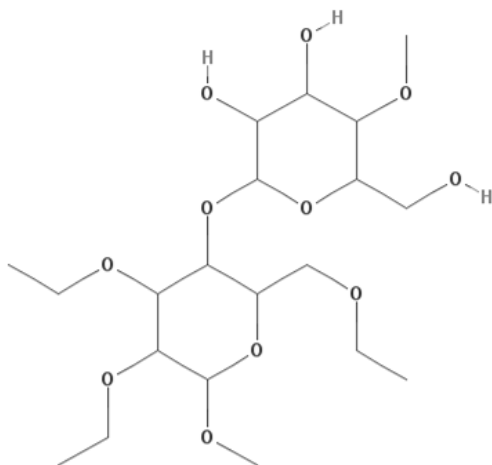


Figure 4.4: Ethyl cellulose structure [29].

4.3.3 Zirconium Diboride

Figure 4.5 shows the temperature profile used for the pressed ZrB_2 sample with ends sprayed with boron nitride and signals $m/z=12$, 16, 28, 44, and 45 versus time for a heating rate of $10^\circ\text{C}/\text{min}$ in helium. The sample decreased 1.3% in mass but did not experience any significant length change from the green to the fired state. The first peaks that occur are observed in the $m/z=16$, 44, and 45 signals at $t=5$ min ($T=120^\circ\text{C}$) followed by the $m/z=16$, 28, 44 and 45 signals at the start of the low temperature 300°C soak at $t=30$ min and directly after the soak. The low temperature peaks from Figure 4.5 have many corresponding peaks in Figure 4.6, typified by the $m/z=27$, 31, 56, 78, 91, and 104 signals. Taken together, these signals are consistent with the evolution of the organics present in the boron nitride spray.

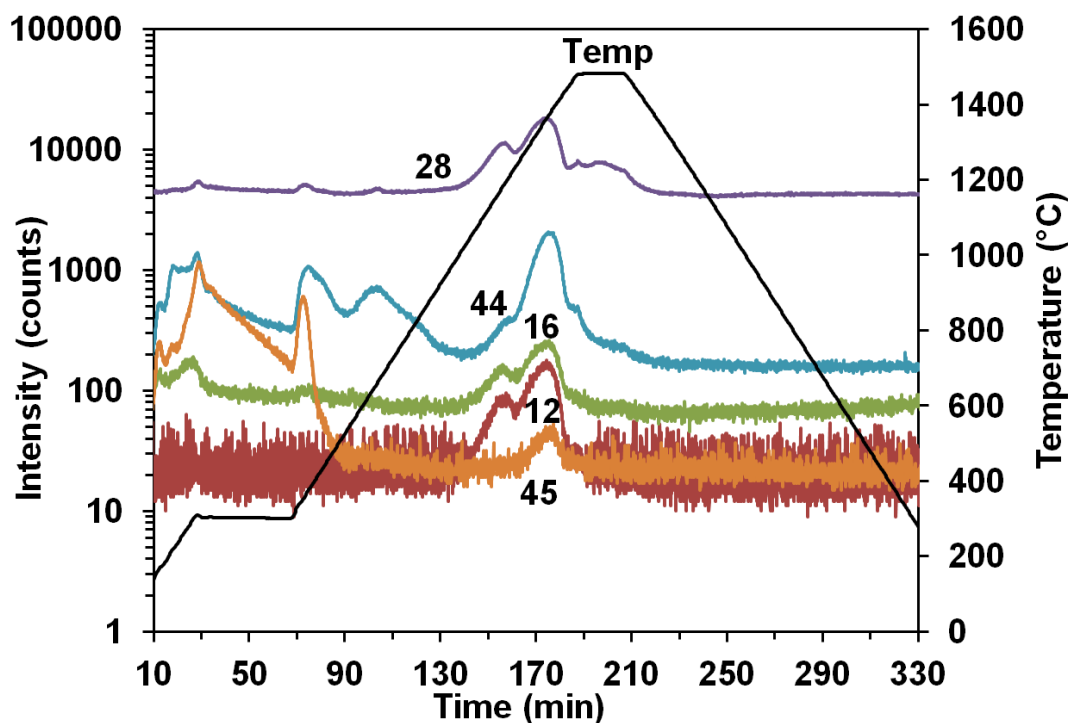


Figure 4.5: Temperature (Temp) and species intensity of the $m/z=12$, 16, 28, 44, and 45 signals versus time for 0.5 g of zirconium diboride heated at $10^{\circ}\text{C}/\text{min}$ in flowing helium.

The next set of peaks in Figure 4.5 are the $m/z=12$, 16, and 28 signals at $t=157$ min (1190°C). The similarity in their profiles suggests that the major peak is CO ($m/z=28$) with O ($m/z=16$) and C ($m/z=12$) arising as the cracked species. The increase of the $m/z=44$ signal, along with the $m/z=12$, 16, and 28 signals, could indicate CO_2 evolution. In the CP of CO_2 , the $m/z=44$ signal is the largest with the next largest being the $m/z=28$ signal, but in the ZrB_2 sample, the $m/z=28$ signal is much larger than the $m/z=44$ signal. The majority of evolved gas from the sample would then be attributed to CO along with a smaller amount of CO_2 .

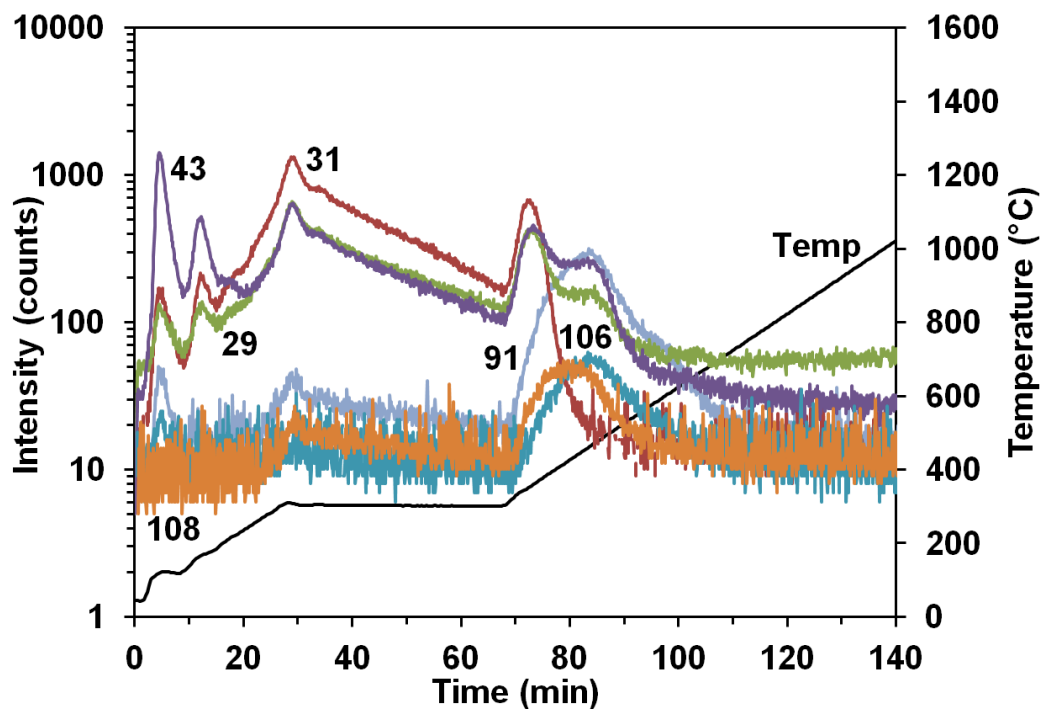


Figure 4.6: Temperature (Temp) and species intensity of the $m/z=29$, 31, 43, 91, 106, and 108 signals versus time for 0.5 g of zirconium diboride heated at $10^{\circ}\text{C}/\text{min}$ in flowing helium.

In order to confirm the assignment of CO at 1190°C , the cracking patterns for the $m/z=12$, 16, and 28 signals can be examined. As seen in Table 4.4, however, the uncorrected CP for the $m/z=16$ signal is larger as compared to the CP seen from CO presented earlier. To improve this, the CP from CO can be corrected by subtracting the CP arising from the smaller CO_2 signal (see Table 4.4). This CP was applied to the $m/z=44$ signal and then subtracted from the $m/z=12$, 16, and 28 signals in Figure 4.4. The resulting $m/z=12$, 16, and 28 signals, with the CO_2 contribution now removed, were next normalized to the $m/z=28$ signal and are shown in Table 4.4. The corrected $m/z=12$ and 16 signals are qualitatively consistent with the NIST CP for CO, with the $m/z=16$ signal in closer agreement than the $m/z=12$ signal. The corrected CP for CO, however, is now

consistent with the CP typically assigned to CO in this work. The assignment of CO is also supported by the lack of other peaks that could be associated with the CP of other chemicals that would have a main peak corresponding to the $m/z=28$ signal, such as the $m/z=14$ signal for nitrogen gas.

Table 4.4: Comparison of normalized m/z ratios evolved from zirconium diboride, boron carbide, silicon carbide, and carbon dioxide, and tabulated values corresponding to the cracking pattern (CP) for carbon monoxide [24].

Source	Peak	Peak intensity at m/z ratios normalized to $m/z = 28$		
		12	16	28
ZrB ₂ *	1190	0.8	1.4	100
ZrB ₂	1190	0.9	1.1	100
ZrB ₂	1360	0.9	1.1	100
B ₄ C	1390	1.1	1.3	100
SiC-1	1370	1.1	1.4	100
SiC-1	1480	1.2	1.4	100
CO ₂ gas [#]	1500	0.3	1.3	3.2
NIST CP for CO		4.7	1.7	100
Possible Compounds		¹² C	¹⁶ O	¹² C ¹⁶ O

*Uncorrected values

[#]Normalized to $m/z=44$

The $m/z=12$, 16, 28, 44, and 45 signals all have major peaks at $t=174$ min (1360°C) with the two largest peaks, the $m/z=28$ and 44 signals, again suggesting that the evolved species may be CO ($m/z=28$) and CO₂ ($m/z=44$). The possibility of CO being evolved is supported by the similarity in the CP of the $m/z=12$, 16, and 28 signals between the $t=157$ min (1190°C) and $t=174$ min (1360°C) peaks. The same analysis to remove the CO₂ contribution to the $m/z=12$, 16, and 28 signals for the peaks at 1190°C was done for the peaks at 1360°C and the results are shown in Table 4.4. The CP of the

m/z=12, 16, and 28 signals for 1360°C is identical to the 1190°C CP and can be once again assigned to CO. The m/z=44 signal is again assigned to CO₂ which is also consistent with the appearance of the m/z=45 (¹³CO₂) signal that mimics the m/z=44 signal profile.

Another possible contribution to the relative amounts of CO and CO₂ can be explained by investigating the equilibrium reactions of carbon and oxygen:



Equation 4.8 has been shown to be dominant over Equation 4.7 at elevated temperatures (T>500°C), resulting in a higher CO signal than CO₂ in the presence of excess carbon [32].

The presence of trace carbon and oxygen in the sample can be explained by examining the common synthesis route of ZrB₂. A common practice is to use boron carbide combined with excess carbon as reducing agents [33] for zirconium oxide. This reduction reaction as given by Equation 4.4 begins at 1200°C, but ZrO₂ is not fully converted until a minimum temperature of 1800°C is reached [5]. In order promote final powder purity, excess boron carbide is added and heated to temperatures above 1220°C as shown in Equation 4.1 [1]. Zirconium diboride powder produced by using excess B₄C according to Equations 4.1 and 4.4 by Sonber et al. [5] contain a minimum of 2% carbon and oxygen impurities when the synthesis temperatures are between 1200-1600°C, whereas the impurities are less than 0.5% when the temperature is raised above 1875°C. During heating, excess carbon can combine with the surface ZrO₂ and surface B₂O₃ or

with oxygen impurities in the starting ZrB_2 powder (0.9 wt% oxygen in Starck [11]) to form CO or CO_2 gas.

4.3.4 Boron Carbide

Figure 4.7 shows the $m/z=12, 16, 28, 44,$ and 45 signals and temperature of pressed B_4C , ends sprayed with boron nitride and heated at $10^\circ\text{C}/\text{min}$ in helium, versus time. The sample experienced a 3.6% weight loss after heating but there was no measurable dimensional change. The low temperature peaks of these signals at $t=32$ min (350°C) and $t=106$ min (490°C) coincide with other signals that have been attributed to the evolution of species associated with the organics in the boron nitride spray.

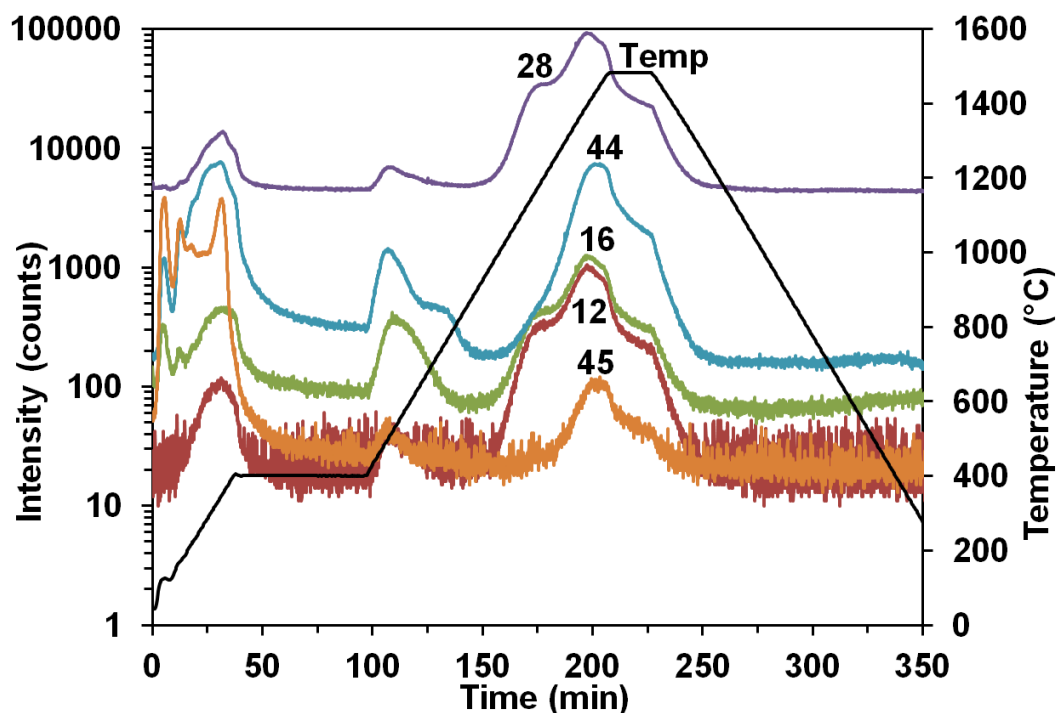


Figure 4.7: Temperature (Temp) and species intensity of the $m/z=12, 16, 28, 44,$ and 45 signals versus time for 0.5 g of boron carbide heated at $10^\circ\text{C}/\text{min}$ in flowing helium.

A family of high temperature peaks for the $m/z=12$, 16, 28, 44, and 45 signals appear at $t=197$ min (1390°C) with low and high temperature shoulders, with largest intensities at the $m/z=28$ and 44 signals; these peaks are suggestive of CO and CO_2 , respectively. To provide further evidence for this assignment, the $m/z=12$ and 16 signals were corrected for the contributions from the $m/z=44$ signal, as was done earlier for the signals evolved from the ZrB_2 sample at 1360°C . Table 4.4 shows that the corrected CP is slightly higher but still in good agreement to what was observed earlier. The assignment of the peaks at 1390°C to CO and CO_2 are in the same temperature range as the TGA results of Lee and Speyer [16], which occurred between 1000°C - 1500°C . These authors attributed the mass loss to B_2O_3 based on the increase in vapor pressure and the decrease in mass recovery caused by the rehydration of the boron oxide coatings, indicating a loss of the coatings after heating to above 1200°C .

The origin of the CO and CO_2 can be explained as arising from impurities in the powder. For example, the same grade B_4C powder as used here has been shown to contain 1.3 wt% oxygen [2,8] impurities, which are likely in the form of the surface oxide B_2O_3 [2, 8, 16]. Excess free carbon is often present in B_4C powder [34] and this occurs from the synthesis of B_4C by the decomposition reaction [35]:



The reduction of B_2O_3 by carbon and boron carbides by the following reactions [6]:



The temperature requirements of 1250°C for both Equations 4.10 and 4.11 are exceeded in the heating of the B₄C sample and are therefore the main contributors to the evolution of CO observed in Figure 4.7. No evidence for the evolution of boron oxides was observed, and this is again attributed to condensation in the cooler CDMS interface.

4.3.5 Silicon Carbide

Figure 4.8 shows the m/z=12, 16, 28, 44, and 45 signals and temperature versus time of pressed SiC coated with boron nitride spray on the ends and heated at 10°C/min in helium. The sample experienced 2.7% mass loss from green to fired state and a decrease in volume corresponding to an increase from 0.59 to 0.62 of theoretical density. The signals in Figure 4.8 show low temperature peaks at t=21 min (350°C) and, with other signals that have similar peaks at that temperature, can again be attributed to the evolution of the organics from the boron nitride spray.

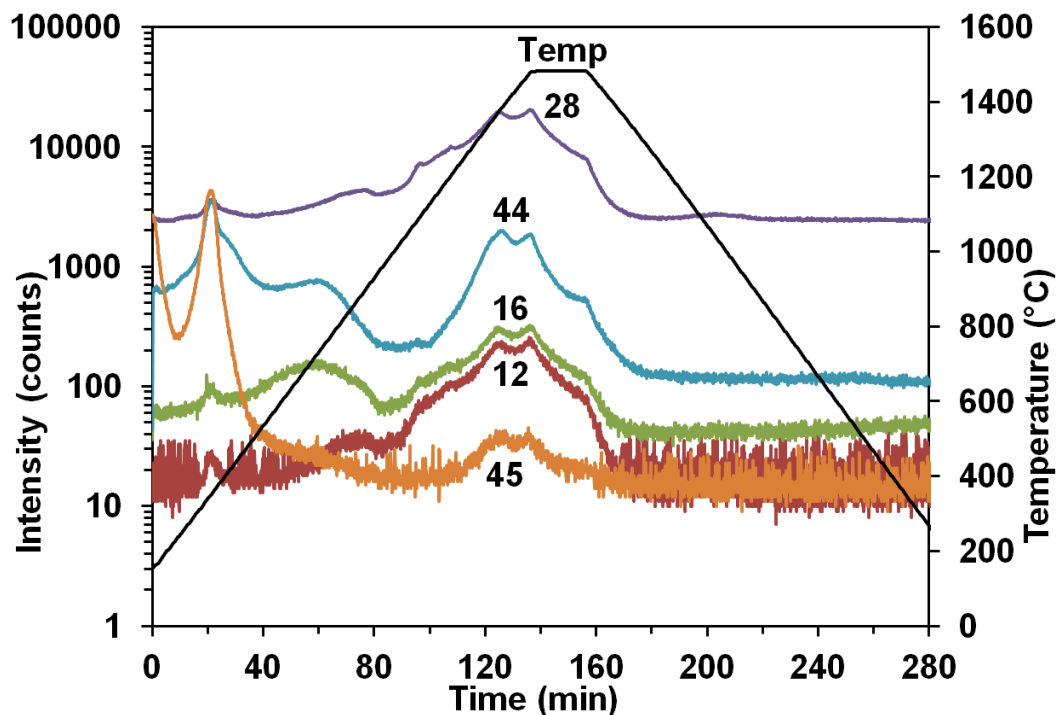


Figure 4.8: Temperature (Temp) and species intensity of the $m/z=12$, 16, 28, 44, and 45 signals versus time for 0.5 g of silicon carbide heated at $10^{\circ}\text{C}/\text{min}$ in flowing helium.

The high temperature double peaks of the large $m/z=28$ and 44 signals at $t=125$ min (1370°C) and $t=136$ min (1480°C) with high and low temperature shoulders are also seen in Figure 4.8. The same analysis as was used for the ZrB_2 sample was applied to remove the CO_2 contribution from the $m/z=12$, 16, and 28 signals. The resultant CP for CO is shown in Table 4.4 for both of these peaks and are similar to the CP of CO from the B_4C sample and slightly larger than for the ZrB_2 sample, but can still be assigned to CO.

One possible source for the CO can be unreacted carbon from the production of SiC by the carbothermal reduction of SiO_2 with carbon in an electric resistance furnace, as shown in Equation 4.6. The silica oxide layer that is formed on the surface of SiC can

also contribute to production of CO by reacting with SiC at low oxygen partial pressure (30 Pa) and elevated temperatures ($T > 1400^{\circ}\text{C}$) [18] according to:



Under these same conditions, the oxygen that is present can oxidize the SiC and produce CO [22] via Equation 4.3. A product in both Equation 4.3 and 4.12 is SiO gas which would have signals for SiO ($m/z=44$), Si ($m/z=28$), O ($m/z=16$) and ^{29}SiO ($m/z=45$), which are many of the same masses in the CPs of CO and CO₂. The assignment of CO and CO₂ for the signal peaks in Figure 4.8 can be confirmed by the similar CP value for the $^{13}\text{CO}_2$ ($m/z=45$) isotope compared to the ZrB₂, and B₄C samples versus the ^{29}SiO value from the isotope abundance for ^{29}Si of 4.7% [27]. The presence of the C ($m/z=12$) signal would also confirm the assignment of CO₂ over SiO except that the very large $m/z=12$ signal from CO is also present.

Silica can also dissociate at high temperatures ($T > 1710^{\circ}\text{C}$) [36], providing another source of oxygen that can potentially combine with the excess carbon to form CO and CO₂:



It is unlikely that the reaction from Equation 4.13 occurred in the SiC sample since the maximum temperature during the heating cycle was 1500°C .

4.3.6 Zirconium Oxide

Figure 4.9 shows the intensities of the $m/z=16$, 28, 32, 44, 48, and 64 signals and temperature versus time for loose ZrO₂ powder heated at 10°C/min in helium. The heated powder remained in loose agglomerated form similar to the as-received powder before

heating except for some hardening of the agglomerates. The $m/z=48$ and 64 signal peaks at $t=83$ min (845°C) are at very low intensity and are suggestive of SO ($m/z=48$) and SO_2 ($m/z=64$) evolution, as was seen in the previous chapter for the BaTiO_3 samples. The analysis of the CP in Table 4.5 shows that the $m/z=64$ signal intensity is approximately double the $m/z=48$ signal, which is consistent with the CP of SO_2 [37]. Unfortunately, the intensities of the $m/z=48$ and 64 signals are so low that the other signals associated with the CP of SO_2 do not have observable peaks, which are seen in the BaTiO_3 and SrTiO_3 samples in Table 4.5.

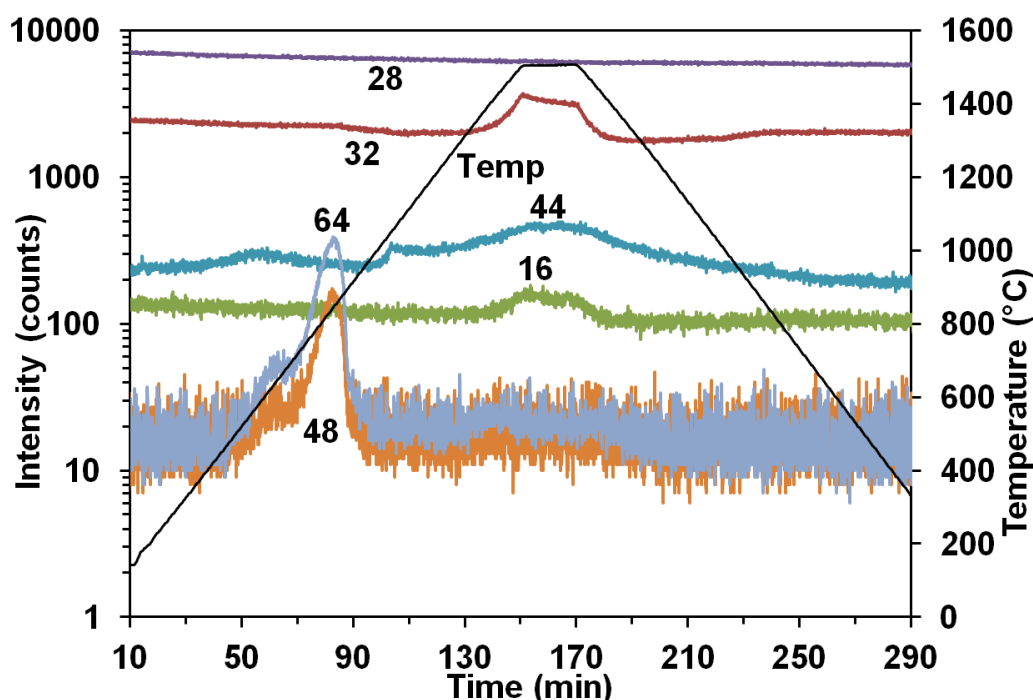


Figure 4.9: Temperature (Temp) and species intensity of the $m/z=16$, 28, 32, 44, 48, and 64 signals versus time for 0.015 g zirconium oxide heated at $10^{\circ}\text{C}/\text{min}$ in flowing helium.

Table 4.5: Comparison of normalized m/z ratios evolved from zirconium oxide, carbon dioxide, barium titanate, and strontium titanate.

Source	Peak	Peak intensity at m/z ratios normalized to m/z = 64				Peak intensity at m/z ratios normalized to m/z = 44		
	Temp (°C)	16	32	48	64	16	32	44
ZrO ₂	845	-	-	40.5	100			
ZrO ₂	1500					18	589.7	100
CO ₂ gas	1500					1.3	-	100
BaTiO ₃	780					1.0	-	100
BaTiO ₃	1005	1.2	10.9	38.2	100			
SrTiO ₃	1000	11.4	28.1	51.4	100			
Possible Compounds		¹⁶ O	¹⁶ O ₂	³² S ¹⁶ O	³² S ¹⁶ O ₂	¹⁶ O	¹⁶ O ₂	¹² C ¹⁶ O ₂

The m/z=16, 32, and 44 signals all show peaks during the high temperature soak at t=150-170 min (1500°C). This set of features is commonly observed directly following an inert conditioning cycle without a background heating cycle before the sample heating cycle (as seen in Figure 3.2). The m/z=16 and 44 signals are present in the CP of CO₂, but when compared to the CPs of CO₂ gas and the BaTiO₃ sample in Table 4.5, the m/z=16 is much larger in the ZrO₂ sample. Table 4.5 also shows a larger O₂ (m/z=32) signal than CO₂ (m/z=44) signal, which is likely contributing to the O (m/z=16) signal. The discrepancy between the m/z=16 signal and the m/z=32 and 44 signals could be caused by multiple chemical interactions between the ZrO₂ sample, the Al₂O₃ of the mullite combustion tube, and the O₂ and CO₂ coming from either the sample or the combustion tube. The intensity of the CO₂ peak for the ZrO₂ sample is also around 10 times smaller than was observed for the CO₂ peaks arising from the ZrB₂, B₄C, and SiC samples. The expected CO (m/z=28) peak to occur with the CO₂ (m/z=44) peak based on

the CP of CO₂ is not distinguishable since the CO signal baseline is much larger than the expected peak.

4.4 Discussion

The observation of chemistry during the heating of zirconium diboride and sintering aids was accomplished using the combined dilatometer mass spectrometer. The pressed samples showed significant amounts of organics evolved at lower temperatures, characteristic of the signals seen from the boron nitride spray which is used to coat the ends of the samples. Similar signals would also occur at lower temperature for samples that used sintering additives such as binders, dispersants, and surfactants.

The mass spectrometer signals from the surface oxides that reacted to produce carbon monoxide and carbon dioxide at elevated temperatures showcases the utility of the CDMS as a tool that can be used in developing methods to improve the densification of zirconium diboride. Surface oxide modification or removal allows densification to occur at lower temperatures and pressures and can produce gas phase species that are monitored by the mass spectrometer. Although the loose B₂O₃ powder did not show the expected gas phase B₂O₃, which is presumed to have condensed in the silica capillary between the furnace and the mass spectrometer. One method that could be used to verify the existence of the B₂O₃ in the capillary is to remove and cut the capillary into smaller segments and test each segment for B₂O₃. This procedure would also give insight into the temperature profile of the capillary during heating cycles and could be performed after every sample heating cycle to determine if there are any condensed species present, but would add considerable time and cost to the testing of samples.

The chemistry will continue to be important as the samples reach temperatures necessary for densification, which was not reached for the materials due to the maximum operating temperature of the CDMS at the time of testing. Increasing the maximum operating temperature of the CDMS would require removing the alumina tubes and silica capillary, and replacing the thermocouples with an optical pyrometer. The capture of species in the gas phase to be transported to the mass spectrometer and the probable increase in furnace environment effects during the heating of samples present challenges that are further discussed in chapter 6.

4.5 Conclusions

Carbides and oxides important to the development of ZrB₂-based composite materials for ultra-high temperature applications were examined using the CDMS. The gas phase chemistry was examined for all samples, and the length of the samples was monitored for the pressed samples. Gas phase species were assigned using measured and tabulated cracking patterns (CP) of relevant compounds, along with tabulated isotope abundances. Low temperature chemistry relating to the evolution of organics from boron nitride spray used on the ends of the pressed samples along with high temperature evolution of CO and CO₂ for the ZrB₂, B₄C, and SiC samples was observed. Negligible length change was observed for these pressed samples, although there was measureable weight loss. The gas phase signals of the loose B₂O₃ and ZrO₂ samples did not show evolution of any compounds that could be attributed to originating from the samples themselves.

4.6 References

1. W. G. Fahrenholtz, G. E. Hilmas, I. G. Talmy, J. A. Zaykoski, "Refractory Diborides of Zirconium and Hafnium," *J. Am. Ceram. Soc.*, **90** 1347-1364 (2007).
2. S. Zhu, W. G. Fahrenholtz, G. E. Hilmas, and S. C. Zhang, "Pressureless Sintering of Zirconium Diboride Using Boron Carbide and Carbon Additions," *J. Am. Ceram. Soc.*, **90** 3660-63 (2007).
3. H. Pastor, "Metallic Borides: Preparation of Solid Bodies. Sintering Methods and Properties of Solid Bodies," pp. 457-93 in *Boron and Refractory Borides*, Edited by V. I. Matkovich. Springer, New York, 1977.
4. R. Telle, L. S. Sigl, and K. Takagi, "Boride-Based Hard Materials" pp. 802-945 in *Handbook of Ceramic Hard Materials*, Vol. 2, Edited by R. Riedel. Wiley-VCH, Weinheim, 2000.
5. J. K. Sonber, T. S. R. Ch. Murthy, C. Subramanian, S. Kumar, R. K. Fotedar, A. K. Suri, "Investigations on the Synthesis of ZrB_2 and Development of New Composites with HfB_2 and $TiSi_2$," *Int. J. Refract. Met. Hard Mater.*, **29**, 21-30 (2011).
6. A. K. Khanra and M. M. Godkhindi, "Effect of Ni Additives on Pressureless Sintering of SHS ZrB_2 ," *Adv. Appl. Ceram.*, **104** 273 (2005).
7. D. Sciti, F. Monteverde, S. Guicciardi, G. Pezzotti, and A. Bellosi, "Microstructure and Mechanical Properties of ZrB_2 - $MoSi_2$ Ceramic Composites Produced by Different Sintering Techniques," *Mater. Sci. Eng. A*, **A434** 303-9 (2006).
8. S. Zhu, W. G. Fahrenholtz, G. E. Hilmas, and S. C. Zhang, "Pressureless Sintering of Carbon-Coated Zirconium Diboride Powders," *Mater. Sci. Eng. A*, **A459** 167-71 (2007).
9. S. K. Mishra and L. C. Pathak, "Effect of Carbon and Titanium Carbide on Sintering Behaviour of Zirconium Diboride," *J. Alloys Compd.*, **465** 547-55 (2008).
10. S. C. Zhang, G. E. Hilmas, and W. G. Fahrenholtz, "Pressureless Sintering of ZrB_2 -SiC Ceramics," *J. Am. Ceram. Soc.*, **91** 26-32 (2008).
11. J. Zou, G. J. Zhang, Y. M. Kan and P. L. Wang, "Pressureless Densification of ZrB_2 -SiC Composites with Vanadium Carbide," *Scr. Mater.*, **59** 309-12 (2008).
12. S.-Q. Guo, Y. Kagawa, T. Nishimura, and H. Tanaka, "Pressureless Sintering and Physical Properties of ZrB_2 -Based Composites with $ZrSi_2$ Additive," *Scripta Materialia*, **58** 579-582 (2008).

13. X. G. Wang, W. M. Guo, and G. J. Zhang, "Pressureless Sintering Mechanism and Microstructure of ZrB_2 -SiC Ceramics Doped with Boron," *Scr. Mater.*, **61** 177-80 (2009).
14. F. Monteverde, S. Guicciardi, and A. Bellosi, "Advances in Microstructure and Mechanical Properties of Zirconium Diboride-Based Ceramics," *Mater. Sci. Eng.*, **A346**, 310-9 (2003).
15. S. C. Zhang, G. E. Hilmas, and W. G. Fahrenholtz, "Pressureless Densification of Zirconium Diboride with Boron Carbide Additions," *J. Am. Ceram. Soc.*, **89** 1544-50 (2006).
16. H. Lee and R. F. Speyer, "Pressureless Sintering of Boron Carbide," *J. Am. Ceram. Soc.*, **86** 1468-73 (2003).
17. J. Drowart and G. DeMaria, pp. 16-23 in *Silicon Carbide, A High Temperature Semiconductor*, Edited by J. F. O'Connor and J. Smiltens, Pergamon Press, Inc., New York, 1960.
18. N. G. Wright, "Silicon Carbide"; pp. 524-546 in *Kirk-Othmer Encyclopedia of Chemical Technology*, John Wiley & Sons, 2006, <http://dx.doi.org/10.1002/0471238961.1909120904092201.a01.pub2>, (retrieved April 17, 2012).
19. P. Sarin, P. E. Driemeyer, R. P. Haggerty, D.-K. Kim, J. L. Bell, Z. D. Apostolov, W. M. Kriven, "In Situ Studies of Oxidation of ZrB_2 and ZrB_2 -SiC Composites at High Temperatures," *J. Eur. Cer. Soc.*, **30** 2375-86 (2010).
20. W. C. Tripp, H. H. Davis, and H. C. Graham, "Effect of an SiC Addition on the Oxidation of ZrB_2 ," *Ceram. Bull.*, **52** 612-6 (1973).
21. L. Kaufman, E. V. Clougherty, J. B. Berkowitz-Mattuck, "Oxidation Characteristics of Hafnium and Zirconium Diboride," *Trns. Met. Soc. AIME*, **239** 458-66 (1967).
22. E. A. Gulbransen and S. A. Jansson, "The High-Temperature Oxidation, Reduction, and Volatilization Reactions of Silicon and Silicon Carbide," *Oxid. Met.*, **4** 181-201 (1972).
23. M. S. Datta, A. K. Bandyopadhyay, and B. Chaudhuri, "Sintering of Nano Crystalline α Silicon Carbide by Doping with Boron Carbide," *Bull. Mater. Sci.*, **25** 181-9 (2002).
24. S. E. Stein, "Mass Spectra"; in *NIST Chemistry WebBook, NIST Standard Reference Database Number 69*, Edited by P. J. Linstrom and W. G. Mallard, National Institute of Standards and Technology, <http://webbook.nist.gov>, (retrieved August 31, 2010).

25. R. H. Wentorf, Jr., "Refractory Boron Compounds"; pp. 673-80 in *Kirk-Othmer Encyclopedia of Chemical Technology*, John Wiley & Sons, 2006, <http://onlinelibrary.wiley.com/doi/10.1002/0471238961.1805061823051420.a01/pdf>, (retrieved May 31, 2012).
26. X.-G. Li, M.-R. Huang, H. Bai, "Thermal Decomposition of Cellulose Ethers," *J. Appl. Poly. Sci.*, **73** 2927-2936 (1999).
27. J. S. Coursey, D. J. Schwab, J. J. Tsai, and R. A. Dragoset, *Atomic Weights and Isotopic Compositions*, National Institute of Standards and Technology, <http://www.nist.gov/pml/data/comp.cfm>, (retrieved August 31, 2010).
28. M. S. Chandrasekharaiah, p. 495 in *The characterization of High Temperature Vapors*, Eds. J. L. Margrave, Appendix B, Wiley, New York, 1967.
29. *Aquacoat* - *PubChem*, U. S. National Library of Medicine, <http://pubchem.ncbi.nlm.nih.gov/>, (retrieved May 21, 2012).
30. P. Patnaik, p. 119 in *Handbook of Inorganic Chemical Compounds*, McGraw-Hill, 2003.
31. P. E. Blackburn, A. Büchler, and J. L. Stauffer, "Thermodynamics of Vaporization in the Aluminum Oxide-Boron Oxide System," *J. Phys. Chem.*, **70** 2469 (1966).
32. K. Feng, S. J. Lombardo, "High-Temperature Reaction Networks in Graphite Furnaces," *J. Mat. Sci.*, **37** 2747-2753 (2002).
33. R. Thomson, "Production, Fabrication, and Uses of Borides"; pp. 113-20 in *The Physics and Chemistry of Carbides, Nitrides and Borides*, Edited by R. Freer, Kluwer Academic Publishers, Dordrecht, 1990.
34. H. J. Brown-Shaklee, W. G. Fahrenholtz, and G. E. Hilmas, "Densification Behavior and Thermal Properties of Hafnium Diboride with the Addition of Boron Carbides," *J. Am. Ceram. Soc.*, 1-9 (2012).
35. A. W. Weimer, p. 131 in *Carbide, Nitride and Boride Materials Synthesis and Processing*, Chapman & Hall, London, New York, 1997.
36. D. W. Green and R. H. Perry, eds., pp. 3-49 in *Perry's Chemical Engineer's Handbook*, 6th ed., McGraw-Hill Book Co., Inc., New York, 1984.
37. M. Schurwanz, J. W. Yun, C. S. Kim, and S. J. Lombardo, "Evolved Gas Analysis During Sintering of Strontium Titanate," *Adv. Appl. Ceram.*, **111** 443 (2012).

Chapter 5

High Temperature Chemistry during the Heating of Mixtures of Ultra-High Temperature Materials

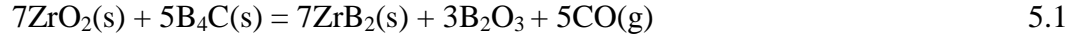
5.1 Introduction

Zirconium diboride (ZrB_2) is classified as an ultra-high temperature ceramic (UHTC) with a high melting temperature $>3000^\circ\text{C}$, and a high hardness of 23 GPa and a large Young's modulus of 489 GPa [1]. These properties, along with high thermal conductivity (60 W/m-K), low electrical resistivity ($10^{-5} \Omega \text{ cm}$), and resistance to chemical degradation, make this material useful for structural applications in high temperature environments such as refractory linings, cutting tools, high temperature electrodes, and hypersonic flight vehicles [2].

Due to its refractory nature, the sintering of pure or nearly pure ZrB_2 requires the high temperatures ($>2000^\circ\text{C}$) and pressures ($>20 \text{ MPa}$) experienced during hot pressing [3]. Many recent densification studies therefore use additives to reduce the temperature and pressure necessary to achieve high density, and several studies also explore alternative sintering techniques [4-11]. Common additives used with ZrB_2 include metals and non-oxide ceramics [12] which have been successful in lowering the conditions at which ZrB_2 sinters; however, the subsequent modifications to the microstructure are commonly coupled with deleterious changes in properties from those of pure ZrB_2 . The current state is thus to find one or more additives that not only increase densification at lower temperatures and pressures, but also retains relevant properties at the desired values. The chemistry of ZrB_2 combined with additives is described below.

Boron carbide (B_4C) has been explored as an additive to ZrB_2 since it also has excellent hardness (25-35 GPa) and a high melting temperature (2450°C). In studies using pressureless sintering to 2050°C in vacuum [13], the addition of 4 wt% of B_4C powder resulted in 95% relative density, compared to 62% without B_4C . The more

complete densification of the sample was attributed to the removal of surface ZrO_2 via the formation of a boron oxide liquid layer at temperatures above 1220°C :



This reaction prevents the coarsening of ZrB_2 [1] by the reduction of surface free energy at temperatures below that which coarsening occurs ($1650\text{-}1850^\circ\text{C}$), through both the transport of oxygen to areas with a high surface free energy in the form of the B_2O_3 liquid, and the removal of oxygen from the surface in the form of CO gas.

Silicon carbide (SiC), which itself has desirable high temperature properties such as a high decomposition temperature ($>2800^\circ\text{C}$) [14], large Young's modulus (>400 GPa), and high hardness (>24 GPa) [15], has also been used as an additive to ZrB_2 . The presence of SiC reduces both the amount of oxidation [16] and the oxidation rate of ZrB_2 [16, 17] according to the following mechanism. In air, pure ZrB_2 oxidizes and forms a B_2O_3 liquid layer via [18]:



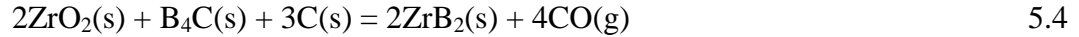
which prevents oxygen transport to the ZrB_2 surface. Rapid evaporation of the B_2O_3 layer at temperatures $>1400^\circ\text{C}$ causes an increase in the rate of ZrB_2 oxidation. The oxidation of SiC at temperatures $>1400^\circ\text{C}$ via [19]:



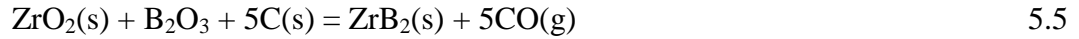
produces an SiO liquid layer that when present on the ZrB_2 powder, prevents oxygen transport to the ZrB_2 surface at higher temperatures. This improved oxidation resistance arises because SiO is less volatile than the B_2O_3 [16].

The addition of B_4C to the ZrB_2 - SiC system has also been examined in order to remove the surface oxide impurities on ZrB_2 according to Eq. 5.1. This strategy,

however, was found to be unsuccessful [8]. When 5 wt% excess carbon along with 4 wt% B_4C , was added to ZrB_2 and 10-30 vol% SiC , this composition sintered without the use of external pressure to >98% relative density at 1950°C in vacuum up to 1650°C and argon above 1650°C [8]. The combination of B_4C plus carbon prevents the formation of B_2O_3 - SiO_2 liquid layers by modifying the mechanism given by Equation 5.1 to:



which is favorable beginning at 1400°C. The liquid layer can also be removed through:



which occurs above 1510°C [1].

Another additive that is able to significantly lower the sintering temperature of ZrB_2 is $ZrSi_2$, which melts at 1620°C [20]. A study by Guo et al. [10] examined the effects of $ZrSi_2$ additions on the densification of ZrB_2 powder and found that adding 20 vol% or greater of $ZrSi_2$ was needed to achieve >99% relative density on samples pressureless sintered to 1650°C in vacuum for 60 min.

In summary, many additives can be used to lower the sintering conditions of ZrB_2 . As indicated by Equation 5.1 to 5.5, the presence of these additives with ZrB_2 can lead to the evolution of gas phase species at high temperature. The gas CO is evolved via Equations 5.1 and 5.3-5.5, and B_2O_3 , with its relatively high vapor pressure, is a product in Equations 5.1 and 5.2. The following work explores the connection between the gas phase chemistry occurring when ZrB_2 is heated to high temperature and length changes of the sample. The sources for the observed species will be investigated in light of previous speculated reactions given for high temperature chemistry of ZrB_2 with these additives.

5.2 Experimental

The CDMS apparatus consists of the furnace/dilatometer, the mass spectrometer, the gas flow system, and the coolant flow system. The interior of the furnace is separated by a mullite or alumina combustion tube to allow the sample environment to be isolated from the heating element environment. A fused silica capillary of 0.1 mm ID and 45 cm long, heated to approximately 320°C, is used to introduce a stream of gas from around the sample into the mass spectrometer. To ensure an inert environment around each sample and in the mass spectrometer, the furnace was evacuated and backfilled with high purity helium (99.999%) to 1 bar, and a steady flow rate of 135 mL/min was established. This continuous purge is maintained for 1-2 hours before the heating of the sample to allow mass signal intensities to reach base-line values. The sample length and the mass to charge (m/z) ratio of the composition of the furnace gas were acquired throughout the heating cycle.

The ZrB₂-B₄C-Phenolic Resin (PR) powder system was prepared by combining ZrB₂ (Grade B, HC Starck, Karlsruhe, Germany) with 2 wt% B₄C (Grade HS, HC Starck, Karlsruhe, Germany) and with a carbon source of 3.75 wt% phenolic resin (Type GP 2074, Georgia-Pacific Chemicals, Atlanta, GA). The mixture was ball milled in acetone for 24 h using WC media, dried, ground using a mortar and pestle, and then screened to 80 mesh [2].

Another powder mixture, ZrB₂-SiC-B₄C-PR-Binder (B)-Dispersant (D)-Surfactant (S), was prepared with the same ZrB₂ powder and 1.8 wt% of the same B₄C powder as above, in addition to 19.9 wt% SiC (UF-10, HC Starck, Karlsruhe, Germany), 1.0 wt% phenolic resin (Type GP 2074, Georgia-Pacific Chemicals, Atlanta, GA), 0.39

wt% binder (QPac 40, Empower Materials, New Castle, DE), 0.54 wt% dispersant (BYK-110, BYK-Chemie USA, Wallingford, CT), and 0.6 wt% surfactant (Santicizer 160, Ferro, Mayfield Heights, OH). The ZrB_2 , SiC, and B_4C were dispersed in methyl ethyl ketone (MEK) or xylene by ball milling with the dispersant for 24 h using WC media. The phenolic resin, binder, and surfactant were next added, and the mixture was ball milled for another 24 h using WC media, dried, and then screened to 45 mesh [8].

A ZrO_2 - B_4C powder mixture was prepared using a 7:5 mol ratio of ZrO_2 (Aldrich, Milwaukee, WI) to B_4C (Grade HS, HC Starck, Karlsruhe, Germany). This mixture was added to isopropyl alcohol, ground using a mortar and pestle, and then dried in air at 100°C for 2 h.

Three other powder systems were prepared using the same ZrB_2 powder as above with 5, 10, and 20 vol% ZrSi_2 (Alfa Aesar, Ward Hill, MA). These mixtures were attrition milled for 24 h with SiC media and designated by ZrB_2 -5- ZrSi_2 , ZrB_2 -10- ZrSi_2 , and ZrB_2 -20- ZrSi_2 .

The above compositions were then uniaxially pressed into 0.5 g cylinders in a 6.4 mm steel die to 875 MPa for the ZrB_2 - B_4C , ZrB_2 -SiC- B_4C , and the ZrO_2 - B_4C powders, and to 200 MPa for the ZrB_2 - ZrSi_2 powders. The pressure was maintained for 1 min. Prior to being loaded in the furnace, the sample ends were sprayed with boron nitride (Boron Nitride Aerosol Spray, SP-108, Materion Advanced Chemicals, Milwaukee, WI) to avoid reaction between the sample and the spacers. All of the samples were heated with calcia-stabilized zirconia spacers (Machined Ceramics, Bowling Green, KY), except for the ZrB_2 -5- ZrSi_2 , ZrB_2 -10- ZrSi_2 , and ZrB_2 -20- ZrSi_2 samples which used Al_2O_3

spacers (A-16, Alcoa, New York, NY). The heating profiles for each powder composition are listed in Table 5.1.

Table 5.1: Heating and cooling rates, low and high temperature holds and times for different samples.

Samples	Heating & Cooling Rates (°C/min)	Low Temperature Hold (°C, min)	High Temperature Hold (°C, min)
Phenolic Resin	10	-	1500, 20
ZrB ₂ -B ₄ C-PR, ZrB ₂ -SiC-B ₄ C-PR-B-D-S, ZrO ₂ -B ₄ C	10	400, 60	1500, 20
ZrB ₂ -5-ZrSi ₂ , ZrB ₂ -10-ZrSi ₂ , ZrB ₂ -20-ZrSi ₂	14	-	1648, 20

For the phenolic resin, 0.004 g were placed on sintered alumina paper and heated as specified in Table 5.1. Dilatometer data were not acquired and no spacers were used because the sample was expected to fully decompose during the heating cycle.

To determine the composition of the gas phase, the background of m/z signal was subtracted from the peaks. The resulting signals were then normalized to the largest peak and compared to signals from known CO sources (the ZrB₂ samples) and CO₂ (CO₂ gas) sources, as well as to isotope abundances [21] of elements from suspected compounds. The signals were also compared to those of the individual compounds that comprise the composition of the sample, such as ZrB₂, B₄C, SiC, and ZrO₂. The dilatometer data were corrected for the length change of the spacers and smoothed using the data analysis software.

As was observed in Chapter 4, a common occurrence in the mass spectrometer data was the possible contribution of both CO and CO₂ to the m/z=12, 16, and 28 signals. A correction procedure is used in order to determine the CP of CO when signals also contained lesser amounts of CO₂, by removing the contribution of CO₂ from the m/z=12, 16, and 28 signals and then normalizing via:

$$N_y = (I_y - (I_{44} \times CP_y)) / I_{28} \quad 5.6$$

where N_y is the normalized intensity of y, for the y=m/z=12, 16, and 28 signals, I_y is the signal intensity (with baseline subtracted) of y, and CP_y is the cracking pattern of y out of 1.0 in CO₂. The normalized intensity for each signal is then attributed only to CO, which then allows the CP of CO to be determined.

5.3 Results

5.3.1 Phenolic Resin

The decomposition of phenolic resin, the structure of which is shown in Figure 5.1, was examined first by itself, as it is used in the ZrB₂-B₄C and ZrB₂-SiC-B₄C samples as the source for excess carbon. The signals of m/z=29, 43, 45, 91, 94, 106, and 108 from a pure phenolic resin sample heated at 10°C/min in flowing helium are plotted in Figure 5.2. The first peaks occur at t=50 min (T=410°C) for the m/z=43, 91, 94, 106 and 108 signals and then at t=69 min (T=600°C) for the m/z=29, 43, 45, 91, and 106 signals. Subsequent to their peaks at low temperature, the m/z=94 and 108 signals exhibit broad peaks of higher intensity for t>80 min (T>710°C) which are sustained until the end of the heating cycle. There are also peaks for the m/z=45 and 91 signals during the high temperature hold starting at t=159 min (T=1480°C). Based on the structure of the

phenolic resin, we can assign the decomposition products observed in Figure 5.2 to COH ($m/z=29$), C_6H_2OH ($m/z=91$), C_6H_5OH ($m/z=94$), OC_6H_2O ($m/z=106$), and OC_6H_4O ($m/z=108$), and tentatively assign the products of C_3H_7 ($m/z=43$) and C_2H_5O ($m/z=45$) from possible recombination reactions.

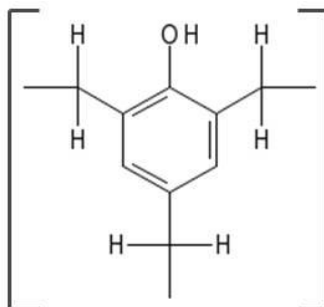


Figure 5.1: Phenol formaldehyde (phenolic resin) repeat structure of MW=133.

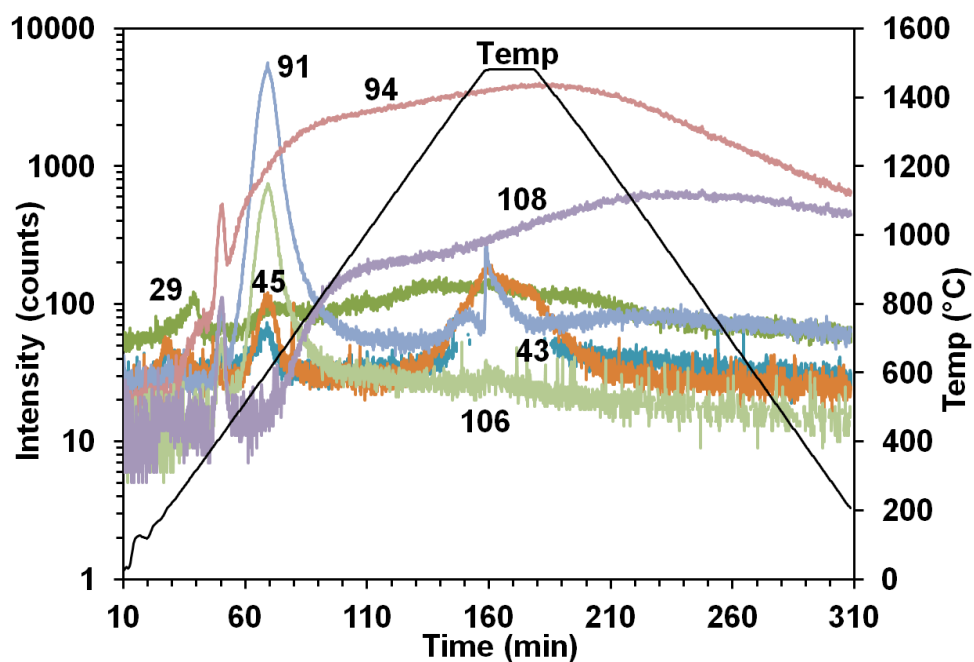


Figure 5.2: Temperature (Temp) and species intensity of the $m/z=29$, 43, 45, 91, 94, 106, and 108 signals versus time for 0.004 g of phenolic resin heated at $10^{\circ}\text{C}/\text{min}$ in flowing helium.

The $m/z=12$, 16, 28, 44, and 45 signals for the phenolic resin sample are plotted in Figure 5.3. The first low temperature peaks coincide with the peaks from Figure 5.2 at $t=69$ min ($T=600^{\circ}\text{C}$) for the $m/z=44$ and 45 signals. The next group of low temperature peaks are the $m/z=12$, 16, and 28 signals that occur at $t=72$ min ($T=630^{\circ}\text{C}$). The high temperature peaks during the hold starting at $t=159$ min ($T=1480^{\circ}\text{C}$) are observed for all of the signals in Figure 5.3. The CP of these signals at $t=159$ min (1480°C) are given in Table 5.2 and show good agreement for the CP of CO_2 gas at 1500°C , except for the $m/z=28$ signal. A possible reason for the larger $m/z=28$ signal (CO) in the CP of CO_2 from the phenolic resin sample can be explained by investigating the equilibrium reactions of carbon and oxygen:



Equation 5.8 has been shown to be dominant over Equation 5.7 at elevated temperatures ($T>500^{\circ}\text{C}$), resulting in a higher CO signal than CO_2 in the presence of excess carbon [22].

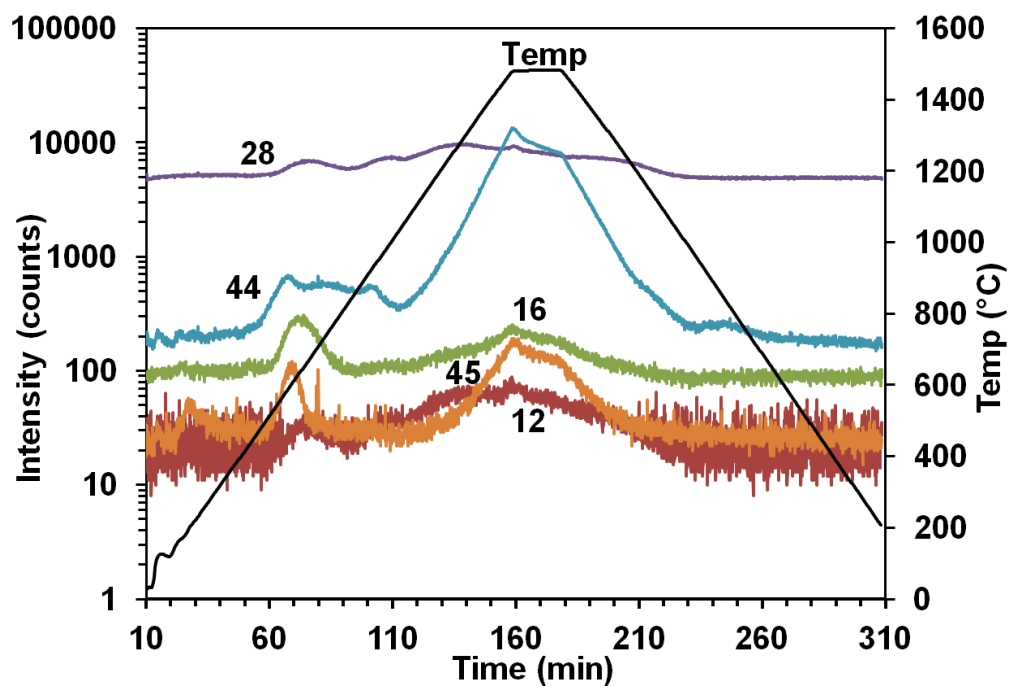


Figure 5.3: Temperature (Temp) and species intensity of the $m/z=12$, 16, 28, 44, and 45 signals versus time for 0.004 g of phenolic resin heated at $10^{\circ}\text{C}/\text{min}$ in flowing helium.

Table 5.2: Comparison of normalized m/z ratios evolved from phenolic resin, ZrO₂-B₄C, ZrB₂-B₄C-PR, ZrB₂-SiC-B₄C-PR-B-D-S, ZrB₂-5, -10, & -20-ZrSi₂, ZrB₂, B₄C and CO₂ gas, and the isotopes for CO₂ [21].

Source	Peak	Peak intensity at m/z ratios normalized to m/z = 28 or 44				
		12	16	28	44	45
Phenolic Resin	1480	0.5	1.1	34.7	100	1.2
ZrO ₂ -B ₄ C*	1290	3.5	3.8	100	-	-
ZrO ₂ -B ₄ C*	1460	5.1	5.6	100	-	-
ZrB ₂ -B ₄ C-PR*	1270	1.2	1.5	100	-	-
ZrB ₂ -B ₄ C-PR	1370	-	-	-	100	1.3
ZrB ₂ -B ₄ C-PR	1480	-	-	-	100	1.2
ZrB ₂ -SiC-B ₄ C-PR-B-D-S*	1335	1.2	1.5	100	-	-
ZrB ₂ -5-ZrSi ₂ *	1150	1.7	2.0	100	-	-
ZrB ₂ -5-ZrSi ₂	1570	1.5	1.4	100	-	-
ZrB ₂ -10-ZrSi ₂ *	1110	1.4	1.5	100	-	-
ZrB ₂ -10-ZrSi ₂	1595	1.5	1.5	100	-	-
ZrB ₂ -20-ZrSi ₂	1040	1.0	1.9	100	-	-
ZrB ₂ -20-ZrSi ₂	1590	2.1	2.3	100	-	-
ZrB ₂ *	1190	0.9	1.1	100	-	-
ZrB ₂ *	1360	0.9	1.1	100	-	-
B ₄ C*	1390	1.1	1.3	100	-	-
CO ₂ gas	1500	0.3	1.3	3.2	100	1.2
Isotopes for CO ₂		-	-	-	100	1.1
Possible Compounds		¹² C	¹⁶ O	¹² C ¹⁶ O	¹² C ¹⁶ O ₂	¹³ C ¹⁶ O ₂

*Correction procedure used

5.3.2 ZrO₂-B₄C

The m/z=12, 16, 28, 44, and 45 signals, sample length, and temperature are plotted versus time in Figure 5.4 for 0.8 g of pressed ZrO₂-B₄C heated at 10°C/min in helium. The sample experienced a 19.9% mass loss and a linear shrinkage of 3.0% from a starting relative theoretical density of 0.56 for the mixture. The lower temperature peaks at t=58 min (T=330°C), t=134 min (T=490°C), and t=145 min (T=600°C) correspond to the species evolved from the boron nitride spray used on the ends of the sample. These

signals can thus be assigned as in Chapter 4 to one or more of the following organics: acetone, ethanol, propane, or n-butane. The onset of the major decrease in length occurs at $t=199$ min ($T=1140^{\circ}\text{C}$), immediately after the beginning of the high temperature peaks.

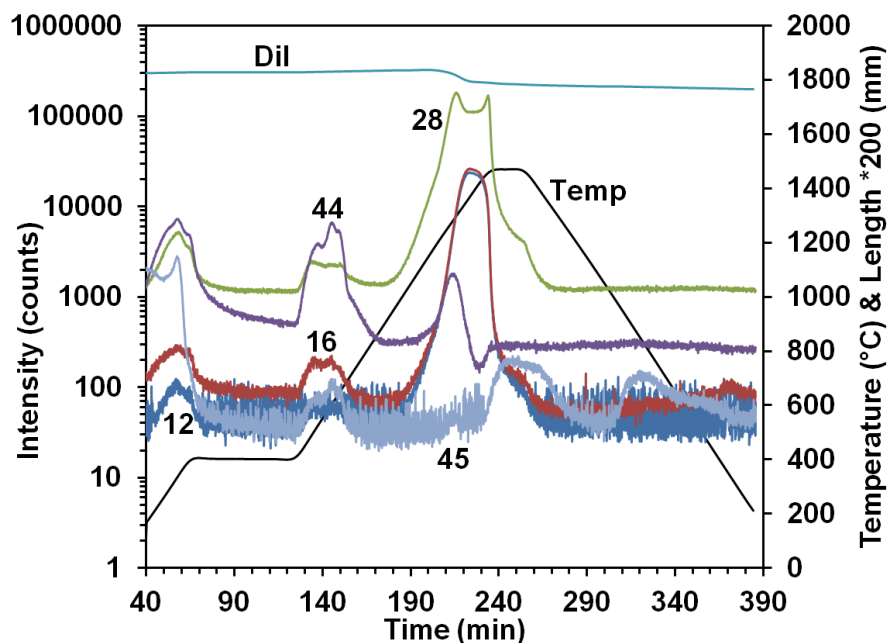


Figure 5.4: Temperature (Temp), length change (Dil), and species intensity of the $m/z=12$, 16, 28, 44, and 45 signals versus time for 0.8 g of $\text{ZrO}_2\text{-B}_4\text{C}$ heated at $10^{\circ}\text{C}/\text{min}$ in flowing helium.

The high temperature peaks occur over a time range of 19 min leading into the high temperature soak and include the $m/z=12$, 16, 28, 44, and 45 signals. The first peaks occur at $t=215$ min (1290°C) from the $m/z=28$ and 44 signals. Accompanying these peaks are increases in the $m/z=12$ and 16 signals that later peak at $t=224$ min (1370°C). An initial assignment of the $m/z=28$ peak to CO and of the $m/z=44$ peak to CO_2 , with CO being the major signal, is based on the results from the individual powders reported in

Chapter 4. In Table 5.2, the intensities of the $m/z=12$ and 16 signals have been normalized to the $m/z=28$ signal at 1290°C according to Equation 5.6. The $m/z=12$ and 16 signals in the CP are approximately three times larger than what has been observed for the CP of CO in individual powders and in powder mixtures.

Two other signals, the $m/z=29$ and 30 signals (not shown), have peaks that occur at the same time ($t=215$ min) as the peak in the $m/z=28$ signal. The comparison of the isotope ratios of carbon and oxygen to the $m/z=29$ and 30 signals in Table 5.3 show agreement between the isotope ratios and their suspected intensity ratios. This, along with the C ($m/z=12$) and O ($m/z=16$) signals in the CP of CO and the fact that no other peaks occur at this time, provide substantial evidence that CO is the evolved species. The lack of agreement to the pure component CPs may arise due to matrix effects in the mass spectrometer, which are changes in the ionization efficiency due to the presence of multiple substances.

Table 5.3: Comparison of normalized m/z ratios evolved from ZrO_2-B_4C and the isotopes for CO [21].

Source	Peak	Peak intensity at m/z ratios normalized to $m/z = 28$		
		28	29	30
$ZrO_2-B_4C^*$	1290	100	1.5	0.3
$ZrO_2-B_4C^*$	1460	100	1.5	0.3
Isotopes for CO		100	1.1	0.2
Possible Compounds		$^{12}C^{16}O$	$^{13}C^{16}O$	$^{12}C^{18}O$

*Correction procedure used

The second peak of the $m/z=28$ signal occurs at $t=234$ min (1460°C) along with a peak of the $m/z=45$ signal that extends into the high temperature hold. As with the first

$m/z=28$ signal peak, the $m/z=12$ and 16 signals are normalized to the $m/z=28$ signal peak in Table 5.2 via Equation 5.6. The observed CP is approximately four times larger than the CP seen from other powder mixtures and individual powders; once again matrix effects may be operative here. The comparison of isotope ratios for CO compared with the $m/z=28$, 29 , and 30 signals in Table 5.3 are consistent with the first $m/z=28$ peak, thus once again indicating that CO is evolved.

The assignment of CO to these high temperature peaks, typified by the $m/z=28$ signal, is supported by the known chemistry between ZrO_2 and B_4C at high temperature. As summarized by Equation 5.1, the reduction of ZrO_2 by B_4C results in ZrB_2 , B_2O_3 , and CO products. Signals from B_2O_3 were not observed, as was the case for the ZrB_2 - B_4C -PR and ZrB_2 -SiC- B_4C -PR-B-D-S samples. The weight loss reported in Goldstein et al. [23] for a ZrO_2 - B_4C composition sample began as low as 1150°C , but the majority occurred 1200 - 1450°C , which coincides with the CO and CO_2 peaks observed from the ZrO_2 - B_4C sample herein.

Figure 5.4 also shows peaks for the $m/z=45$ signal at $t=242$ min ($T=1470^\circ\text{C}$) during the high temperature soak and at $t=320$ min ($T=780^\circ\text{C}$) during the cooling section of the temperature profile. These signals are not coupled with the $m/z=44$ signal associated with the evolution of CO_2 , nor are there any of the signals observed from the boron nitride spray, such as the $m/z=45$ signal seen at very early times, with these peaks. While it is not uncommon to see signal peaks during the high temperature soak, it is uncommon to see signal peaks during cooling. No assignment is made using current information for these two $m/z=45$ signal peaks.

5.3.3 ZrB₂-B₄C-PR

In Figure 5.5, the signals for $m/z=12$, 16, 28, 44, and 45, sample length, and temperature are plotted versus time for the 0.5 g of pressed ZrB₂-B₄C-PR sample heated at 10°C/min in helium. The sample experienced a decrease in mass of 4% and in length of less than 1%, but there was no measurable change in the relative density. At $t=31$ min ($T=345^\circ\text{C}$), the intensities of the $m/z=16$, 28, 44, and 45 signal peaks are consistent with those arising from the organics in the boron nitride spray.

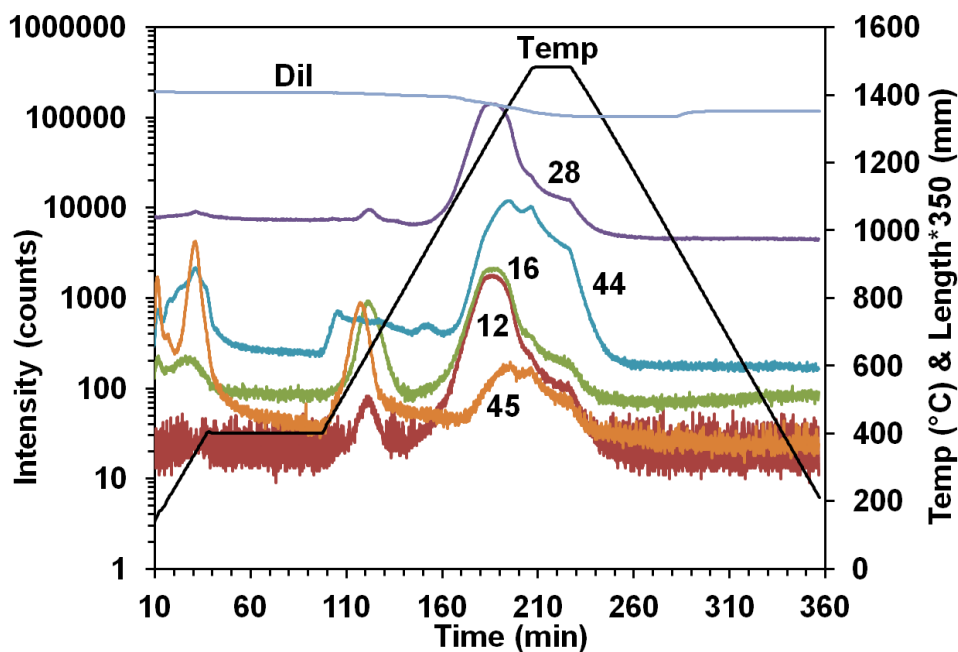


Figure 5.5: Temperature (Temp), length change (Dil), and species intensity of the $m/z=12$, 16, 28, 44, and 45 signals versus time for 0.5 g of ZrB₂-B₄C-PR heated at 10°C/min in flowing helium.

At $t=117$ min ($T=600^\circ\text{C}$) in Figure 5.5, there is a peak for the $m/z=45$ signal and corresponding peaks in Figure 5.6 for the $m/z=29$, 31, 43, 91, 106, and 108 signals at the

same temperature. An examination of the signals for the boron nitride spray from Chapter 4 in Figure 4.2 shows peaks for the same signals that occur at a temperature lower than 600°C, with the $m/z=91$, 106, and 108 signals at a much lower intensity. The boron nitride spray is contributing to these signals, but this assignment does not explain all of the signals observed. Phenolic resin is also present in the $\text{ZrB}_2\text{-B}_4\text{C-PR}$ sample as a source of excess carbon, and the same signals from a pure phenolic resin sample occur at the same temperature as for the $\text{ZrB}_2\text{-B}_4\text{C-PR}$ sample.

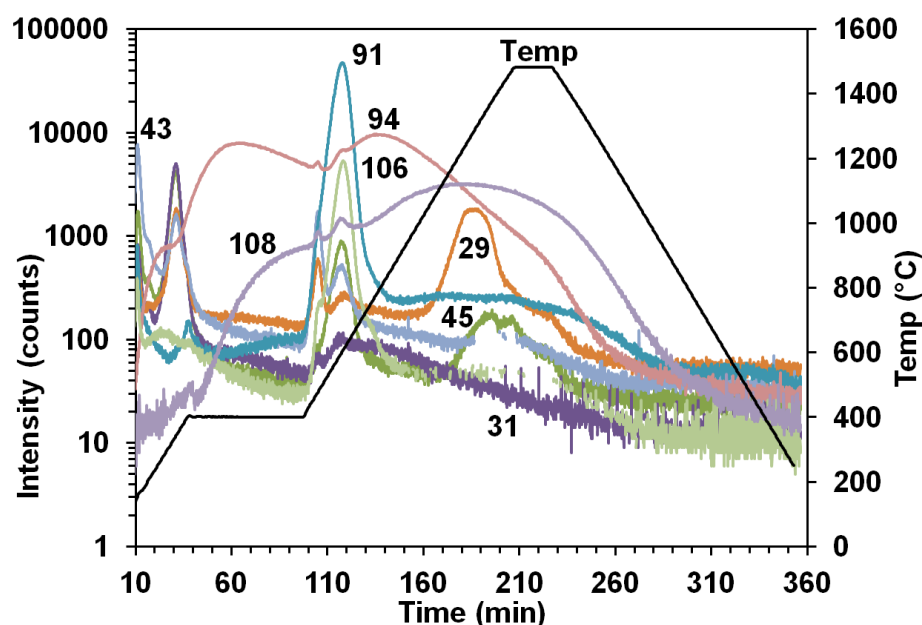


Figure 5.6: Temperature (Temp) and species intensity of the $m/z=29$, 31, 43, 45, 91, 94, 106, and 108 signals versus time for 0.5 g of $\text{ZrB}_2\text{-B}_4\text{C-PR}$ heated at 10°C/min in flowing helium.

In Figure 5.5 at $t=121$ min ($T=635^\circ\text{C}$), peaks occur in the $m/z=12$, 16, and 28 signals, which suggests that CO ($m/z=28$) is being evolved. An examination of the $m/z=12$, 16, and 28 signals of the phenolic resin sample in Figure 5.3 also shows peaks

for these signals at $t=72$ min ($T=630^{\circ}\text{C}$). This allows us to assign the source of the $m/z=12$, 16, and 28 signal peaks at $t=121$ min to phenolic resin. The evolution of boron nitride spray components and the decomposition of phenolic resin are the dominant peaks below 650°C in the $\text{ZrB}_2\text{-B}_4\text{C-PR}$ sample.

The largest decrease in length for the $\text{ZrB}_2\text{-B}_4\text{C-PR}$ sample begins at $t=166$ min ($T=1080^{\circ}\text{C}$) and coincides with the beginning of large peaks for the $m/z=12$, 16, and 28 signals at $t=185$ min ($T=1270^{\circ}\text{C}$) and for the $m/z=44$ and 45 signals at $t=195$ min ($T=1370^{\circ}\text{C}$) and $t=207$ min ($T=1480^{\circ}\text{C}$), as seen in Figure 5.5. The peaks for the $m/z=12$, 16, 28, 44, and 45 signals all decrease throughout the high temperature hold and have a shoulder feature when cooling begins.

The correction procedure in Equation 5.6 was applied to the peak intensities of the $m/z=12$, 16, and 28 signals for $\text{ZrB}_2\text{-B}_4\text{C-PR}$ at 1270°C and for the individual powders of ZrB_2 and B_4C at temperatures between 1190°C and 1390°C in Table 5.2. An examination of these values shows that the $m/z=12$ and 16 signals of $\text{ZrB}_2\text{-B}_4\text{C-PR}$ are slightly larger than the individual powders values but are still reasonably close as to what was observed and thus the assignment to CO can still be justified for these peaks.

For the two peaks of the $m/z=44$ and 45 signals seen at $t=195$ min ($T=1370^{\circ}\text{C}$) and $t=207$ min ($T=1480^{\circ}\text{C}$) in Figure 5.5, a comparison of the normalized peak intensities to the CP of CO_2 gas and to the isotopes for CO_2 in Table 5.2 confirm the assignment to CO_2 . The analysis method of subtracting the $m/z=12$, 16, and 28 signal contributions of the CO_2 CP from the rest of the signals has shown that the contribution from the CO_2 is minimal, due to the large CO intensity at the same m/z signals. A possible source for the CO_2 can be attributed to the phenolic resin, as seen in Figure 5.3.

The source of the CO can be linked to both the impurities in the individual powders from processing techniques, as was seen in Chapter 4, and to the reactions between the powder components. The surface oxide of ZrB_2 in the form of ZrO_2 can react with the B_4C as given by Equations 5.1, 5.4, and 5.5. These reactions have been shown to increase removal of surface oxides and thereby increase densification [6, 13]. This sintering is observed in the ZrB_2 - B_4C -PR sample by the slight decrease in length over the same time period, $t=166$ to 226 min, that CO evolution occurs. Another possible source of carbon contamination is the WC milling media.

Based on Equation 5.1, B_2O_3 is a product of the reaction between the surface oxide ZrO_2 and B_4C in the ZrB_2 - B_4C -PR sample, and because the sample was heated past the temperature required for the reaction to occur and near the boiling temperature (1500°C) of B_2O_3 [24], it is expected to observe signals related to B_2O_3 . The $m/z=27$ (BO), 53 (B_2O_2), and 69 (B_2O_3) signals (not shown here) from the CP of B_2O_3 were observed at temperatures up to 500°C , well below the temperature of 1220°C necessary for the reaction in Equation 5.1. The same signals, however, are consistent with the signals seen from the boron nitride spray (see Chapter 4) and are thus not assigned to B_2O_3 . As discussed in Chapter 4, the reason for not observing the B_2O_3 signals at $T>1220^\circ\text{C}$ is most likely due to the low temperature of the capillary interface between the furnace and mass spectrometer, resulting in condensation of the vapor.

5.3.4 ZrB_2 -SiC- B_4C -PR-B-D-S

The 0.5 g pressed ZrB_2 -SiC- B_4C -PR-B-D-S sample was heated at $10^\circ\text{C}/\text{min}$ in helium, and Figure 5.7 shows the $m/z=12$, 16, 28, 44, and 45 signals, sample length, and

temperature versus time. The sample underwent a length decrease of <1% and a loss of 4.4% mass, and there was no increase in relative final density. At $t=24$ min ($T=275^{\circ}\text{C}$), $t=32$ min ($T=350^{\circ}\text{C}$), $t=106$ min ($T=490^{\circ}\text{C}$), and $t=120$ min ($T=625^{\circ}\text{C}$), all of the five signals mentioned above have features, which correspond to similar signals that were observed in the $\text{ZrB}_2\text{-B}_4\text{C-PR}$ heating cycle below 660°C . Figure 5.8 shows the $m/z=29$, 31, 43, 45, 91, 94, 106, and 108 signals that also have features at the times previously mentioned for the $\text{ZrB}_2\text{-SiC-B}_4\text{C-PR-B-D-S}$ sample. Using the same comparative analysis technique as before, the assignment of these lower temperature peaks can be made to mostly carbon-containing species evolved from the boron nitride spray and the phenolic resin, in addition to the organic content arising from the binder, dispersant, and surfactant.

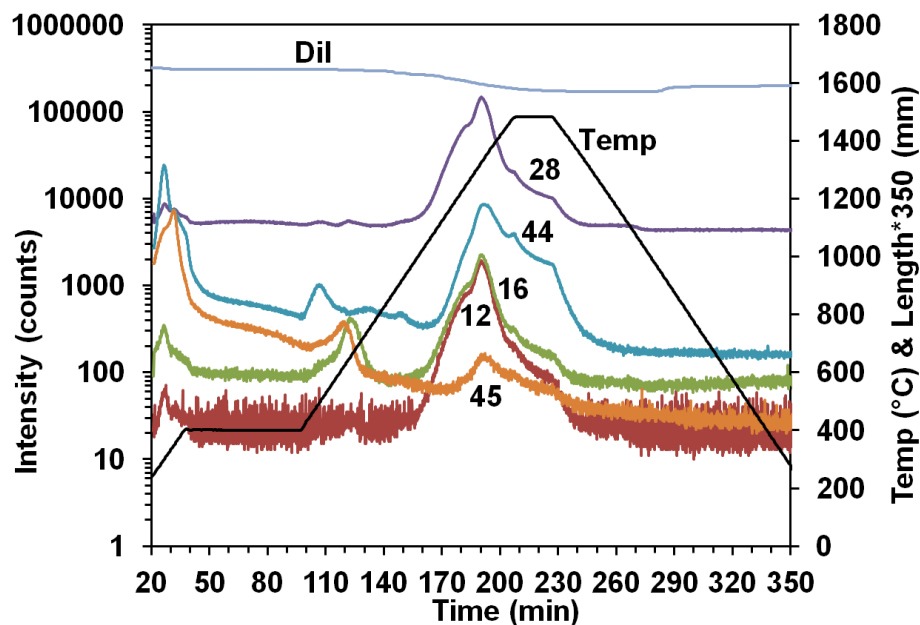


Figure 5.7: Temperature (Temp), length change (Dil), and species intensity of the $m/z=12$, 16, 28, 44, and 45 signals versus time for 0.5 g of $\text{ZrB}_2\text{-SiC-B}_4\text{C-PR-B-D-S}$ heated at 10°C/min in flowing helium.

Figure 5.7 also shows for the $\text{ZrB}_2\text{-SiC-B}_4\text{C-PR-B-D-S}$ sample peaks for the $m/z=12, 16, 28, 44,$ and 45 signals at $t=191$ min ($T=1335^\circ\text{C}$) along with two shoulder features prominent in the $m/z=28$ and 44 signals at the beginning and end of the high temperature soak. These signals begin to increase around $t=160$ min ($T=1015^\circ\text{C}$), which is the same time at which the length of the sample begins to decrease. The correction procedure from Equation 5.6 was used for the $\text{ZrB}_2\text{-SiC-B}_4\text{C-PR-B-D-S}$ sample peaks and the CP in Table 5.2 shows good agreement for the $m/z=12, 16,$ and 28 signals as compared to the $\text{ZrB}_2\text{-B}_4\text{C-PR}$ signals at 1270°C , which again indicates CO evolution.

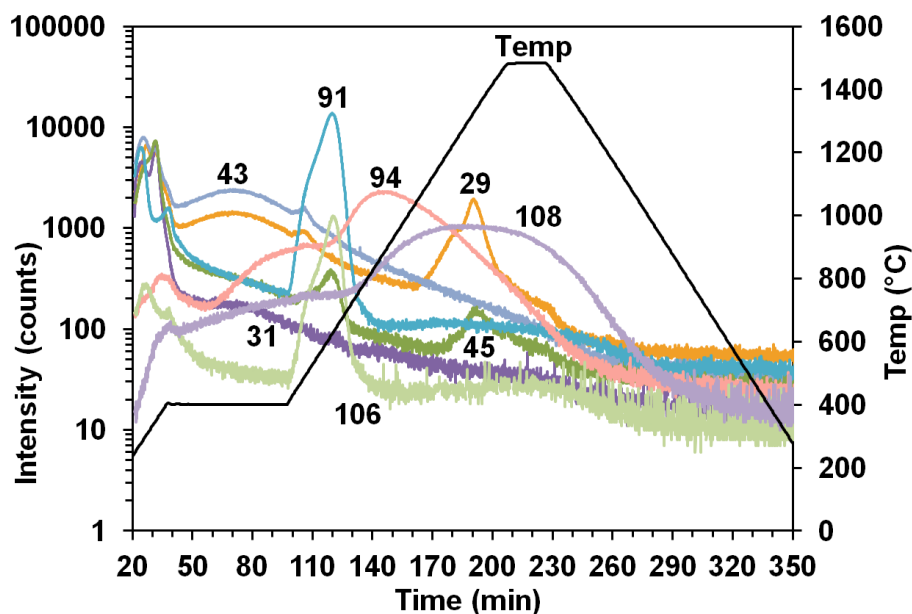


Figure 5.8: Temperature (Temp) and species intensity of the $m/z=29, 31, 43, 45, 91, 94,$ $106,$ and 108 signals versus time for 0.5 g of $\text{ZrB}_2\text{-SiC-B}_4\text{C-PR-B-D-S}$ heated at 10°C/min in flowing helium.

In the $\text{ZrB}_2\text{-SiC-B}_4\text{C-PR-B-D-S}$ sample, the $m/z=44$ and 45 peak signals in Figure 5.7 are present at the same temperature as the CO peak evolution, which is unlike

what was observed for the ZrB₂-B₄C-PR sample. By normalizing the m/z=45 signal to the m/z=44 signal as seen in Table 5.2, the ratio is in fair agreement to the CP observed for the ZrB₂-B₄C-PR sample at 1370°C and 1480°C and for the CP of CO₂ gas at 1500°C. The larger m/z=44 and 45 signals in the ZrB₂-SiC-B₄C-PR-B-D-S sample at t=191 min (T=1335°C) can be attributed to the decomposition of the phenolic resin in the sample into CO₂, as was seen for the ZrB₂-B₄C-PR sample.

The high temperature CO and CO₂ sources for the ZrB₂-SiC-B₄C-PR-B-D-S sample are likely the same as from the ZrB₂-B₄C-PR sample (Equations 5.1, 5.4, and 5.5), namely, the reduction of surface oxides from a carbonaceous source, such as those found as impurities in the individual powders. The SiO₂ oxide layer present on the surface of SiC can lead to production of CO by reacting with SiC at low oxygen partial pressure (30 Pa) and elevated temperatures (T>1400°C) [15] via:



Under these same conditions, any oxygen that is present can oxidize the SiC and produce CO, as seen in Equation 5.3.

A product in both Equation 5.3 and 5.9 is SiO gas, which would have signals of SiO (m/z=44), Si (m/z=28), O (m/z=16) and ²⁹SiO (m/z=45); these are many of the primary signals in the CPs of CO and CO₂. The assignment of CO and CO₂ for the signal peaks in Figure 5.7 is further substantiated by the similar CP value for the ¹³CO₂ (m/z=45) isotope compared to the ZrB₂-B₄C-PR and ZrB₂-SiC-B₄C-PR-B-D-S samples in Table 5.2. The sample values are much closer to the ¹³CO₂ isotope abundance than what is expected for the ²⁹SiO isotope abundance for ²⁹Si of 4.7% [21]. The presence of

the C ($m/z=12$) signal would also confirm the assignment of CO_2 over SiO except that the $m/z=12$ signal contribution from CO is also present.

At high temperatures ($T>1520^\circ\text{C}$) [25], excess carbon can reduce the surface oxides on silicon carbide via:



Silica can also dissociate at high temperatures ($T>1710^\circ\text{C}$) [26], providing another source of oxygen that can potentially combine with excess carbon to form CO and CO_2 :



It is unlikely; however, that the reactions from Equations 5.10 and 5.11 occurred in the $\text{ZrB}_2\text{-SiC-B}_4\text{C-PR-B-D-S}$ sample since the maximum temperature was 1500°C . As in the $\text{ZrB}_2\text{-B}_4\text{C-PR}$ sample, none of the signals from the CP of B_2O_3 were observed.

5.3.5 $\text{ZrB}_2\text{-5-ZrSi}_2$

A pressed $\text{ZrB}_2\text{-5-ZrSi}_2$ sample was heated at 14°C/min to 1648°C in flowing helium, and experienced an overall decrease of 4.5% in mass and of 8.2% in length, resulting in a relative theoretical density increase from 0.54 to 0.70. The relative final density is comparable to the extrapolated relative final density according to the results of Guo et al. [10] that are plotted as relative density versus volume percent of ZrSi_2 . The temperature, length, and $m/z=12$, 16, 28, 44, and 45 signals are plotted versus time for the $\text{ZrB}_2\text{-5-ZrSi}_2$ sample in Figure 5.9. The $t=25$ min ($T=360^\circ\text{C}$) peaks for the $m/z=12$, 16, 28, 44, and 45 signals along with a peak at $t=40$ min ($T=570^\circ\text{C}$) for the $m/z=45$ signal are consistent with what has been observed below 660°C when using the boron nitride spray and are therefore attributed to this source.

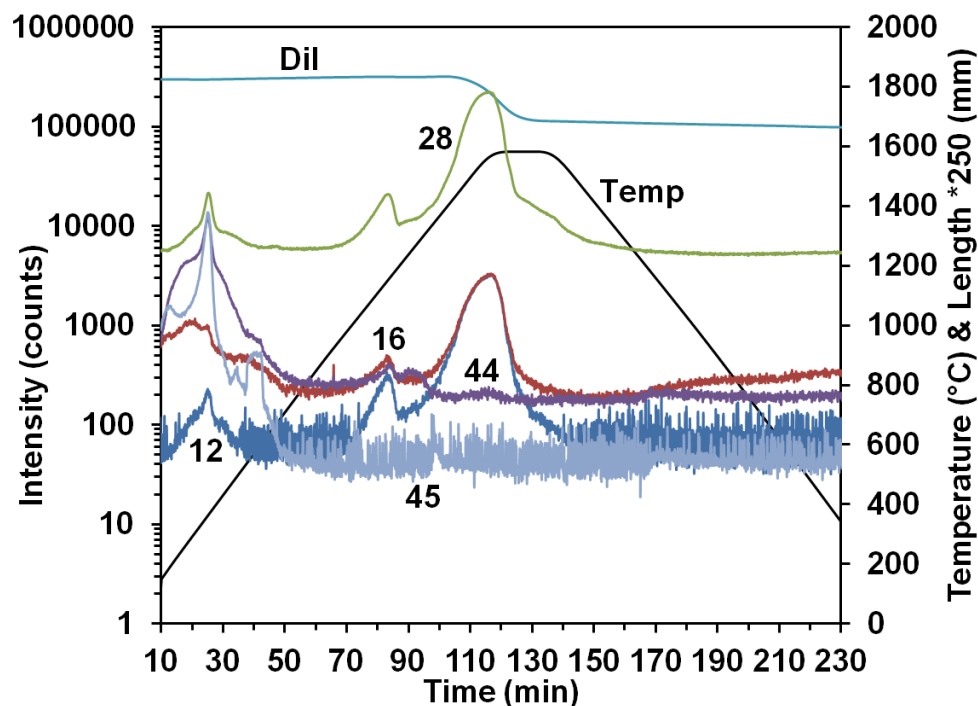


Figure 5.9: Temperature (Temp), length change (Dil), and species intensity of the $m/z=12, 16, 28, 44$, and 45 signals versus time for 0.8 g of $\text{ZrB}_2\text{-5-ZrSi}_2$ heated at 14°C/min in flowing helium.

At $t=83$ min ($T=1150^\circ\text{C}$) in Figure 5.9, peaks arise in signals for the $m/z=12, 16, 28$, and 44 , and these peaks occur before the sample experiences a decrease in length. This family of signals is again suggestive of CO and CO_2 ; to verify this, the correction procedure of Equation 5.6 was used to determine the CP of CO . Table 5.2 shows that corrected CP is in comparatively good agreement with the corrected CPs observed for the other samples containing ZrB_2 , although these were observed at $100\text{-}200^\circ\text{C}$ higher temperatures. The peak temperature observed here for the evolution of CO and CO_2 is near to the same temperature observed for the evolution of CO and CO_2 from ZrB_2 (see Chapter 4).

At $T=1150^{\circ}\text{C}$ in Figure 5.9, an $m/z=45$ peak is expected from the isotope of carbon in CO_2 to match with the $m/z=44$ signal, but this peak is not discernible from the baseline for the $m/z=45$ signal. The assignment to CO_2 for the $m/z=44$ signal is based, however, on the same reasoning for the ZrB_2 powder at 1190°C and the $\text{ZrB}_2\text{-SiC-B}_4\text{C-PR-B-D-S}$ powder at 1335°C , where the evolution of CO and a small amount of CO_2 is present. Another small peak of the $m/z=44$ signal is observed at $t=90$ min ($T=1235^{\circ}\text{C}$) for the $\text{ZrB}_2\text{-5-ZrSi}_2$ sample in Figure 5.9; however, there are no other distinguishable peaks for other species at this time.

The onset of the length decrease in the sample occurs at $t=101$ min ($T=1385^{\circ}\text{C}$), seen in Figure 5.9, which coincides with the beginning of large peaks from the $m/z=12$, 16, and 28 signals that occur at $t=117$ min ($T=1570^{\circ}\text{C}$). The CP of these signals, normalized to the $m/z=28$ signal and seen in Table 5.2, match with what has been observed in the $\text{ZrB}_2\text{-B}_4\text{C-PR}$ sample at 1270°C and the $\text{ZrB}_2\text{-SiC-B}_4\text{C-PR-B-D-S}$ sample at 1335°C . The assignment of this peak to CO evolution during the length decrease of the sample can therefore be made.

The sources of the CO and CO_2 can be determined in part by investigating the synthesis routes for both the ZrB_2 and the ZrSi_2 . The synthesis of ZrB_2 , which has already been discussed and outlined in Equations 5.1, 5.4, and 5.5, gives rise to surface oxides whose removal via carbon reduction leads to CO and CO_2 . The synthesis of ZrSi_2 is carried out in an electric furnace by the carbon thermal reduction of mixtures of ZrO_2 and SiO_2 [27]. This synthesis route is thus a possible source for carbon contamination. Oxygen contamination can be found on the oxide layers for each of the powders in the forms of ZrO_2 and SiO_2 for ZrB_2 and ZrSi_2 , respectively [10].

5.3.6 ZrB₂-10-ZrSi₂

A pressed ZrB₂-10-ZrSi₂ sample was heated at 14°C/min to 1648°C in flowing helium, and experienced an overall decrease in length of 12.8% and 5.7% in mass, resulting in a relative theoretical density increase from 0.53 to 0.74. The final relative theoretical density is 4 percentage points less than what was reported in Guo et al. [10]. The temperature, sample length, and m/z=12, 16, 28, 44, and 45 signals plotted for the ZrB₂-10-ZrSi₂ sample versus time are shown in Figure 5.10. The first set of peaks for the m/z=12, 16, 28, 44, and 45 signals at t=35 min (T=360°C) and the second peak for the m/z=45 signal at t=51 min (T=570°C) are consistent with the ZrB₂-5-ZrSi₂ sample and are therefore attributed to the boron nitride spray used on the samples.

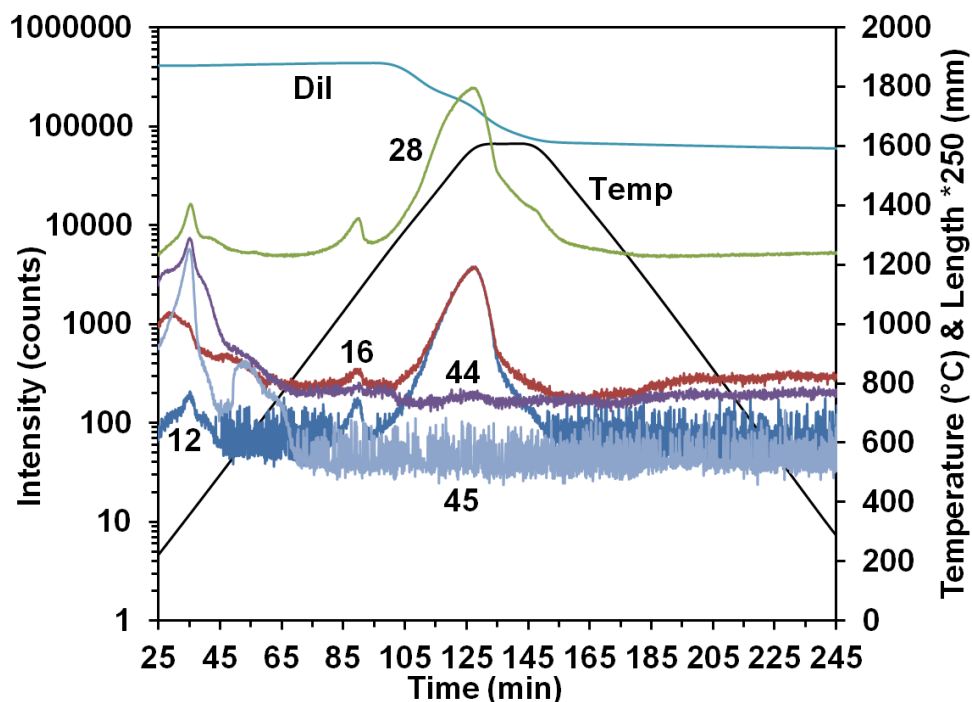


Figure 5.10: Temperature (Temp), length change (Dil), and species intensity of the m/z=12, 16, 28, 44, and 45 signals versus time for 0.8 g of ZrB₂-10-ZrSi₂ heated at 14°C/min in flowing helium.

In Figure 5.10 peaks arise in signals for the $m/z=12$, 16, 28, and 44 at $t=90$ min ($T=1110^{\circ}\text{C}$) and for the $m/z=12$, 16, and 28 signals at $t=128$ min ($T=1595^{\circ}\text{C}$). These families of signals suggest again the presence of CO and CO_2 ; the correction procedure described in Equation 5.6 is used to verify this. Table 5.2 shows that the corrected CP is in very good agreement with the corrected CPs observed for the ZrB_2 -5- ZrSi_2 sample. The peak temperature observed here for CO and CO_2 evolution is close to the same temperatures observed for CO and CO_2 evolution for the ZrB_2 -5- ZrSi_2 sample and the ZrB_2 sample (see Chapter 4).

The peak at $T=1110^{\circ}\text{C}$ for the CO signal has a lower overall intensity than the corresponding peak in the 5% ZrSi_2 sample. This could be attributed to a decrease in either surface oxides or leftover synthesis contamination from the ZrB_2 powder. The sources for the CO and CO_2 evolution in the ZrB_2 -10- ZrSi_2 sample are assumed to be the same as in the ZrB_2 -5- ZrSi_2 sample. It is noted that the additional 5 vol% of ZrSi_2 in this sample over the ZrB_2 -5- ZrSi_2 sample lowered the temperature for the start of the length decrease in the sample from 1385°C to 1210°C .

5.3.7 ZrB_2 -20- ZrSi_2

A pressed ZrB_2 -20- ZrSi_2 sample was heated at $14^{\circ}\text{C}/\text{min}$ to 1648°C in flowing helium, and experienced an overall mass decrease of 7.4% and of 15.5% in length, resulting in a relative theoretical density increase from 0.52 to 0.78. The final relative theoretical density was 9 percentage points less than what was reported in Guo et al. [10] (87%) versus a hold time of 60 min. Figure 5.11 shows the temperature, length of the sample, and $m/z=12$, 16, 28, 44, and 45 signals versus time. The peaks of the $m/z=12$, 16,

28, 44, and 45 signals at $t=36$ min ($T=355^{\circ}\text{C}$) are consistent as what was observed in the $\text{ZrB}_2\text{-5-ZrSi}_2$ and $\text{ZrB}_2\text{-10-ZrSi}_2$ samples and are therefore assigned to the boron nitride spray.

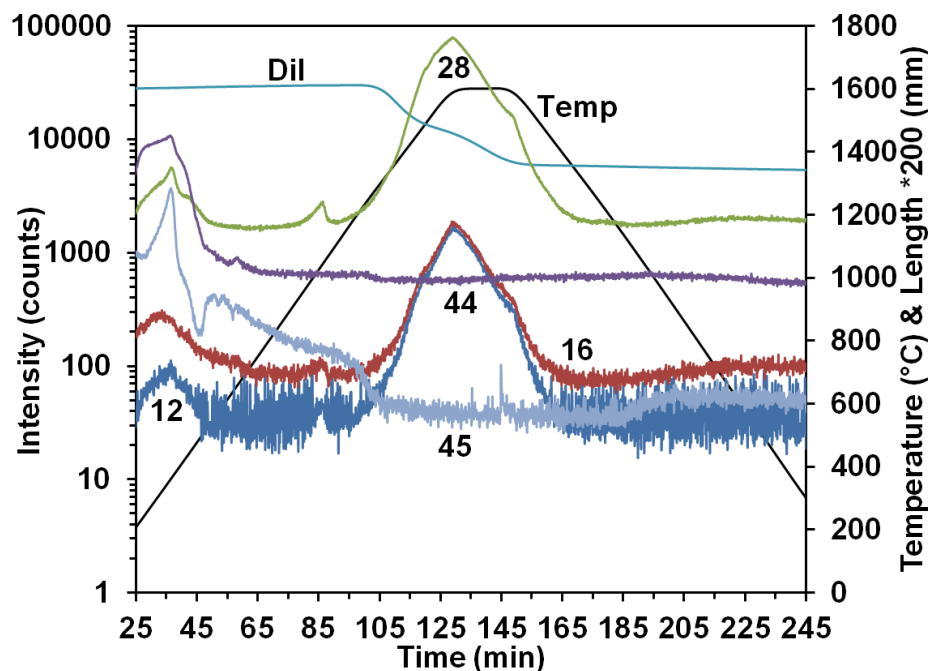


Figure 5.11: Temperature (Temp), length change (Dil), and species intensity of the $m/z=12, 16, 28, 44$, and 45 signals versus time for 0.8 g of $\text{ZrB}_2\text{-20-ZrSi}_2$ heated at 14°C/min in flowing helium.

At $t=86$ min ($T=1040^{\circ}\text{C}$) and $t=129$ min ($T=1590^{\circ}\text{C}$) in Figure 5.11, peaks arise in the $m/z=12, 16$, and 28 signals at similar temperatures to the $\text{ZrB}_2\text{-5-ZrSi}_2$ and $\text{ZrB}_2\text{-10-ZrSi}_2$ samples and this family of signals is again suggestive of CO. In order to verify this assignment, Table 5.2 shows that the CP of CO for the $\text{ZrB}_2\text{-20-ZrSi}_2$ sample is in comparatively good agreement with the $\text{ZrB}_2\text{-5-ZrSi}_2$, $\text{ZrB}_2\text{-10-ZrSi}_2$, and other ZrB_2 containing samples at similar temperatures.

The source for the CO is expected to be the same as the ZrB₂-5-ZrSi₂ and ZrB₂-10-ZrSi₂ samples. At T=1590°C, the main CO peak has a lower overall intensity than the corresponding peaks in the ZrB₂-5-ZrSi₂ and ZrB₂-10-ZrSi₂ samples. This can be attributed to a decrease in either surface oxide from the ZrB₂ or ZrSi₂ powder or leftover synthesis contamination from the ZrB₂ powder. The onset of the length decrease in the ZrB₂-20-ZrSi₂ sample occurs at t=102 min (T=1255°C) and is between the temperatures for the onset of length decrease for the ZrB₂-5-ZrSi₂ and ZrB₂-10-ZrSi₂ samples.

Table 5.4 compares the major CO (m/z=28) signal onset and peak temperatures, the onset of length change temperatures, and the final relative densities of the ZrB₂-5-ZrSi₂, ZrB₂-10-ZrSi₂, and ZrB₂-20-ZrSi₂ samples. The onset temperature of the CO signal decreases a total of 155°C as the proportion of ZrSi₂ increases from 5 vol% to 20 vol% in the samples. This suggests that one or more mechanisms are occurring: impurities from the ZrSi₂ powder are reacting to form CO more easily than the impurities from the ZrB₂ powder, the impurities from the ZrSi₂ powder are facilitating CO production by the impurities in the ZrB₂ powder at a lower temperature, or some other unknown mechanism is occurring.

Table 5.4: Temperatures of the major m/z=28 signal onset and peak and the onset of the sample length change, along with the final relative theoretical density for the ZrB₂-5-ZrSi₂, ZrB₂-10-ZrSi₂, and ZrB₂-20-ZrSi₂ samples.

Sample	Temperature (°C) of the major m/z=28 signal		Temperature (°C) of the onset of length change	Final relative theoretical density
	Onset	Peak		
ZrB ₂ -5-ZrSi ₂	1280	1570	1385	0.70
ZrB ₂ -10-ZrSi ₂	1180	1595	1210	0.74
ZrB ₂ -20-ZrSi ₂	1125	1590	1255	0.78

The CO signal peak temperatures in Table 5.4 are all within 25°C of each other and no clear increasing or decreasing peak temperature pattern is present with increasing ZrSi₂ content. For all three samples, the onset of the major CO signal occurs before the onset of the length change, indicating that the removal of impurities in the powder occurs before sintering begins. This is also supported by the decrease in the onset of length change temperature from 5 to 10 vol% ZrSi₂ that coincides with the temperature decrease for the onset of the major CO signal. The increasing final relative density with increasing ZrSi₂ composition is expected due to the much lower melting temperature of ZrSi₂ compared to ZrB₂.

5.4 Discussion

The densification of ultra-high temperature materials has traditionally been to increase the defect concentration in the material by pressing during heating (hot pressing); however, the sizes and complex shapes desired are beyond the limits of hot pressing. Other methods that have been explored to achieve densification are the introduction of liquid phases and the removal of surface oxide layers, both of which are accomplished by incorporating additives. The progression of each of the last two methods listed can be monitored by the combined dilatometer mass spectrometer. The mass spectrometer has been shown to be very sensitive, allowing for the likely detection of gas phases that accompany liquid phases and gas phases that are produced by the removal of surface oxide layers.

The heating and sintering of ultra-high temperature materials was accomplished using a combined dilatometer mass spectrometer. These materials are complex systems

with multiple reactions occurring throughout the heating, and the short detection time of the mass spectrometer is useful for examining these materials. The combination of dilatometry with mass spectrometry allows for determining how the additives affect the rate of sintering and the chemistry during heating. The combined dilatometer mass spectrometer, coupled with microstructural analysis and material properties testing, would provide the information necessary to develop compositions and sintering procedures that meet desired ultra-high temperature material applications.

5.5 Conclusions

Pressed ZrB_2 samples with additives of B_4C , SiC , excess carbon, and ZrSi_2 were examined up to temperatures of 1648°C while real time evolved gas phase species and sample length data were acquired. As expected, sintering occurred for the ZrB_2 - ZrSi_2 samples, but not for the ZrB_2 with other additives. The assignment of gas phase species through tabulated cracking pattern and isotope analysis was supported by results from phenolic resin and boron nitride, and from the individual powders of ZrB_2 and B_4C from Chapter 4. Organic species from the boron nitride spray and phenolic resin dominated the low temperature chemistry, while CO and CO_2 evolution was prevalent at higher temperatures. Surface oxide layers, along with carbon and oxygen contaminants from the powder, reacting with the additives are assigned as the sources of the CO and CO_2 evolution.

5.6 References

1. W. G. Fahrenholtz, G. E. Hilmas, I. G. Talmy, J. A. Zaykoski, "Refractory Diborides of Zirconium and Hafnium," *J. Am. Ceram. Soc.*, **90** 1347-1364 (2007).
2. S. Zhu, W. G. Fahrenholtz, G. E. Hilmas, and S. C. Zhang, "Pressureless Sintering of Zirconium Diboride Using Boron Carbide and Carbon Additions," *J. Am. Ceram. Soc.*, **90** 3660-63 (2007).
3. H. Pastor, "Metallic Borides: Preparation of Solid Bodies. Sintering Methods and Properties of Solid Bodies," pp. 457-93 in *Boron and Refractory Borides*, Edited by V. I. Matkovich. Springer, New York, 1977.
4. A. K. Khanra and M. M. Godkhindi, "Effect of Ni Additives on Pressureless Sintering of SHS ZrB_2 ," *Adv. Appl. Ceram.*, **104** 273 (2005).
5. D. Sciti, F. Monteverde, S. Guicciardi, G. Pezzotti, and A. Bellosi, "Microstructure and Mechanical Properties of ZrB_2 - MoSi_2 Ceramic Composites Produced by Different Sintering Techniques," *Mater. Sci. Eng. A*, **A434** 303-9 (2006).
6. S. Zhu, W. G. Fahrenholtz, G. E. Hilmas, and S. C. Zhang, "Pressureless Sintering of Carbon-Coated Zirconium Diboride Powders," *Mater. Sci. Eng. A*, **A459** 167-71 (2007).
7. S. K. Mishra and L. C. Pathak, "Effect of Carbon and Titanium Carbide on Sintering Behaviour of Zirconium Diboride," *J. Alloys Compd.*, **465** 547-55 (2008).
8. S. C. Zhang, G. E. Hilmas, and W. G. Fahrenholtz, "Pressureless Sintering of ZrB_2 - SiC Ceramics," *J. Am. Ceram. Soc.*, **91** 26-32 (2008).
9. J. Zou, G. J. Zhang, Y. M. Kan and P. L. Wang, "Pressureless Densification of ZrB_2 - SiC Composites with Vanadium Carbide," *Scr. Mater.*, **59** 309-12 (2008).
10. S.-Q. Guo, Y. Kagawa, T. Nishimura, and H. Tanaka, "Pressureless Sintering and Physical Properties of ZrB_2 -Based Composites with ZrSi_2 Additive," *Scr. Mater.*, **58** 579-582 (2008).
11. X. G. Wang, W. M. Guo, and G. J. Zhang, "Pressureless Sintering Mechanism and Microstructure of ZrB_2 - SiC Ceramics Doped with Boron," *Scr. Mater.*, **61** 177-80 (2009).
12. F. Monteverde, S. Guicciardi, and A. Bellosi, "Advances in Microstructure and Mechanical Properties of Zirconium Diboride-Based Ceramics," *Mater. Sci. Eng.*, **A346**, 310-9 (2003).

13. S. C. Zhang, G. E. Hilmas, and W. G. Fahrenholtz, "Pressureless Densification of Zirconium Diboride with Boron Carbide Additions," *J. Am. Ceram. Soc.*, **89** 1544-50 (2006).
14. J. Drowart and G. DeMaria, pp. 16-23 in *Silicon Carbide, A High Temperature Semiconductor*, Edited by J. F. O'Connor and J. Smiltens, Pergamon Press, Inc., New York, 1960.
15. N. G. Wright, "Silicon Carbide"; pp. 524-546 in *Kirk-Othmer Encyclopedia of Chemical Technology*, John Wiley & Sons, 2006, <http://dx.doi.org/10.1002/0471238961.1909120904092201.a01.pub2>, (retrieved April 17, 2012).
16. P. Sarin, P. E. Driemeyer, R. P. Haggerty, D.-K. Kim, J. L. Bell, Z. D. Apostolov, W. M. Kriven, "In Situ Studies of Oxidation of ZrB_2 and ZrB_2 -SiC Composites at High Temperatures," *J. Eur. Cer. Soc.*, **30** 2375-86 (2010).
17. W. C. Tripp, H. H. Davis, and H. C. Graham, "Effect of an SiC Addition on the Oxidation of ZrB_2 ," *Ceram. Bull.*, **52** 612-6 (1973).
18. L. Kaufman, E. V. Clougherty, J. B. Berkowitz-Mattuck, "Oxidation Characteristics of Hafnium and Zirconium Diboride," *Trns. Met. Soc. AIME*, **239** 458-66 (1967).
19. E. A. Gulbransen and S. A. Jansson, "The High-Temperature Oxidation, Reduction, and Volatilization Reactions of Silicon and Silicon Carbide," *Oxid. Met.*, **4**, 181-201 (1972).
20. D. R. Lide, pp. 4-96 in *Handbook of Chemistry and Physics (87 ed.)*, CRC Press, Boca Raton, FL, 1998.
21. J. S. Coursey, D. J. Schwab, J. J. Tsai, and R. A. Dragoset, *Atomic Weights and Isotopic Compositions*, National Institute of Standards and Technology, <http://www.nist.gov/pml/data/comp.cfm>, (retrieved August 31, 2010).
22. K. Feng, S. J. Lombardo, "High-Temperature Reaction Networks in Graphite Furnaces," *J. Mat. Sci.*, **37** 2747-2753 (2002).
23. A. Goldstein, Y. Geffen, and A. Goldenberg, "Boron Carbide-Zirconium Boride *In Situ* Composites by the Reactive Pressureless Sintering of Boron Carbide-Zirconia Mixtures," *J. Am. Ceram. Soc.*, **84** 642-44 (2001).
24. P. Patnaik, p. 119 in *Handbook of Inorganic Chemical Compounds*, McGraw-Hill, 2003.

25. M. S. Datta, A. K. Bandyopadhyay, and B. Chaudhuri, "Sintering of Nano Crystalline α Silicon Carbide by Doping with Boron Carbide," *Bull. Mater. Sci.*, **25** 181-9 (2002).
26. D. W. Green and R. H. Perry, eds., pp. 3-49 in *Perry's Chemical Engineer's Handbook*, 6th ed., McGraw-Hill Book Co., Inc., New York, 1984.
27. V. Dosaj, M. Kroupa, and R. Bittar, "Silicon and Silicon Alloys, Chemical and Metallurgical"; pp. 1-25 in *Kirk-Othmer Encyclopedia of Chemical Technology*, John Wiley & Sons, 2001, <http://dx.doi.org/10.1002/0471238961.0308051304151901.a01.pub2>, (retrieved May 7, 2012).

Chapter 6

Conclusions and Future Work

6.1 Conclusions

A combined dilatometer mass spectrometer (CDMS) has been shown to be useful in identifying gas phase species and sintering progress during the heating of ceramics to high temperature. During the continued development of this characterization tool, a number of modifications and improvements have been made to the apparatus and to the procedure for conducting experiments. The mass spectrometer exhibits high sensitivity and high mass-to-charge (m/z) resolution over the range of $m/z=4-125$. The high sensitivity of the MS necessitated developing a procedure to reduce background contamination and hence gas-phase signals arising from this contamination. The procedure consists of performing an oxidation heating cycle followed by an inert conditioning cycle before each sample heating cycle. When heating carbide and boride ceramics, the platinum alloy thermocouple failed frequently during these cycles. This was attributed to operating in a reducing environment and also to the presence of sulfur, both of which are known to be detrimental to platinum. A thermocouple protection tube was thus designed that now allows the thermocouple to be in a protected environment at the expense of a slightly slower response time for temperature changes.

The gases evolved during the heating and sintering of barium titanate were investigated using the CDMS in chapter 3. Carbon dioxide and species related to its cracking in the MS were observed at low and intermediate temperatures, up to about 800-900°C, and were assigned to the decomposition of organic species and the decomposition of residual barium carbonate from the synthesis of barium titanate. Immediately following the CO₂ signals, at temperatures of 850-1200°C, signals corresponding to the evolution of sulfur dioxide were observed. The identification of the species were

accomplished using tabulated cracking patterns and isotope abundances, along with the cracking pattern from known gases (CO_2) and from model compounds (BaCO_3 and BaSO_4) that evolve the suspected species.

In chapter 4, the CDMS system was also applied to characterize the high temperature chemistry during the heating of individual ceramic powders (ZrB_2 , B_4C , SiC , ZrO_2 , and B_2O_3) that are routinely used to synthesize and sinter ultra-high temperature ceramics (UHTCs) ZrB_2 - B_4C , ZrB_2 - B_4C - SiC , and ZrB_2 - ZrSi_2 . The lower temperature MS signals (200-600°C) corresponded to the evolution of organics that were present from the application of the boron nitride spray applied to the ends of the sample, which was used to prevent undesired reactions with the spacers. High temperature signals (1000-1500°C) present during the heating of the ZrB_2 , B_4C , and SiC samples were assigned to the evolution of both CO and CO_2 . The sources for these signals are likely from surface oxide layers and other carbon and oxygen contamination in the powder. There was measurable weight loss for these samples, although the length change of the samples was negligible. The gas phase signals evolved from the loose B_2O_3 and ZrO_2 powder samples were not attributed to originating from the samples themselves but rather from background signals arising from the furnace environment. For all of the MS signals observed from the UHTC materials, species identification was achieved through the use of tabulated cracking patterns and naturally occurring isotope abundances.

The CDMS was also used to examine the evolved gas from ultra-high temperature ceramics of different compositions (ZrO_2 - B_4C , ZrB_2 - B_4C -PR, ZrB_2 - SiC - B_4C -PR-B-D-S, ZrB_2 -5- ZrSi_2 , ZrB_2 -10- ZrSi_2 , and ZrB_2 -20- ZrSi_2) in chapter 5. Low temperature signals (200-700°C) were identified as organics originating from the boron nitride spray and the

phenolic resin, binder, dispersant, and surfactant additives. High temperature signals (900-1650°C) evolved included CO and CO₂, with sources similar to what is found from the materials studied in chapter 4, along with the reactions between the main powder and the additives. The only samples that experienced sintering over the temperature ranges examined here were the ZrB₂-ZrSi₂ samples.

A major result of this work, which has been observed from several diverse ceramic powder systems, has been the detection of many reactions in real time that result in gas phase species occurring at different temperatures throughout the heating cycles. The sources of these reactions have been traced to either impurities in the powders or to reactions between powder compounds. Surface oxides and impurities from the powder production process were found to be the main sources of powder impurity. Reactions between powder compounds can include not only bulk material reactions but also reactions arising from surface oxide layers. The identification of gas-phase species arising from high temperature reactions and from powder impurities showcases the ability of the CDMS as a routine characterization tool for studying the gas-phase species evolved from ceramic materials at high temperature during sintering cycles.

6.2 Future Work

The CDMS has been developed into a fairly consistent and reliable characterization tool, but there are still aspects that could be improved to provide clearer insight into identifying evolved gas phase species during the heating of ceramic samples. The current configuration, which uses a capillary to introduce gases from the furnace environment into the mass spectrometer, does not easily allow for the use of other carrier

gases besides helium. In order to change to other carrier gases, the capillary must be replaced with one that has a smaller or larger diameter to adjust for the differences in the viscosity and the ionization probability between the gases. Installing a line-of-sight mass spectrometer would not only make it simpler to switch between carrier gases, it would also improve the signals obtained from the mass spectrometer. Replacing the capillary would further prevent the possibility of any species condensing in the capillary before reaching the detector of the mass spectrometer. The quantitative analysis based on the signals of the mass spectrometer would also improve since all species would be detected, not just the species that enter the capillary.

Another aspect of the CDMS that could be improved is the maximum operating temperature of the furnace, which is currently limited by the alumina materials (combustion tube, sample holder, and thermocouple protection tubes) and the thermocouple inside the furnace and the silica capillary that extends into the combustion tube but not all the way into the furnace. Removing the combustion and thermocouple protection tubes and replacing the alumina sample holder with a graphite sample holder would allow for much higher temperatures to be reached. In this modified setup, the thermocouple would be replaced with an optical pyrometer mounted on the exterior of the furnace for temperature readings. The silica capillary could also be an issue since the suggested maximum operating temperature is around 350°C. Current heating of the furnace to 1650°C has not resulted in capillary failure, but the increase of the maximum operating temperature of the furnace could cause the end of the capillary that is in the combustion tube to exceed 350°C. Another issue in this setup that uses the graphite sample holder to achieve higher maximum temperatures is that the oxidizing heating

cycle using air could not be performed to remove residual species present in the interior of the furnace environment without damaging the graphite sample holder and graphite heating elements. A light oxidizing heating cycle could possibly be run to accomplish the same goal; however, the sample holder and heating elements would still experience some oxidation.

In order to have a more complete characterization of the relationship between evolved gases and sintering during the heating of samples in the CDMS, several methods could be used. The change in heating rates and the inclusion of constant temperature holds at different temperatures could affect the temperatures of species evolution and the progress of sintering. The ability to reduce the time or temperature necessary to sinter leads to production cost savings along with the possibility of new applications for the product. The effect of pressing a powder, the particle size, and the powder composition should also continue to be explored with different powder systems. The addition of SEM and XRD analysis of samples would also aid in determining sintering progress and optimum heating cycle parameters.